DISSERTATION

Electromigration in Interconnect Structures

ausgeführt zum Zwecke der Erlangung des akademischen Grades
eines Doktors der technischen Wissenschaften
unter der Leitung von

O.Univ.Prof. Dipl.-Ing. Dr.techn. Dr.h.c. Siegfried SELBERHERR
Institut für Mikroelektronik

und der Assistenz von
Associate Prof. Dipl.-Ing. Dr.techn. Hajdin CERIC
Christian Doppler Laboratory for Reliability Issues in Microelectronics at the
Institut für Mikroelektronik

eingereicht an der Technischen Universität Wien
Fakultät für Elektrotechnik und Informationstechnik

von

Dipl.-Ing. Wolfhard H. ZISSER
0126308 / E 066 439
[redacted]

Wien, im Juni 2016

Kurzfassung

3D-Integration ist eine neuartige Technologie in der Mikroelektronik und eine Notwendigkeit für die Entwicklung von leistungsfähigeren Systemen in Bezug auf Größe, Geschwindigkeit und Energieverbrauch. Dabei werden die einzelnen Chips übereinander gestapelt, wodurch kürzere elektrische Verbindungen (Interconnects) möglich sind. Für die Verbindungen zwischen den gestapelten Chips sorgen neuartige elektrische Verbindungselemente wie offene Through-Silicon-Vias. Wie alle Interconnect-Strukturen sind auch diese der Elektromigration unterworfen. Elektromigration ist der gerichtete Materialtransport in Metallen ausgelöst durch die heutzutage gebräuchlichen hohen Stromdichten. An Stellen an denen Material abtransportiert wird, führt dies zu erheblichen mechanischen Spannungen. Dieser Materialtransport kann auch zur Unterbrechung der Schaltkreise führen. Elektromigrationsbedingter Leitungsausfall in Hinblick auf Leitungsunterbrechungen kann auf zwei unterschiedliche Arten entstehen. Bei der ersten Art führt die mechanische Belastung zu einem Riss quer durch das Interconnect und unterbricht damit die leitende Verbindung, welche damit zu einem abrupten Widerstandssprung führt. Im Gegensatz dazu führt bei der zweiten Art die mechanische Spannung zur Bildung eines Voids, also zu einem Hohlraum in dem kein Metall mehr vorliegt, welches die Leiterbahn nicht vollständig unterbricht und damit keinen Leitungsausfall hervorruft. Dieses Void kann dann in weiterer Folge in dem Metall durch die Elektromigration wandern und wachsen, was mit der Zeit den Widerstand der Leitung erhöht, bis dieser die Anforderungen des integrierten Schaltkreises übersteigt.

Traditionell werden Interconnect-Strukturen experimentell unter beschleunigten Testbedingungen getestet. Diese Experimente dauern jedoch sehr lange und die Planung hat äußerst sorgfältig zu geschehen, um aussagekräftige Ergebnisse für die Beurteilung der Zuverlässigkeit zu gewährleisten. Daher ist der verstärkte Einsatz von Modellen und Simulationen dieses Phänomens ein wichtiges Hilfsmittel, um die Entwicklung von integrierten Schaltungen zeitsparender und kostengünstiger zu gestalten.

In dieser Arbeit wurde ein Elektromigrationsmodel in ein kommerzielles Softwarepacket implementiert um eine möglichst einfache und breite Verwendbarkeit in der Industrie zu gewährleisten. Diese Software basiert auf der Finite-Elemente-Methode. Hierfür wurden die neuesten Modelle herangezogen und diese erlauben die Simulation der beiden oben beschriebenen Interconnect-Ausfallarten. Für die Implementierung des Voidwachstums wurde auf die Phasenfeldmethode zurückgegriffen. Diese erlaubt die Simulation von Voids, ohne dass nach einer Bewegung der Voidoberfläche erneut ein Gitter erzeugt werden muss. Dies ist möglich, da das Void sowie das Metall des Interconnects in der selben

Domäne liegen und die Unterscheidung nur durch den Wert des Ordnungsparameters realisiert wird.

Weiters wurde erstmalig die Implementierung zur Untersuchung der Widerstandsfähigkeit eines offen Through-Silicon-Vias gegen Elektromigration verwendet. Dabei wurden im ersten Schritt die Stellen lokalisiert, welche der höchsten Elektromigartionsbelastung ausgesetzt sind. Diese sind dort zu finden, wo die lokale Stromdichte am höchsten ist und in Folge dessen Current-Crowding auftritt. Diese Stellen sind insbesondere an Ecken und Kanten in der leitenden Struktur zu finden, welche besonders an den Stellen ausgeprägt sind, an denen das Aluminium mit dem Wolfram überlappend für die *Galvanische* Verbindung sorgt. Weiters ist der Vakanzenfluss durch Elektromigration vom Aluminium zum Wolfram blockiert, da Wolfram eine wesentlich höhere Beständigkeit gegen Elektromigration aufweist. Dadurch sammeln sich die Vakanzen nahe der Grenzfläche an und es bildet sich mechanische Spannung aus. In weiterer Folge sammeln sich im gesamten Aluminiumgebiet weitere Vakanzen an und die mechanische Spannung steigt weiter. Für den Eintritt einer Rissbildung wurde eine Spannung definiert und Simulationen für unterschiedliche Stromstärken durchgeführt. Die dadurch erhaltenen Zeitspannen bis zum Ausfall (time to failure) wurden dann anhand der *Black*'schen Gleichung zu einem Kompaktmodell kalibriert und zeigen eine gute Übereinstimmung zu den Vorhersagen *Black*s. Auch das Auftreten eines Voids und dessen zeitliche Entwicklung wurde simuliert. Hierfür wurde an die vorausgegangenen Simulationen angeknüpft und ein Void an jene Stelle gesetzt, bei der die höchste mechanische Spannung zu beobachten war. Die Simulation zeigte, dass das Void in Richtung des Aluminium-Wolfram-Übergangs zu wandern begann und dort angekommen weiter an Größe zunahm. Dadurch erhöhte sich der Widerstand bis die Leiterbahn eine Unterbrechung aufwies, welche letztlich zu einem abrupten Widerstandsanstieg führte. Auch diese Simulationen wurden für verschiedene Stromstärken durchgeführt und mittels der *Black*'schen Gleichung gefittet. Die beiden gefitteten Kompaktmodelle erlauben die Vorhersage der Ausfallzeiten für diese Struktur unter Berücksichtigung verschiedener Parameter (z.B. Stromdichten, Temperatur) und sind damit ein wichtiges Werkzeug für die Entwicklung von integrierten Schaltungen.

Abstract

3d-Integration is a novel technology in microelectronics and a necessity for the development of systems with enhanced performance with respect to size, speed, and power consumption. Thereby, the individual chips are stacked on top of each other, thus shortened electrical connections (interconnects) are possible. For the connections between the stacked chips novel electrical connection elements such as open through-silicon-vias are utilized. As all interconnect structures also these suffer from electromigration. Electromigration is the directed material transport in metals triggered by the nowadays common high current densities. At locations where material transport occurs, this leads to significant mechanical stress. The material transport can also lead to an interruption in the circuit. Electromigration mediated line failure with respect to line disruptions can arise from two different modes. In the first mode the mechanical load leads to a crack across the interconnect and through this to an interruption of the conducting connection, which results in an abrupt resistance jump. In contrast to this, in the second mode, the mechanical stress leads to the formation of a void, thus to a hollow region where metal can no longer be found which does not fully interrupt the metal track and thereby does not generate a line failure. This void can further migrate and grow in the metal, which with time increases the line resistance, until the specification of the integrated circuit is exceeded.

Traditionally interconnect structures are tested experimentally under accelerated test conditions. These experiments last very long and the planing must be very carefully carried out, in order to ensure meaningful results for the evaluation of the reliability. Therefore, the increased utilization of models and simulation of this phenomenon is an important tool to develop integrated circuits more economically regarding time and cost.

In this work an electromigration model was implemented in a commercial software in order to ensure the easiest and broadest exploitation in industry. This software is based on the finite-element-method. For this the newest models were considered, which allow for the simulation of both above-mentioned interconnect failure modes. For the implementation of void evolution a phase-field-model was facilitated. This allows for the simulation of voids without requiring remeshing after the void surface movement. This is possible, since the void and the interconnect metal lie within the same domain and the distinction is realized only through the value of the order parameter.

Furthermore, for the first time, this implementation for the assessment of the durability of an open through-silicon-via under electromigration was employed. In the first step the regions were localized which experience the highest electromigration load. They are found at the locations were the current density is highest and subsequently current crowding appears. These locations are found especially in corners and edges of the conducting structure, which are particularly pronounced at the overlapping area of the aluminium and the tungsten, which realizes the galvanic connection. Further is the vacancy flow through electromigration from the the aluminium to the tungsten blocked, since tungsten possesses a much higher durability against electromigration. Thus, vacancies gather close by the interface and a mechanical stress is formed. Subsequent thereto more vacancies are accumulated in the entire aluminium region and the mechanical stress rises further. For the occurrence of a crack formation a threshold was defined and simulations for different current values were performed. The gained times to failure were used to calibrated a compact model via the *Black* equation and showed good agreement in comparison to *Black*'s predictions. Also the occurrence of a void and its time evolution have been simulated. For this purpose previous simulations were continued and a void was placed at the location were the highest mechanical stress was observed. This simulation revealed that the void started to migrate towards the aluminium/tungsten interface and after reaching it further grew in size. Thus, the resistance increased, until the metal line showed a disruption which lead also to an abrupt resistance jump. Also these simulations were carried out for different current values and fitted with the *Black* equation. These two fitted compact models allow the prediction of the time to failure for the structure under consideration with different parameters (e.g. current density, temperature) and therefore are an important tool for the development of integrated circuits.

Acknowledgments

First of all I am very grateful to Professor Siegfried SELBERHERR for his support through out my time at the Institute of Microelectronics. I appreciate also that he took the time to correct my thesis very thoroughly.

Professor Hajdin CERIC gave me the opportunity to work in the field of electromigration, funded by his Christian Doppler Laboratory for Reliability Issues in Microelectronics, and supported me with various discussions, suggestions, and comments.

I am very glad, that Professor Erasmus LANGER managed all the bureaucratic and organizational tasks and by this kept my time free for the project.

Further, I thank Professor Manfred KALTENBACHER for serving on my examination committee.

Professor Roberto LACERDA de ORIO introduced me to the topic of electromigration and eased the start of my doctoral program, while Dr. Thomas WINDBACHER and Dr. Lado FILIPOVIC reviewed my thesis.

Contents

Nomenclature

2D	Two-Dimensional
3D	Three-Dimensional
CMOS	Complementary Metal–Oxide–Semiconductor
CVD	Chemical Vapor Deposition
DRIE	Deep Reactive Ion Etch
EM	Electromigration
FEDOS	Finite Element Diffusion and Oxidation Simulator
FEM	Finite Element Method
GB	Grain Boundary
IC	Integrated Circuit
ILD	Inter-Level Dielectric
IVD	Inter-Via Dielectric
KKR	Korringa-Kohn-Rostoker
LKKR	Layer KKR
PDE	Partial Differential Equations
PECVD	Plasma Enhanced CVD
TCAD	Technology Computer Aided Design
TSV	Through Silicon Via
TTF	Time to Failure

UV	Ultraviolet
A	Area
B	Applicable Mechanical Modulus
C_a	Atom Concentration
c_T	Specific Heat Capacity
C_v	Vacancy Concentration
C_v^eq	Equilibrium Vacancy Concentration
d	Grain Size
D_a	Atom Diffusion Coefficient
D_eff	Effective Diffusion Coefficient
D_GB	Grain Boundary Diffusion Coefficient
D_s	Surface Diffusion Coefficient
D_v	Vacancy Diffusion Coefficient
E	Electric Field
e	Unit Charge
E_a	Activation Energy
F	Mechanical Force
f	Relaxation Factor
j	Current Density
J_a	Atom Flux
J_v	Vacancy Flux
k_B	Boltzmann Constant
Q^*	Heat of Transport
$\dot{q}$	*Joule* Heat Generated per Time
R_p	Flaw Radius
T	Temperature

T_{ref}	Reference Temperature
$\mathbf{u}$	Displacement Field
V	Volume
W	Elastic Strain Energy
Z^*	Effective Valence
$\mathbf{C}$	Elastic Tensor
δ	Grain Boundary Width
$\delta_{i,j}$	*Kronecker* Delta
ϵ	Mechanical Strain
ϵ_{pf}	Phase Field Interface Thickness Parameter
ϵ_{T}	Temperature Induced Mechanical Strain
ϵ_{v}	Vacancy Related Mechanical Strain
ϕ_{E}	Electric Potential
γ_{S}	Surface Energy
κ	Surface Curvature
λ	*Lamè* Parameter
λ_{T}	Thermal Conductivity
μ	Chemical Potential
ρ	Specific Electric Resistance
ρ_{M}	Material Density
σ	Isotropic Stress
σ_{E}	Electric Conductivity
σ_{th}	Threshold Stress for Void Nucleation
τ	Characteristic Relaxation Time
Ω	Atomic Volume

List of Figures

Chapter 1

Introduction

Traditionally integrated circuits (IC) are manufactured by mounting a single die in a package. Thus, bigger dies in terms of space are needed to realize more complex circuits for a given technology node. This approach leads to a higher length of the interconnects. In contrast to the transistors the propagation velocity of interconnects did not increase by scaling, leading to higher signal run times. On the other hand more complex circuits can also be achieved through higher integration densities. This approach is restricted by limitations of the endurable power density. To avoid these circumstances three-dimensional (3D) integration was proposed [46] and is widely used for applications reaching from the miniaturization of portable devices to power efficient high performance computing, for instance servers and supercomputers [108]. Thereby opportunities for improved power efficiency, increased band width, and lower latency can be harvested [80]. This technology uses the third dimension by stacking the dies one above the other. With the introduction of this technology heterogeneous integration and smaller footprints became possible, leading to the opening of new product possibilities [47]. In the process of designing 3D integrated circuits some factors, e.g. heat generation and dissipation, stress development due to the stacking, must be considered to avoid reliability issues and break down of systems [119].

For 3D integration not only planar interconnects, providing the connections of the devices on a single die, but also vertically connecting structures, applying the connections between the stacked dies, are required [108]. These vertically connecting structures include solder bumps for the connections between the dies in contrast to a thinning and bonding process. Furthermore, through silicon vias (TSV) are used for the connection trough the dies. Due to the introduction of these components new reliability issues arise. These issues include delamination and cracking due to residual stress introduced from the fabrication process as well as thermal expansion [83] and void formation and growth because of electromigration (EM) [5, 72] among others [20, 24, 44]. Therefore, an adequate characterization of the vertically connecting structures is necessary to get a deeper insight of the failure mechanisms degrading these components.

The aim of this thesis is the implementation of EM degeneration models in the simulation tool COMSOL [30], based on the soft failure phase, and the EM assessment of the open TSV technology. Thereby the prediction of the lifetime of open TSVs and the localization of the areas with the highest failure occurrence probability are addressed. Furthermore, the results of simulations based on the finite elements method (FEM), taking all aspects regarding the two different phases of EM into account, are used for the calibration of a compact model.

1.1. Interconnect Structures in Microelectronics

Interconnect structures are responsible for the transmission of signals within electronic circuits. The first structures in use were single wire connections between the active, as electronic tubes and transistors, and passive elements like resistors, capacitors, and inductors found in old days radios. The next step was the development of printed circuit boards. These boards consist of copper layers laminated on polymeric substrates. By etching lithographically developed patterns into the copper, conductive tracks are obtained. This planar structure connecting the electric components exhibits low aspect ratios and allows the application of low cost wet etching techniques [146].

In integrated circuits the active components are placed in the substrate, usually silicon, whereon planar interconnect structures are grown. Besides the conducting lines several other layers are placed between them such as dielectric, etch stop, anti-reflective coating, diffusion barriers, and plugs realizing vertical connections, and thereby realizing multiple metallization layers [108].

The function of interconnection in integrated circuit is the distribution of the clock signals, the power, and the transmission of signals over the chip connecting various system functions. Due to the desired development of fast integrated circuits the interconnects have to meet the high speed requirements for the clocks, the signals, as well as the down-scaling of sizes. A typical parameter for interconnect speed is the RC time delay given by the product of the resistance and the capacitance of the line. To minimize this delay the interconnect structures have to be properly designed and material systems with conducting materials exhibiting low resistance as well as isolation materials between the lines with low permittivity have to be developed and implemented [146]. The conducting materials should fulfill the following requirements:

- low resistance
- high thermal conductivity
- high melting temperature
- compatibility to the isolation materials, the barrier, and capping layers
- compatibility to the back-end-of-line process

The two materials primarily used for IC metallization are aluminium and copper. In Table 1.1 their most important material parameters are summarized.

Physical property	Aluminium	Copper
Specific electrical resistivity ($\mu\Omega$ cm)	2.72	1.71
Thermal conductivity (W/mK)	238	327.7
Melting point (K)	933.5	1358

Table 1.1.: Material properties of aluminium and copper [146].

1.2. Aluminium Based Interconnect Fabrication

For the fabrication of interconnects two strategies are currently used. The subtractive method and the inlaid method also called damascene process. For aluminium the first process mentioned is used and the process flow for one metallization layer is depicted in Figure 1.1. In the first step a silicon oxide is deposited (cf. Figure 1.1a) followed by the deposition of a photoresist. The photoresist is exposed to a UV light, transferring the pattern from the mask to the photoresist layer. After dissolution of the areas exposed to the UV light, the photoresist shows the pattern of the mask and serves in the etching process as an etch mask for the silicon oxide layer. After etching the oxide (cf. Figure 1.1b) the resist is removed and sequentially a barrier layer and a tungsten layer are deposited, filling the etched holes and forming a layer as shown in Figure 1.1c. To remove the unwanted barrier and tungsten layer, the wafer is polished leaving only the filled holes back (depicted in Figure 1.1d). These holes form the vias responsible for the vertical connections between the metallization layers and between the metallization and the devices. Thereafter a diffusion barrier, an aluminium layer, and another diffusion barrier are deposited (cf. Figure 1.1e). The diffusion barriers are formed by titanium and titanium nitride preventing the aluminium to diffuse into the silicon and as an antireflective coating for lithography purposes [146, 148]. In the next step a photoresist is deposited and exposed to UV light to transfer the pattern from the mask. After dissolution of the exposed photoresist and etching the aluminium exhibits the desired pattern depicted in Figure 1.1f. The last steps for this metallization layer are the removal of the unexposed photoresist and the deposition of an isolating oxide (cf. Figure 1.1g), which is polished to receive a flat surface for eventually further following metallization layers. By repeating this procedure a multi-layer interconnect structure is obtained [119].

1.3. Copper Based Interconnect Fabrication

IBM began to developed metallization technologies based on copper in the 1990s [2, 81]. One benefit, as shown in Table 1.1, is the reduced resistance compared to aluminium of about 40%. The process of fabrication had to be modified as there is no reactive ion etching process for mass-production, quite contrary to aluminium [146]. Therefore the fabrication process for aluminium fabrication is adopted in the following way. After the deposition of the silicon oxide a second oxide layer is grown. This oxide is covered with a photoresist which in turn is exposed to UV light for the pattern transfer from the mask and subsequently dissoluted. After the etching process the oxide remains

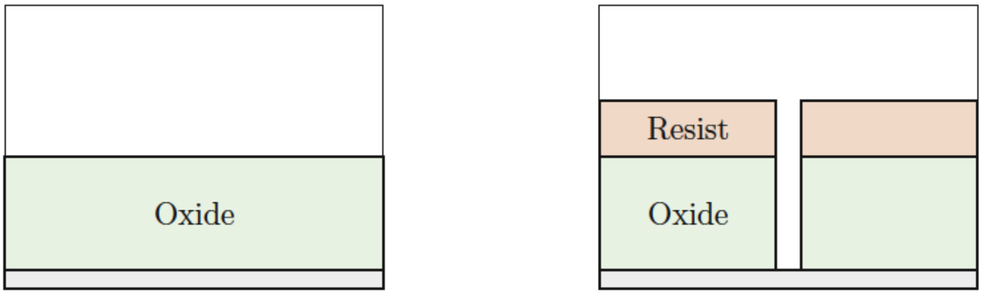

(a) Oxide deposition (b) Via etch

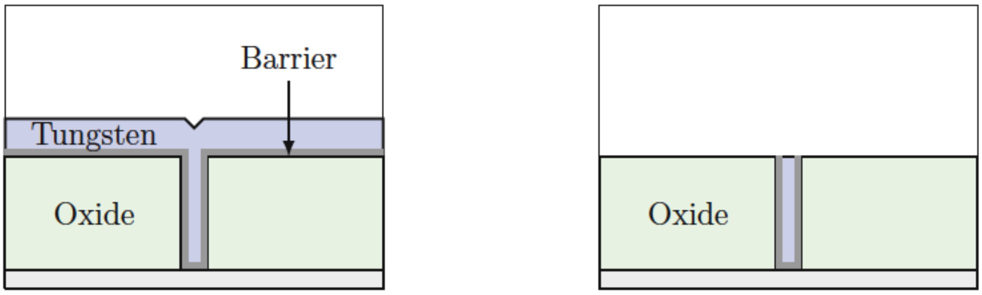

(c) Barrier and tungsten deposition (d) Tungsten and barrier polish

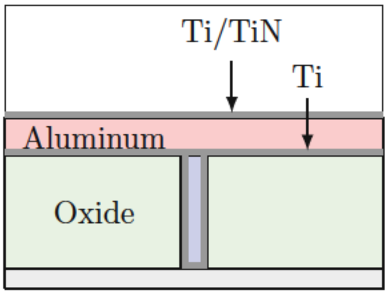

(e) Deposition of titanium, aluminium, and titanium nitride

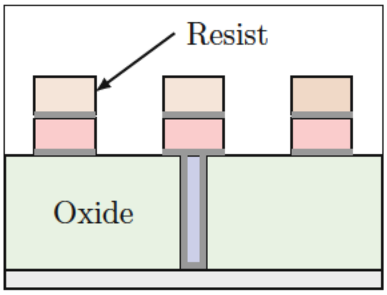

(f) Etch of metallization

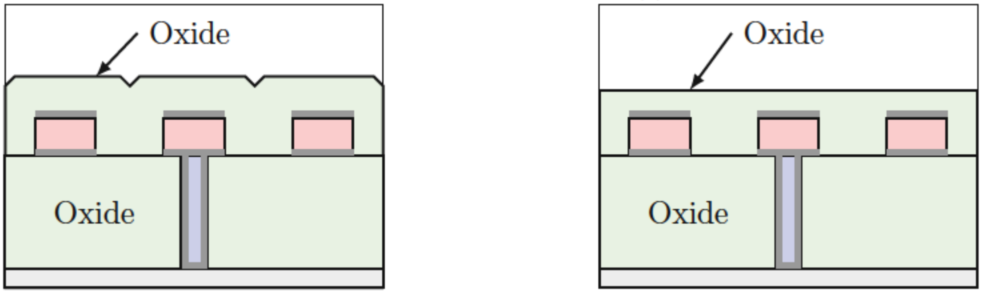

(g) Oxide gap fill (h) Oxide polish

Figure 1.1.: Fabrication process of a aluminium metallization layer. By repeating the steps a multi-layer structure is realized. [146].

only at those locations where no copper should be located and the copper is deposited into the trenches and forms a layer at the top of the wafer. By chemical-mechanical polishing the top layer is removed and only the filled trenches remain. For the isolation another oxide layer is deposited and the steps described are repeated until the last metallization layer is formed [146]. This process is comparable to the tungsten via creation used in the aluminium fabrication process as discussed before. Therefore, the processes forming the vias and the lines are very similar which enables the reduction of the process steps by saving one isolation oxide deposition, diffusion barrier, copper deposition, and planarisation step [69, 149].

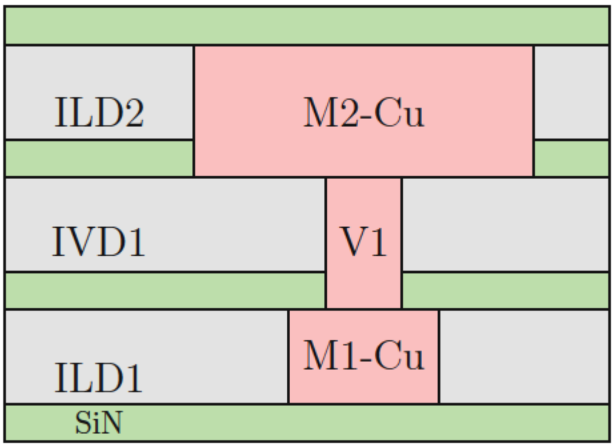

(a) Single-damascene structure

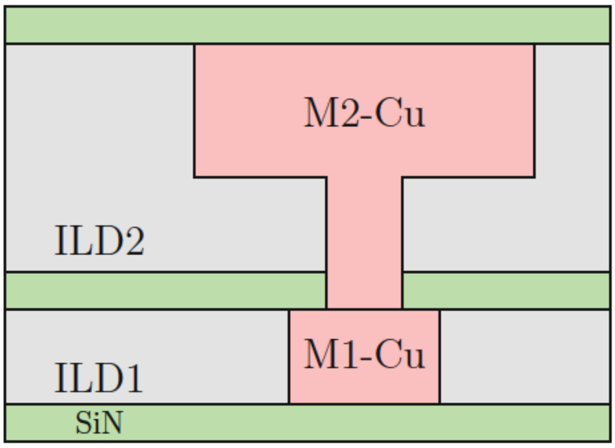

(b) Dual-damascene structure.

Figure 1.2.: Cut through a single and dual-damascene interconnect structure [61].

The dual-damascene process takes advantage of of the possibility to omit several process steps and is explained in the following. First an inter-level dielectric (ILD) layer is deposited on the wafer, followed by a photolithographic pattern transfer, the dissolution of the exposed photoresist, and etching of the via holes. By depositing another photoresist and exposing it to UV light masked by the line patterns the structure of the lines is transferred. After dissolution of the photoresist and etching, the trenches of the lines are etched into the ILD and the via holes are further etched to the bottom of the layer. The last steps are a deposition of the barrier layer and the copper, filling the vias and trenches, as well as forming a layer at the top of the wafer which is removed by chemical-mechanical polishing and covered by a non-conductive diffusion-barrier layer (eg. SiN) [149]. Figure 1.2 compares the single- to the dual-damascene structure. In the dual-damascene structure the inter-via dielectric (IVD) layer is missing giving an idea of the reduction of the fabrication steps.

1.4. Three-Dimensional Integration

Commonly ICs are built in a planar 2D design style. For miniaturization and performance increase of electronic systems the increased utilization of 3D integration methods is unavoidable [1]. Thereby dies are stacked and have to get vertically connected to enable the signal flow between them. Therefore novel interconnect structures are introduced reaching through the single dies and connecting from one die to the other. This increases besides the area efficiency (for 5x5mm dies in a 7x7mm package in the range of 50%) also the volumetric efficiency which is nowadays only in the range of 0.01% and potentially allows shorter interconnections than in 2D configurations enabling higher operation speed and lower power consumption. On one side this is of particular importance for high performance computing as in synchronous operating mode the latency of the clock signals depending on the interconnection length is a limiting factor [7]. On the

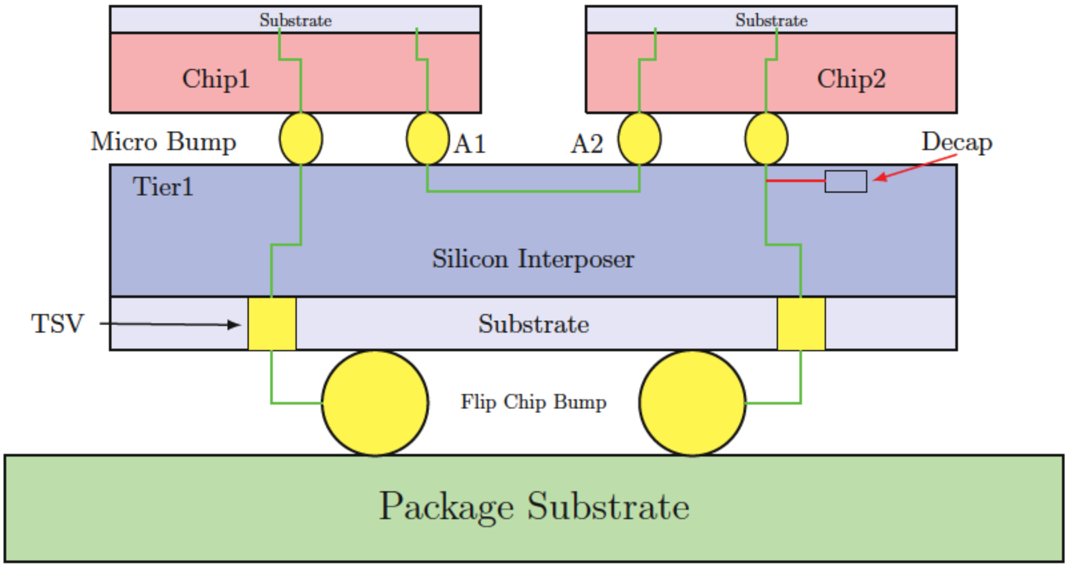

Figure 1.3.: Schematic of a chip-to-wafer bonded structure. Stapled dies hold together by solder bumps.

other side 3D integration also allows the stapling of dies based on different technologies, which is called heterogeneous integration (e.g. analog, digital, sensors, antennas, and power electronics) and different technology nodes [71].

Bonding is the process of mounting one wafer or die onto another. The first method is termed wafer bonding. Thereby two wafers are bonded before the wafers are cut into single dies. Due to the easier alignment this method was developed first. The second possibility is called chip-to-wafer bonding. With this method the dies can have different dimensions giving more flexibility as one chip can carry more then an other chip. Figure 1.3 shows a possible combination of different dies connected by solder bumps in the chip-to-wafer configuration [108].

The available bonding processes can be divided into two kinds. The first is called direct bonding, where no intermediate layer is separating them. This type is separable into molecular bonding and anodic bonding. The second is the bonding with intermediate layers, where polymer, glass [79] or solder bumps are put in between them to hold the wafers together [140]. In the next section TSV structures are introduced with a special focus on the direct bonding method, based on a device presented by *Kraft et al.* [83].

1.5. Open TSV Structure

A recent TSV design is realized by filled copper TSVs and has the advantage of a low contact resistance [81]. However, the price of a high mechanical stress due to the mismatch of the thermal expansion coefficient of the TSV materials and the substrate has to be paid [122]. Furthermore, the depth of the TSV structure is limited to approximately 50μm determined by the limitation of the aspect ratio of the etching process and the limited thicknesses of copper deposited by electroplating. Therefore, the open TSV structure was introduced, where the filling of the vertical cylindrical structure is replaced by a metallization layer plated on the cylindrical wall leaving it hollow, as depicted in Figure 1.4. The fabrication of the open TSV structure is carried out after the front-end and back-end metallizations are performed in a regular CMOS process. In the following sections the steps for the open TSV fabrication are presented for a sensor chip which is wafer bonded on a CMOS wafer [83].

1.5.1. Wafer Bonding

After the final via layer has been processed the top wafer gets thinned to a thickness of 250μm and fine polished at the backside to a roughness of $R_{\max} < 0.5$nm to obtain a suitable surface quality for the wafer bonding. The bond interface of the bottom wafer is prepared by oxide deposition employing a plasma-enhanced chemical vapor deposition (PECVD) technique [45], a densification step, and a chemical-mechanical polishing step which results in a low surface roughness without any nano-topology larger than 10nm. After removing organic contamination and small particles with a cleaning step, the bond surfaces are activated by a nitrogen plasma, followed by a further cleaning step, and aligning of the bottom and the top wafers to each other. By bringing them into contact a bond wave is started [108]. The smoothness of the surfaces has to be guaranteed as otherwise the bond wave propagation is disrupted leading to unbonded regions. This can result, beside others, in a chip off, which is the unwanted unbonding of dies, or increased resistance. The bond wave step is followed by an annealing step resulting in a bond strength of >2J/m. These steps are followed by a deep reactive ion etch (DRIE) process, the so called *Bosch* [40] process, described in the following.

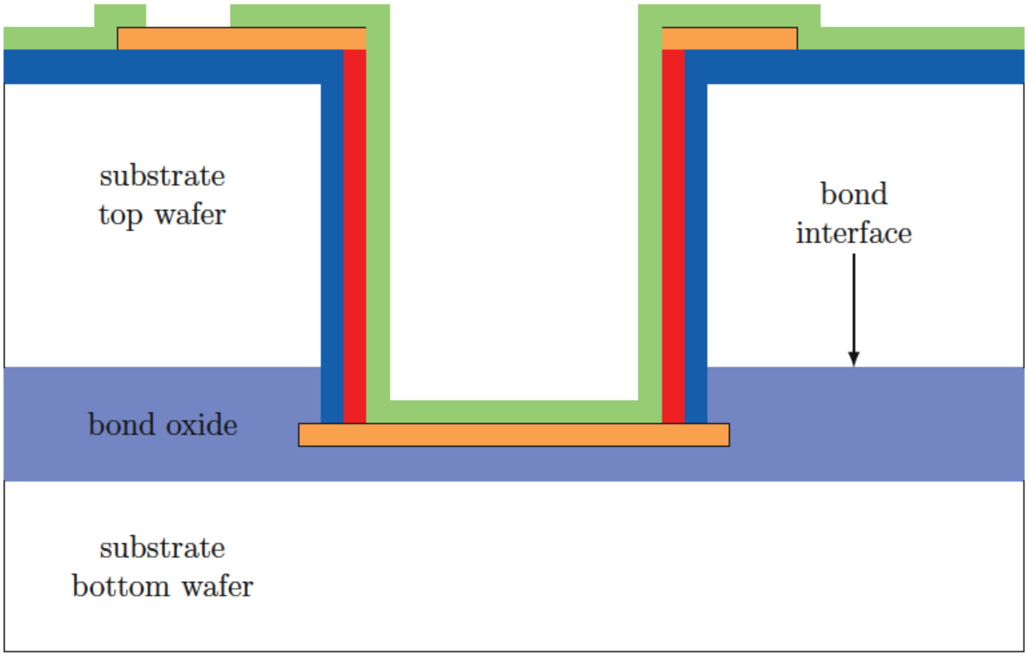

Figure 1.4.: Schematic of the TSV [83]. The orange regions are aluminium, the red are tungsten, the dark blue are the galvanic isolation layer from the metal to the silicon bulk, and the green are the passivation layers. For bonding the bottom wafer is prepared with a silicon oxide (in light blue) and the top wafer is planarized silicon.

1.5.2. The Bosch Etching Process

The *Bosch* process [23, 31] is a sequence of alternating dry plasma etching and polymer deposition cycles, each lasting only in the range of seconds. The main advantage is the highly anisotropic etching which provides the ability of high aspect ratios between TSV heights and TSV diameters as well as ensuring high mask selectivity and almost vertical sidewalls [85].

The process is carried out by the following steps. First of all the silicon wafer must be covered with a photoresist. This photoresist is exposed to a patterned intensive light causing chemical reactions which allow the removal of the photoresist at the exposed positions by the developer [123]. The remaining parts of the photoresist form the mask which is necessary to prevent the covered material from being etched. This mask producing process stage is followed by the actual series of the alternating plasma etching and polymer deposition cycles. For the etching process sulfur hexafluoride SF_6 together with a carrier gas (mostly argon) is injected into the reactor containing the wafer. By the generation of a high energetic plasma the SF_6 is transformed into a highly reactive gas realizing an isotropic, chemical etching reaction. This etching is combined with a physical etching realized by the sputtering of ions adding an anisotropy. This step is followed by polymerization, where the before created structure is passivated by coating it with a polymer layer. For this step fluorocarbons such as C_4F_8 and a carrier gas is led into the reactor. This mixture is activated and forms a polymer passivation layer on the mask as well as on the sidewalls and on the bottom of the etched trench. The polymerization step is followed by a further etching cycle. In this cycle due to the anisotropy of the etching process the passivation layer in the bottom of the trench is first etched through. Therefore at the bottom the etching of the silicon starts again, whereas the sidewalls are still protected by the passivation layer, attaining the anisotropy of the overall alternating process. The trench narrows as the depth increases and the polymer is continuously recoating the structure. These two cycles are repeated, until the requested TSV depth is achieved.

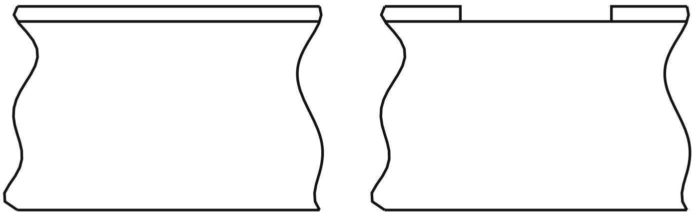

(a) Wafer coated with photoresist

(b) Photoresist washed away by the developer.

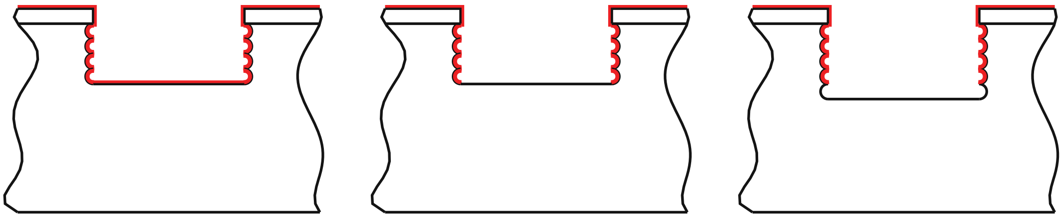

(c) Passivation by coating with a polymer.

(d) Etching of the polymer till the bottom silicon is free.

(e) Etching of another well. This step is followed by the passivation step (c).

Figure 1.5.: Schematic of the *Bosch* process.

1.5.3. Isolation and Metallization of the Open TSV

After the sequentially repeated etching and passivation processes have reached the metallization layer of the bottom wafer isolation, lining and passivation processes have to be carried out. For the isolation of the conductive TSV lining against the semiconducting silicon bulk, a region of silicon oxide is introduced. The process temperature must not exceed 300°C as the aluminium metallization is already present in the bottom wafer. Therefore *Kraft et al.* [83] chose a sequence of three layers consisting of a PECVD layer, a sub atmospheric chemical vapor deposition (SACVD) layer, and another layer made by PECVD. The PECVD process reaches a temperature of 350°C and the SACVD layer a temperature of 400°C. The SACVD process is interposed due to its good gap filling property and the high conformity of the film deposited, in contrast to PECVD. Before the metallization can be deposited the isolation and the metal oxide at the bottom to the adjacent metal pad have to be removed, which is accomplished by a deep spacer reactive ion etching (RIE) step. The metallization layers are deposited in the following sequence. First a titanium and a titanium nitride layer is placed as an adhesion layer by a physical vapor deposition (PVD) sputtering process [63]. As sputtering processes provide low side wall deposition [65] the quite novel self ionized plasma option was employed, offered by the newest generations of sputter tools [83]. The actual conducting tungsten layer is then deposited by a metal CVD and removed at the top of the wafer by a maskless back-etch process using SF_4. This process is an anisotropic RIE step leaving the tungsten behind at the sidewalls and does not reach to the bottom metallization. The titanium as well as the titanium nitride act for the etching process as a stopping layer in the TSV top region. At the last metallization step aluminium is sputtered connecting the top interconnection structure to the tungsten at the sidewalls. To protect the metallization against moisture passivation layers are placed in the same schema as the isolation to the bulk silicon, finalized by a silicon nitride layer.

1.6. Failure Mechanisms in Interconnects

In interconnects, failures are the variation of parameters beyond critical values which prevents the designated function of integrated circuits. The typical parameters are the resistance of the interconnect and the resistive and capacitive isolation to neighboring components like interconnects, devices, or to the bulk. Differences between the experienced parameters and the designed parameter can be caused by defect-related problems or by wear-out.

Defect-related problems are caused by the fabrication process. Missing process steps and especially dirt contamination can be responsible for regions where the conducting material is missing, leading to higher resistance than designed [92, 109]. Furthermore, the isolating layers can be thinner than engineered, leading to higher leakage currents and capacitive coupling into other system parts, affecting there function.

Wear-out, in contrast, is a failure phenomenon, which occurs or evolves under the operation of the devices. This can even occur under normal operating conditions. Wear-out phenomena are for example material diffusion from the metal into the semiconductor or the isolation/dielectric leading to a change in the electrical characteristics, or temperature induced phenomena leading to stress induced failure (e.g. cracking or delamination) [134].

1.7. Electromigration Induced Failures

One of the processes leading to wear-out degeneration in interconnect structures is EM, the directed transport of atoms under the influence of an electric field acting as one force and a resulting electric current contributing to a second force. The electric field force - the so called direct force - is a result of the ionic character of atoms in a metallic lattice as the valance electrons responsible for the electric conductivity are not bound to their atom anymore. Furthermore, the conducting electrons driven by the electric field are scattered at the atoms exerting a force on them and this force is the so called wind force. Figure 1.6 depicts this circumstances.

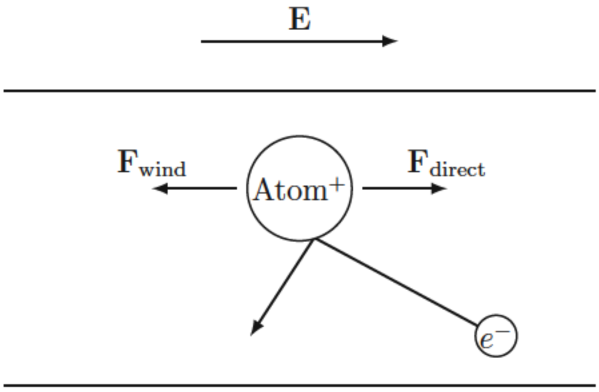

Figure 1.6.: The two forces of EM.

Beside this phenomenon, other material transport inducing phenomena are acting inside metals. Some are uncorrelated to the EM induced flux, e.g., thermal migration [103], and some are compensating partially the EM flux [18], e.g., diffusion [32]. The transport of material in interconnect structures is leading to a mechanical stress build-up in the structures. These stresses can be tensile, when material is transported away, causing cracking or void formation and thereby leading to a degradation as the conducting cross sections are reduced. In the worst case an open circuit failure can be observed. The stress can also be compressive, which can crack the passivation and isolation layers between interconnects or other devices and cause the formation of a hillock. This leads to a reduction of the isolation gaps and thus degrades or even destroys the desired function of an IC. Therefore, ICs have to be checked against these phenomena [33]. For these assessment tests under accelerated test conditions are carried out and the results are extrapolated to normal operation conditions. An extrapolation of the data is only reasonable, if the phenomenon leading to degeneration under accelerated conditions is the same as under normal operation conditions. Therefore, these tests have to be designed very carefully. Typical accelerated conditions are increased electric current densities and elevated temperatures. These conditions can cause melting especially in big devices like TSVs and thereby renders an extrapolation impossible as another phenomenon was tested against [135]. Due to this and the long times needed for experimental tests, TCAD simulations are the method of choice to give designers a tool for pretesting or even testing.

1.8. Outline of this Thesis

The main aim of this dissertation is to investigate the open TSV technology regarding EM failure. This investigation includes the two phases of EM degeneration, where the first phase is the phase where stress is built up leading to cracking or void formation. In the case where a void is formed, the first phase is followed by the second phase where the void moves within the metal structure and expands leading to failure. In order to cover the full range of failure development, models for both phases are implemented into the Finite Elements Method (FEM) simulation software COMSOL [30] to provide the ability to analyze the lifetime of interconnect structures as well as to examine the impact of design changes on the lifetime. The validity of the implemented model is demonstrated. The first phase model is verified by comparing the results originating from the TCAD tool FEDOS developed at the institute. The results of the evaluation of the models for the second phase are qualitatively compared to results from experiments. This accomplishment is the basis for the EM failure assessment of interconnect structures taking also voiding into account.

This thesis is logically structured into 6 chapters. Chapter 2 gives a historic outline of the discovery of EM and the development of its modeling originating from the compact model developed by *Black* [10] relating current densities and lifetime. This is followed by *Blech*'s findings [14], a critical length times current product for the occurrence of EM induced voiding and hillock development. After the description of these simple models more advanced and complex models are introduced, where the impact of the vacancy dynamics and the stress build-up is gradually incorporated, finally resulting in the state of the art model for EM. The chapter closes with the introduction of the quantum mechanical EM force calculation giving a fundamental understanding of the different resistances of materials and interfaces against EM.

In Chapter 3 the models for a physics based EM assessment are presented in detail. To describe EM failure a variety of different physical phenomena have to be considered, resulting in the need to simulate a multiphysics problem. This includes in bulk regions the electro-thermal problem, as the current is the driving force for EM, the vacancy dynamics, and the continuum mechanical model. For interfaces, different behaviors are known including the fast diffusivity, differing equilibrium concentration, and segregation and are therefore described in this section. To detect the starting point of phase two a critical stress value is needed as a threshold value as explained in the void nucleation section. For the second phase, after a void is formed, the void evolution has to be tracked according to the phase field model explained in Section 3.6.

Subsequently Chapter 4 deals with the details of the essential implementations of the simulation models and how they are carried out for the two simulation tools employed for this work. First the required basis of FEM and its derivation are pointed out, building the principle method of computation for the simulations in FEDOS and COMSOL. Second the specifics concerning the process flow and the model implementation are presented.

Chapter 5 discuses the entire assessment of an interconnect structure with simulation results and their implications. After opening with an analysis of the current crowding effect, reasoning the locations of high current densities at corners of the conducting structure, the vacancies pile-up at the interface of two different metals due to a blocking behavior is surveyed. The typical characteristic of EM induced vacancy accumulation featuring a three phase behavior in time is used as an initial verification and is therefore discussed subsequently. Thereafter the stress build-up in the structure is simulated to evaluate the time until cracking or void formation for different current densities and is followed by the void evolution simulation. The assessment is completed by a fitting of the times resulting from the two phase simulations to *Black*'s equation.

Finally, the thesis is concluded in Chapter 6 giving an outline for possible further improvements by taking atomistic and micro structural properties into account.

Chapter 2

Physics

2.1. Historic Outline of Electromigration

Electromigration was first discovered by the french physicist M. Gerardin in 1861 [104]. In the 1950s systematic studies of electromigration were carried out by W. Seith and H. Wever [120] showing the correlation between the direction of the current flow and the material transport. In the 1960s electromigration was recognized as one of the main failure phenomena leading to the development of different failure criteria and physically based models [143].

2.1.1. *Black*'s Equation

While working for Motorola in the 1960s, *James R. Black* was involved in the understanding of the "cracked stripe" problem [95]. This phenomenon was found to be electromigration induced. He carried out a systematic investigation and derived a model for the failure time prediction [10]. The model is based on the concept that a failure criterion is reached, if a structure specific mass is transported away.

$$TTF \cdot R \propto 1 \tag{2.1}$$

R is the mass transported per time. This leads to the inverse proportionality of the TTF to the rate of mass transport.

$$TTF \propto \frac{1}{R} \tag{2.2}$$

This rate R is modeled by the proportionality

$$R \propto n_\mathrm{e} \Delta p N_\mathrm{a} \tag{2.3}$$

with n_e being the conducting electron concentration, Δp the impulse transferred from the electrons to the atoms while scattering, and N_a the density of thermal activated atoms. The first two variables n_e and Δp are proportional to the current density j and the density of activated atoms is modeled by the *Arrhenius* law [137]

$$N_\mathrm{a} \propto \exp\left(-\frac{E_\mathrm{a}}{k_\mathrm{B}T}\right), \tag{2.4}$$

with the activation energy E_a, the *Boltzmann* constant k_B and the temperature T. The combination of (2.2)-(2.4) leads to *Black*'s equation.

$$TTF = \frac{A}{j^2}\exp\left(\frac{E_\mathrm{a}}{k_\mathrm{B}T}\right) \tag{2.5}$$

The constant A comprises the material properties as well as the geometry and must be empirically determined [11, 12, 13].

The inverse j^2 dependence is a special case which can be extended to the generalized *Black*'s equation

$$TTF = \frac{A}{j^n}\exp\left(\frac{E_\mathrm{a}}{k_\mathrm{B}T}\right), \tag{2.6}$$

by substituting the exponent 2 by a second parameter n called the current exponent. The correct value for this parameter was extensively debated [77, 93]. According to *Clement* [26] lifetime models can be roughly classified into two groups. Void growth models, where the failure is triggered by the growth of a void over a critical size and nucleation models, where the failure is triggered by the stress build-up in the structure exceeding a critical value. For the void growth model the current exponent is found to be 1, because the mass transported is proportional to the current resulting in an inverse relation to the TTF [126]. Models based on the nucleation show an exponent of 2 as in the original *Black* equation due to the stress induced back flow flux [5, 91].

For the prediction of the TTF the generalized *Black* equation is used to extrapolate the results from accelerated test conditions with increased currents and elevated temperatures to normal operation conditions. In this application the current exponent is a second fitting parameter beside the parameter A. Measurements reported in the literature show values for n ranging form slightly greater than one to six [107]. Values above two are explained by the improper treatment of the *Joule* heating. Values in the range between one and two are interpreted as a failure based on a mixture of the two models, where a void is first nucleated and followed by a growth phase.

2.1.2. *Blech* Effect

Ian A. Blech from the Technion in Israel carried out a study, where he deposited golden islands onto a refractory underlay made out of titanium nitride. In his experiments he stressed the film with high current densities [14]. Due to the much higher resistivity of the underlayer the current mainly passed through the gold in the gold covered regions. By observing the movement of the islands he discovered a length dependent behavior. For long islands the edge, where the electrons pass into the gold, moved in the direction of the stripes with the velocity v_e

$$v_\mathrm{e} = \frac{D_\mathrm{a}|Z^*|e\rho j}{k_\mathrm{B}T}, \tag{2.7}$$

where D_a is the self diffusion coefficient, Z^* the effective valance, e the unit charge, ρ the specific electrical resistance, and j the current density. At the other side of the island extrusions were formed. For islands short enough the movement of the ends was not observed. For islands in between, the side, where the electrons entered, also moved with v_e but stopped after a certain time, when a critical length was reached. At the other end no extrusion was formed. *Blech* discovered a critical value for the product of current density j and the length l of the islands under which electromigration does not occur. This finding leads to the concept of the *Blech* length as a critical value for a given current density.

The explanation for this phenomenon was found in the fact that different densities of mass in the island lead to a mechanical back stress working against the electromigration force. This compression stress has to be below the critical value of extrusion forming. While the islands are in steady state, the back flux induced by the stress gradient is totally compensating the EM flux. This back flux is proportional to the gradient of the tensile stress. Therefore, the maximum stress divided by the island length l is proportional to the back flux. With the fact that the EM flux is proportional to the current j the following can be deduced.

$$\frac{\sigma}{l} \propto j \Rightarrow \sigma \propto (jl) \tag{2.8}$$

By taking a critical stress value into account a critical product $(jl)_\mathrm{c}$ follows [125, 142]. As the stress build-up due to electromigration in microelectronic structures is highly depending on the surrounding materials, on the physical design and on the fabrication process, the *Blech* length or product can hardly be pre-determined. Therefore, this concept was never seriously considered [95].

2.1.3. *Korhonen*'s Model

The coupling of the stress development with the vacancy dynamics was first introduced by *Korhonen et al.* [82]. They consider a thin narrow interconnect line deposited on a silicon oxide substrate covered by a dielectric passivation layer of infinite length. At moderate temperatures the electromigration induced flux is mainly flowing along the grain boundaries. Therefore the effective diffusion coefficient for the whole interconnect can be calculated by

$$D_\mathrm{eff} = \frac{\delta}{d} D_\mathrm{GB}, \tag{2.9}$$

where δ is the grain boundary width, d is the grain size, and D_GB is the grain boundary diffusion coefficient. However, in certain cases, like bamboo structures, the grain boundaries are nearly perpendicular to the line and the simplification of zero bulk flux from (2.9) is not applicable. A diffusion flux arises due to a difference in the chemical potential in the interconnect, which can be written [29, 57] by

$$\mu = \mu_0 - \Omega\sigma, \tag{2.10}$$

where Ω is the atomic volume and σ is the tensile stress. For thermal equilibrium of the vacancies μ_0 must be set to zero. The atomic flux including the electromigration induced flux is then represented by

$$J_\mathrm{a} = -\frac{D_\mathrm{a} C_\mathrm{a}}{k_\mathrm{B} T} \left(\frac{\partial \mu}{\partial x} + Z^* e E \right). \tag{2.11}$$

For the equilibrium concentration of the vacancies in the presence of stress *Korhonen et al.* [82] derived the equation

$$C_\mathrm{v} = C_\mathrm{v}^\mathrm{eq} \exp\left(\frac{\Omega \sigma}{k_\mathrm{B} T} \right), \tag{2.12}$$

which leads to the vacancy flux

$$J_\mathrm{v} = -D_\mathrm{v} \left(\frac{\partial C_\mathrm{v}}{\partial x} - \frac{Z^* e E}{k_\mathrm{B} T} C_\mathrm{v} \right) \tag{2.13}$$

and the conservation law for the vacancies

$$\frac{\partial C_\mathrm{v}}{\partial t} + \frac{\partial J_\mathrm{v}}{\partial x} + \gamma = 0, \tag{2.14}$$

where the γ added by *Clement* [26] represents a sink or source term. This model was extensively studied and presented in [26, 27, 28].

Under the assumption of a low vacancy concentration compared to the atomic concentration and climbing grain boundary dislocations consuming the net flux divergence, *Korhonen et al.* [82] developed a PDE for the build-up stress.

$$\frac{\partial \sigma}{\partial t} = \frac{\partial}{\partial x} D_\mathrm{a} B \left(\frac{\Omega}{k_\mathrm{B} T} \frac{\partial \sigma}{\partial x} + \frac{Z^* e E}{k_\mathrm{B} T} \right) \tag{2.15}$$

B is the applicable mechanical modulus for an aluminium line in a confined silicon matrix ranging form 0.5 to 0.75 times the *Young* modulus [82].

These equations were generalized for 3D calculations, allowing to simulate 3D structures which are more complex then straight interconnect lines. This formulation was used to investigate structures with grain boundaries explicitly given [118].

2.1.4. *Kirchheim*'s Fluxes

In the model presented in the previous chapter the stress is only included in the calculation of the equilibrium concentration of the vacancies. This was argued with the stress being in local equilibrium with the vacancy concentration. *Kirchheim* [76] added an extra driving force due to a gradient of the stress leading to the driving force approach allowing the stress and the concentration being out of equilibrium.

$$\boldsymbol{J}_{\mathrm{v},\sigma} = D_\mathrm{v} \frac{f \Omega}{k_\mathrm{B} T} C_\mathrm{v} \nabla \sigma \tag{2.16}$$

f is a relaxation factor. *Tan* and *Roy* [139] showed that the typical order of the stress induced flux and the electromigration induced flux are of the same order and therefore the flux driven by the stress gradient can not be neglected. An additional important physically induced flux is the flux due to a temperature gradient. This flux arises from the non-isothermal second *Fick* law [74].

$$\boldsymbol{J}_{\mathrm{v,th}} = \frac{D_{\mathrm{v}} Q^{*}}{k_{\mathrm{B}} T^{2}} \nabla T \tag{2.17}$$

Q^{*} stands for the heat of transport, which relates the temperature to the chemical energy by [114]

$$\mu_{T} = Q^{*} \ln T. \tag{2.18}$$

For the calculation of the stress in the structure, the volume change due to the sink/source γ has to be taken into account by [100]

$$\frac{1}{V}\frac{\partial V}{\partial t} = \Omega \left(1 - f\right) \gamma. \tag{2.19}$$

The state of the art model is entirely based on the physical phenomena and its mathematical description was developed by *Korhonen et al.* [82] and the extension of *Clement*'a [28] and *Kirchheim*'s [74] work.

2.1.5. Towards the State of the Art Model

The equations of *Kirchheim* are derived for one-dimensional problem sets and are therefore only capable to model straight lines. In these lines the values of the concentration, the stress etc. are assumed to be the same in every cross section. The extension of this equations by *Sarychev et al.* [116] to three-dimensional problems, while also taking the inelastic strain due to mass displacement into account, allows the simulation of EM in complex interconnect structures. Furthermore, the directional dependence of the diffusion was included by introducing a diffusion coefficient tensor. This constitutes a self-consistent model connecting the transport dynamics of the vacancies and the stress build-up in the conducting materials under EM.

Some extensions are required for interfaces like grain boundaries and interfaces to surrounding isolation or dielectric materials regarding, but not limited to, different diffusion coefficients. For instance, the segregation model of *Lau et al.* [90] was applied [22] to self diffusion and EM, furthermore, the *Fischer* model [42] was implemented to include a possible accumulation behavior of grain boundaries [4, 34].

The diffusion coefficients obeying an *Arrhenius* law were extended by a second dependence on the stress [136]. Also the equilibrium concentration of the vacancies was extended by an *Arrhenius* law [22, 55]. The full mathematics of the model PDE and the connecting quantities are presented in detail in Chapter 3.

2.2. Quantum Mechanical Electromigration Description

The force due to EM is modeled in continuum mechanical problems as described above by

$$\boldsymbol{F} = Z^* e \rho \boldsymbol{J}, \tag{2.20}$$

where the Z^* is called effective valence or effective charge. The EM induced force on an atomic scale was theoretically studied by *Huntington et al.* [64]. They used some simplifications, such as the defects are decoupled from the lattice, the electrons are scattered by atoms only, and the creation or annihilation of phonons is neglected. Under these assumptions the x-directional momentum transferred from the scattered electrons to the defects per time is given by

$$\frac{dM_x}{dt} = -\left(\frac{1}{4\pi^3}\right)^2 \iint \left(\frac{m_0}{\hbar}\right)\left(\frac{\partial E}{\partial k'_x} - \frac{\partial E}{\partial k_x}\right) f(\boldsymbol{k})(1-f(\boldsymbol{k}'))W_d(\boldsymbol{k},\boldsymbol{k}')\mathrm{d}\boldsymbol{k}\mathrm{d}\boldsymbol{k}', \tag{2.21}$$

where $f(\boldsymbol{k})$ is the distribution function of the electrons and $W_d(\boldsymbol{k},\boldsymbol{k}')$ is the transition probability per unit time of an electron in state $\boldsymbol{k}$ to jump into state $\boldsymbol{k}'$. By separating the two energies' differentiation into two integrals, interchanging the primed and the unprimed variables of the second integration, and employing the substitution

$$\frac{f\left(\boldsymbol{k}\right) - f_0\left(\boldsymbol{k}\right)}{\tau_a} = \int f(\boldsymbol{k})(1-f(\boldsymbol{k}'))W_d(\boldsymbol{k},\boldsymbol{k}') - f(\boldsymbol{k}')(1-f(\boldsymbol{k}'))W_d(\boldsymbol{k}',\boldsymbol{k})\frac{\mathrm{d}\boldsymbol{k}\mathrm{d}\boldsymbol{k}'}{4\pi^2} \tag{2.22}$$

equation (2.21) can be written in the form

$$\frac{dM_x}{dt} = \left(\frac{m_0}{\tau_a \hbar}\right) \int \frac{\partial E}{\partial k_x} f\left(\boldsymbol{k}\right) \frac{\mathrm{d}\boldsymbol{k}}{4\pi^3}, \tag{2.23}$$

where τ_a is the relaxation time of the electrons. As a common assumption for metals, the relaxation time is taken to be constant over all states $\boldsymbol{k}$. $f_0\left(\boldsymbol{k}\right)$ describes the electron distribution at equilibrium and integrates to zero. The current density in the x-direction can be expressed by [3, 78]

$$J_x = \frac{-e}{4\pi^2} \int f\left(\boldsymbol{k}\right) \frac{\partial E\left(\boldsymbol{k}\right)}{\hbar \partial k_x} \mathrm{d}\boldsymbol{k}. \tag{2.24}$$

By comparison of (2.21) and (2.24) the relation

$$\frac{\mathrm{d}M_x}{\mathrm{d}t} = \frac{J_x m_0}{e \tau_a} \tag{2.25}$$

is obtained. With the density of defects N_a, the density of the conducting electrons n, and the contribution of the defects to the resistivity $\rho_d = |m^*|/ne^2\tau_a$ the force can be expressed by

$$F_{\text{wind}} = -\frac{neJ_x\rho_\mathrm{d} m_0}{N_\mathrm{d}|m^*|} = -eE_x z \frac{N\rho_\mathrm{d}}{\rho N}\frac{m_0}{|m^*|}, \tag{2.26}$$

where the density of the conducting electrons is substituted by $n = zN$, where N is the density of the lattice atoms, and z is the number of conducting electrons per lattice atom. For an ion at a saddle point between two vacant position the interaction of the ion and the conducting electron is the strongest, whereas the interaction at lattice points is the weakest. On the way from one lattice point to an other the interaction varies and as this position dependent interaction is not known, *Huntington et al.* [64] chose a sinusoidal form leading to

$$\boldsymbol{F}(y) = \boldsymbol{F}_{\mathrm{m}} \sin^2\left(\frac{\pi y}{a}\right), \tag{2.27}$$

where a is the jump distance, and $\boldsymbol{F}_m$ is the maximum force. For a jump path j with an angle θ_j between the path and the force $\boldsymbol{F}_m$, the energy required for a jump can be calculated by

$$\Delta V_j = \int_0^{\frac{a_j}{2}} \boldsymbol{F}(y) \cdot \mathrm{d}\boldsymbol{y} = \frac{1}{4} a_j F_{wind} \cos\theta_j. \tag{2.28}$$

The net flow of atoms due to EM in the current direction is the sum of the probabilities of jumps (along the paths j) times the jump length in the current direction [78].

$$J_{\mathrm{wind}} = \sum_j C\nu_0 \exp\left(-\frac{V}{k_{\mathrm{B}}T}\right) a_j \cos(\theta_j) \sinh\left(\frac{\Delta V_j}{k_{\mathrm{B}}T}\right) \tag{2.29}$$

ν_0 is the atomic vibration frequency, C the concentration of the ions in the metal, and V the saddle point energy including the formation energy and the motion energy of vacancies. This equation can be linearized and rewritten to

$$J_{\mathrm{wind}} = \frac{cDF_{wind}}{2k_{\mathrm{B}}T} \tag{2.30}$$

with D being the diffusion coefficient.

$$D = \frac{1}{2}\nu_0 \exp\left(-\frac{V}{k_{\mathrm{B}}T}\right) \sum_j a_j^2 \cos(\theta_j) \tag{2.31}$$

The resulting equation (2.30) differs form the *Nernst-Einstein* relation by the factor 2 in the denominator, which is the average of the chosen position dependent interaction of the conducting electrons and the ions on their path from one lattice point to an other. In addition to the force due to the electron wind also the force due to the electric potential gradient has to be included, leading to the effective charge

$$e' = eZ^* = ez\left(\frac{1}{2}\left(\frac{\rho_{\mathrm{d}} N}{\rho N_{\mathrm{d}}} \frac{m_0}{|m^*|}\right) - 1\right) \tag{2.32}$$

and to the effective valence Z^*. Using the *Einstein* relation for field assisted diffusion in a potential the drift velocity can be expressed by [94]

$$v_{\mathrm{EM}} = \frac{DF}{k_{\mathrm{B}}T} = \frac{DZ^* e\rho J_x}{k_{\mathrm{B}}T}. \tag{2.33}$$

This was the first quantum mechanical expression of the EM induced ion velocity. Within the ballistic model [96] it was shown that there is a linear relation between the EM induced flux and the current density.

For a quantum mechanical force calculation another equation was developed and widely used, based on the scattering states of the conducting electrons [15, 117, 124, 132, 128] obtained from the linear response theory of *Kubo* [84],

$$\boldsymbol{F}_{\text{wind}} = \frac{e\Omega}{4\pi^3}\left[\iint\limits_{\text{FS}} \frac{\mathrm{d}^2\boldsymbol{k}}{|\nabla E_{\boldsymbol{k}}|}\tau_{E_{\boldsymbol{k}}}\boldsymbol{v}_{\text{F}}\left(\boldsymbol{k}\right)\iiint \psi^{*}_{\boldsymbol{k}}\left(\boldsymbol{r}\right)\nabla_{\boldsymbol{R}}V\left(|\boldsymbol{R}-\boldsymbol{r}|\right)\psi_{\boldsymbol{k}}\left(\boldsymbol{r}\right)\mathrm{d}^3\boldsymbol{r}\right]\cdot\boldsymbol{E}. \tag{2.34}$$

The considered atom is located at position $\boldsymbol{R}$ and $V\left(|\boldsymbol{R}-\boldsymbol{r}|\right)$ is the effective one-electron potential. $\boldsymbol{E}$ is the electric field, Ω is the volume of the unit cell, τ_E is the relaxation time of the scattered electron, $\boldsymbol{v}_{\text{F}}\left(\boldsymbol{k}\right)$ is the k-dependent *Fermi* velocity, and ψ_k is the wave function of the electron, which can be calculated with the *Schröedinger* equation [37]

$$-\frac{1}{2}\nabla^2\psi_{\boldsymbol{k}} + V\left(\boldsymbol{r}\right)\psi_{\boldsymbol{k}}\left(\boldsymbol{r}\right) = E_{\boldsymbol{k}}\psi_{\boldsymbol{k}}\left(\boldsymbol{r}\right) \tag{2.35}$$

In (2.34) the first part on the right hand side has the meaning of the effective charge, has the form of a tensor of second order, and reflects the possible dependence of the crystal orientation on the current direction of the EM force especially for non-cubic crystal metals (e.g. zinc) [59]. For periodic structures the integral (2.34) is always equal 0. The reason is the symmetry of the wave functions regarding the crystal wave vector

$$\psi_{\boldsymbol{k}}\left(\boldsymbol{x}\right) = \psi^{*}_{-\boldsymbol{k}}\left(\boldsymbol{x}\right), \tag{2.36}$$

making the result of the integration over space an even function in $\boldsymbol{k}$ due to the fact that the potential is a real valued function,

$$\iiint \psi^{*}_{\boldsymbol{k}}\left(r\right)\nabla_{R}V\left(|R-r|\right)\psi_{\boldsymbol{k}}\left(r\right)\mathrm{d}^3\boldsymbol{r} = \iiint \psi^{*}_{-\boldsymbol{k}}\left(r\right)\nabla_{R}V\left(|R-r|\right)\psi_{-\boldsymbol{k}}\left(\boldsymbol{r}\right)\mathrm{d}^3\boldsymbol{r}. \tag{2.37}$$

Furthermore, the *Fermi* velocity is an odd function in $\boldsymbol{k}$ leading to a vanishing result of the integration over the *Fermi* sphere. This causes the necessity of calculations of non-periodic problems. For bulk materials the calculations were performed using the pseudo potential and the KKR method [129, 130, 131, 144, 145]. *Bly et al.* [15, 111, 112] showed how a calculation for a single adatom can be carried out by employing the LKKR method [97, 98]. They used the muffin-tin approximation by confining the atomic potential to non-overlapping spheres with a constant interstitial potential [101]. The advantage of this method is the simplicity and the computational economy payed by an insufficient description of valence electron potentials in covalent open structures [147] compared to full potential calculations [105] The electron wave function was defined by

$$\psi_{\boldsymbol{k}}\left(\boldsymbol{r}\right) = \frac{4\pi}{\sqrt{\Omega}}\sum_{lm} i^l A_{lm}\left(\boldsymbol{k}\right)R_l\left(\boldsymbol{r}\right)Y_{lm}\left(\boldsymbol{r}\right), \tag{2.38}$$

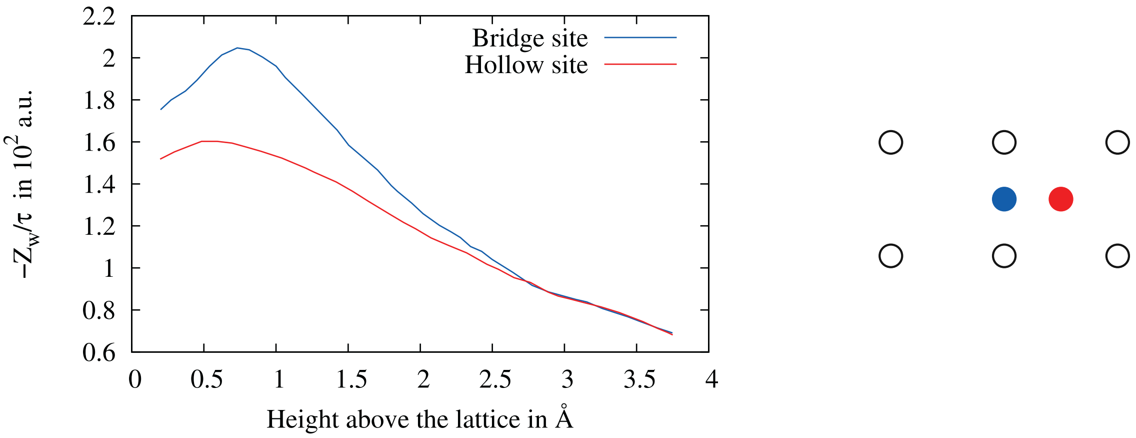

Figure 2.1.: The dependence of the effective valence on the distance of an adatom to a semi-infinite metal surface for two different location above the crystal lattice shown on the right [15]. τ is the time scale of relaxation of the electronic charge density.

where $Y_{lm}(\boldsymbol{r})$ is a spherical harmonic [150], $A_{lm}(\boldsymbol{k})$ is the coefficient from the spherical wave expansion, evaluated by the LKKR calculation, and $R_l(\boldsymbol{r})$ is the spherical solution of the *Schrödinger* equation [141], which can be expressed as

$$R_l(\boldsymbol{r}) = \left(j_l(\kappa\boldsymbol{r}) + h_l^{(1)}(\kappa\boldsymbol{r})\right) i e^{i\delta_l^a} \sin\left(\delta_l^a\right). \tag{2.39}$$

Here $\kappa = \sqrt{2E_{\boldsymbol{k}}}$, j_l is a spherical *Bessel* function [150], $h_l^{(1)}$ is the spherical *Henkel* function [150] of the first kind, and δ_l^a characterizes the scattering phase shift of each atom. The results show that the effective valance of an adatom is strongly dependent on the height of the atom relative to the metal surface (c.f. Figure 2.1). This dependence is quite well described by a simple ballistic model, if the reduced electron density relative to the bulk is taken into account [15]. This calculation was extended to islands of adatoms on a substrate modeled by the jellium model showing that the distance to islands has a huge impact on the effective valance of single adatoms [113].

Chapter 3

Models

In this section the models used for the analysis of the failure mechanisms are described. In Section 3.1 the electro-thermal model is explained followed by the different EM models regarding bulk metals, interfaces between conducting materials, and the mechanical model for elastic materials influenced by plastic deformation due to EM induced material transport. This section is followed by the elucidation of void nucleation. The last section of this chapter deals with the evolution model which gives the ability to track the cross section reduction and thereby the resistance development in interconnect structures.

3.1. Electro-Thermal Model

For an ohmic material the current density and the electrical field is linearly related by the conductivity σ_E.

$$\mathbf{J} = \sigma_{\mathrm{E}}\mathbf{E} \tag{3.1}$$

For a conservative electrical field the field can be expressed as the gradient of an electrical potential ϕ_{E}.

$$\mathbf{E} = -\nabla\phi_{\mathrm{E}} \tag{3.2}$$

Inserting (3.2) into (3.1) and applying the divergence results in [138]

$$\nabla \cdot \mathbf{J} = -\nabla \cdot \left(\sigma_{\mathrm{E}}\nabla\phi_{\mathrm{E}}\right). \tag{3.3}$$

The left side of this equation must be 0 in a charge free region due to the conservation of charge. Under the assumption of a constant conductivity the equation can be simplified to *Laplace*'s equation [66].

$$\nabla^2\phi_{\mathrm{E}} = 0 \tag{3.4}$$

For interfaces with normal vector $\mathbf{n}$ between a conducting material and a non-conducting material the current density has to vanish and obey therefore

$$\mathbf{J} \cdot \mathbf{n} = 0. \tag{3.5}$$

Applying (3.4) results in

$$\frac{\partial \phi_{\mathrm{E}}}{\partial n} = 0. \tag{3.6}$$

The heat flow in materials can be written in the form [121]

$$\rho_{\mathrm{M}} c_{\mathrm{T}} \frac{\partial T}{\partial t} = \nabla \cdot (\lambda_{\mathrm{T}} \nabla T) + \dot{q}, \tag{3.7}$$

where ρ_{M} is the material density, c_{T} is the specific heat capacity, λ_{T} is the thermal conductivity, and $\dot{q}$ is the heat generation per time. The heat generated in interconnect systems is the *Joule* heat given by

$$\dot{q} = \mathbf{J} \cdot \mathbf{E} = \sigma_{\mathrm{E}} |\mathbf{E}|^2 = \sigma_{\mathrm{E}} |\nabla \phi_{\mathrm{E}}|^2. \tag{3.8}$$

3.2. Electromigration in Bulk Metals

The mass transport due to electromigration is modeled as the flow of vacancies. First the equations for EM in bulk were written in this form in [116] and further developed in [34, 136]. The governing equation of the vacancy concentration is given by the conservation law

$$\frac{\partial C_{\mathrm{v}}}{\partial t} = -\nabla \cdot \mathbf{J}_{\mathrm{v}} + G, \tag{3.9}$$

with a flow term and a generation/annihilation term. The flow is the sum of the four flows driven by diffusion, by EM, a gradient of the pressure, and a gradient of the temperature distribution.

$$\mathbf{J}_{\mathrm{v}} = \mathbf{J}_{\mathrm{D}} + \mathbf{J}_{\mathrm{EM}} + \mathbf{J}_{\mathrm{S}} + \mathbf{J}_{\mathrm{T}} \tag{3.10}$$

The first flow contribution is a diffusion induced flow expressed by

$$\mathbf{J}_{\mathrm{D}} = -\mathbf{D}_{\mathrm{v}} \cdot \nabla C_{\mathrm{v}}, \tag{3.11}$$

where $\mathbf{D}_{\mathrm{v}}$ is the diffusion coefficient tensor. This coefficient is in general a tensor of second order as shown in Section 2.2.

The second component is the electromigration induced flow given by

$$\mathbf{J}_{\mathrm{EM}} = \mathbf{D}_{\mathrm{v}} \cdot \frac{|Z^*| e}{k_{\mathrm{B}} T} C_{\mathrm{v}} \mathbf{E}, \tag{3.12}$$

where Z^* is the effective valence, e is the elementary charge, k_{B} the *Boltzmann* constant, T the temperature, and $\mathbf{E}$ the electrical field.

Due to a gradient in the hydraulic pressure σ a flux is driven which is modeled by the third term as

$$\mathbf{J}_{\mathrm{S}} = -\mathbf{D}_{\mathrm{v}} \cdot \frac{f \Omega}{k_{\mathrm{B}} T} C_{\mathrm{v}} \nabla \sigma \tag{3.13}$$

with f being the relation between the volume of a vacancy and the volume of an atom Ω. Therefore, f is in the range between zero and one. For the crystal lattice of metals the ratio is in the range of $f = 0.2 - 0.4$ [39, 41].

The fourth term is the flow driven by temperature gradient.

$$\mathbf{J}_\mathrm{T} = \mathbf{D}_\mathrm{v} \cdot \frac{Q^*}{k_\mathrm{B} T^2} C_\mathrm{v} \nabla T \tag{3.14}$$

For vacancies there is an equilibrium concentration to which the concentration converges in the absence of any outer perturbation. This phenomenon is modeled by the so called *Rosenberg-Ohring* term [21, 110].

$$G = \frac{C_\mathrm{v,eq} - C_\mathrm{v}}{\tau} \tag{3.15}$$

$C_\mathrm{v,eq}$ is the equilibrium concentration and τ is the characteristic relaxation time of the vacancy concentration. The equilibrium concentration depends on the temperature according to an *Arrhenius* law [102]

$$C_\mathrm{v,eq} = C_\mathrm{v,0} \mathrm{e}^{-\frac{E_\mathrm{a}}{k_\mathrm{B} T}}. \tag{3.16}$$

3.3. Electromigration at Interfaces

Interfaces regarding EM are the domains which connect either bulk metal domains of the same metal kind or bulk materials of two different kinds. In the second case the interface can separate two conducting materials or a conducting material from a non-conducting material. In all three cases the interface can have a diffusion coefficient higher then the coefficient of the bulk material or a lower equilibrium concentration. How to handle this behavior is shown in the two next subsections. This is followed by a subsection explaining the case of an interface between two conducting materials, where the interface can have a segregation behavior.

3.3.1. Fast Diffusivity Paths at Interfaces

The crystal structure is highly disturbed at interfaces as there crystals with different orientations or even crystals with other lattice kinds or lattice parameters meet. This leads to atoms with a decreased binding energy compared to the atoms located in the undisturbed lattice of a bulk material. This increases the probability for those atoms to jump and therefore increases also the diffusion coefficient as shown by *Sørensen et al.* [133]. This jumping is limited by the two-dimensional plane of the interface embedded in the 3D space. Therefore, interfaces show a highly direction depending diffusion coefficient giving it the form of a second order tensor. Since for interfaces the real thickness can hardly be defined, for simulation normally the interface is modeled by a domain with a small but finite thickness. As a smaller thickness leads to a higher amount of mesh elements to ensure a reasonable mesh quality, a thicker layer is desired. For these reasons in the further description of the modeling of fast diffusivity paths a thickness δ is chosen to be the modeled interface thickness and its influence is pointed out.

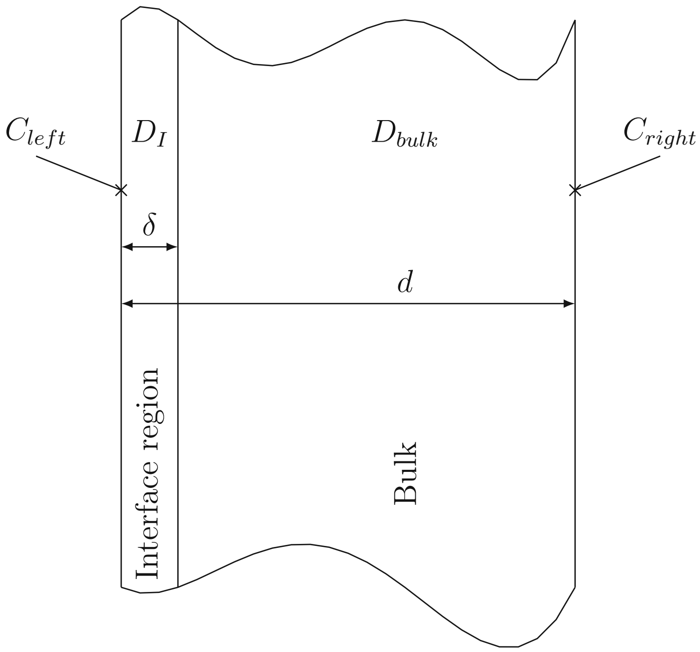

Figure 3.1.: Segment with an interface domain and a neighboring bulk domain for the diffusion coefficient calculation.

In Section 2.1.3 the effective diffusion coefficient was calculated by (2.9), where the diffusion in the bulk was taken to be negligibly small compared to the diffusion in the GB. Extending this equation for a finite diffusion coefficient in the bulk leads to the expression for the effective diffusion coefficient [136] for a structure shown in Figure 3.1 with an interface and an bulk segment.

$$D_{\text{eff}} = \frac{\delta}{d} D_{\text{I}} + \frac{d-\delta}{d} D_{\text{bulk}} \tag{3.17}$$

If the effective diffusion coefficient is known from experimental data this equation can be rearranged to

$$D_{\text{I}}(\delta) = D_{\text{bulk}} + \frac{d}{\delta}\left(D_{\text{eff}} - D_{\text{bulk}}\right), \tag{3.18}$$

giving a functional dependence on the interface thickness and the interface diffusion coefficient.

This value is the diffusion coefficient in the directions parallel to the interface surface, whereas the value perpendicular to the interface surface is given by the bulk diffusion coefficient, leading to a tensor form of the diffusion coefficient. For very small interface thicknesses this distinction of the direction is not needed, shown by the following gedankenexperiment. The flow of vacancies perpendicular to the interface is calculated for the structure shown in Figure 3.1 for predetermined vacancy concentrations at the left and right side of the structure in the following way:

$$J_{\text{D}} = D\frac{\partial C_v}{\partial x} \tag{3.19}$$

$$\Delta C_v = C_{v,\text{right}} - C_{v,\text{left}} = \int\limits_{\text{right}}^{\text{left}} \frac{J}{D\left(x\right)} \mathrm{d}x \tag{3.20}$$

For the case of an infinite small interface ($\delta \rightarrow 0$) this leads to

$$\Delta C_{v,\delta\rightarrow 0} = J_{\delta\rightarrow 0} \frac{d}{D_\text{bulk}}, \tag{3.21}$$

whereas for a finite interface it results in

$$\Delta C_{v,\delta} = J_\delta \left(\frac{d-\delta}{D_\text{bulk}} + \frac{\delta}{D_\text{I}} \right). \tag{3.22}$$

Setting both equations to the concentration difference assumed at the beginning, substituting D_I form (3.18) and calculating the relative error gives

$$\epsilon = \frac{J_\delta + J_{\delta\rightarrow 0}}{J_{\delta\rightarrow 0}} = \frac{\delta\left(D_\text{eff} - D_\text{bulk}\right)}{d\left(-D_\text{eff} + D_\text{bulk}\right) + \delta\left(D_\text{eff} - 2D_\text{bulk}\right)}, \tag{3.23}$$

and establishes a rule under which the directional dependence of the diffusion can be neglected.

3.3.2. Interfaces with Lower Equilibrium Concentrations

Interfaces can have, due to their disorder, a lower vacancy equilibrium concentration, as in the bulk, where vacancies can be easily filled by surrounding atoms as their binding energy is lower there. This is modeled by an extra region with a lower equilibrium concentration between the bulk materials in the *Rosenberg-Ohring* term inside the domain in contrast to the surrounding domains. This phenomenon is particularly important at interfaces between voids and bulk materials, as there at one side a lattice is formed, whereas on the other side no material is present. Therefore, this behavior is given special attention in the phase field model for voids in Section 3.6.

3.3.3. Segregation Model

Surfaces between different conducting materials play a special role in EM. The current at these interfaces passes from one conducting material to another. But for vacancies passing the interface can be hindered leading to a segregation in the vicinity of those interfaces. The segregation at interfaces was modeled by *Lau et al.* [90] based on the work of *Grove et al.* [52]. The interface in this model makes use of a trap density T, where the filled traps are denoted by T_d and the empty ones by T_0. These traps are dynamically coupled to the bulk materials' concentrations C_1 and C_2 by the flows

$$F_1 = t_1 T_0 C_1 - e_1 T_\text{d} \tag{3.24}$$

and

$$F_2 = t_2 T_0 C_2 - e_2 T_\text{d}, \tag{3.25}$$

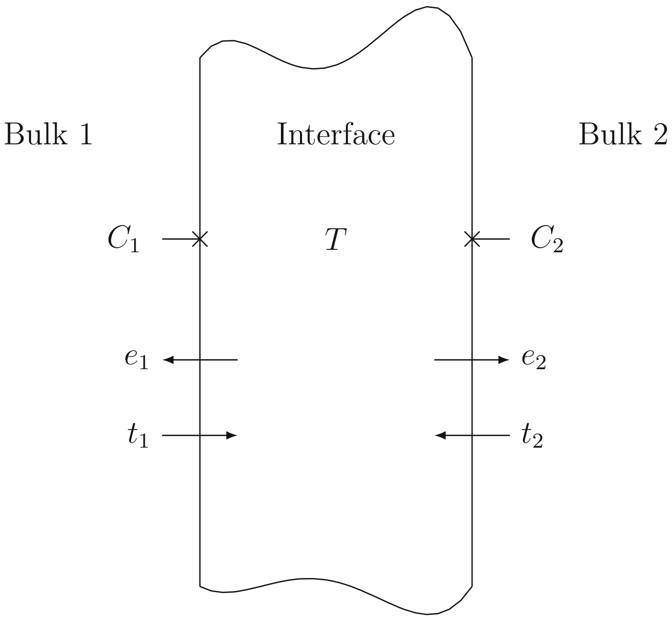

Figure 3.2.: Schematics for the derivation of the segregation model according to [90].

respectively, where the e_i are the emission probabilities and t_i are the trapping probabilities. These equations can be put together to calculate the time derivative of the filled trap density T_d by

$$\frac{\partial T_\mathrm{d}}{\partial t} = F_2 + F_1 = t_2 T_0 C_2 - e_2 T_\mathrm{d} + t_1 T_0 C_1 - e_1 T_\mathrm{d}. \tag{3.26}$$

With the assumption of an equilibrium, where the filled trap density is constant in time, (3.26) can be rearranged to

$$T_0 \left(t_2 C_2 + t_1 C_1\right) = T_\mathrm{d} \left(e_2 + e_1\right). \tag{3.27}$$

Using the fact that the filled and the empty traps are the sum of the total traps density

$$T = T_\mathrm{d} + T_0, \tag{3.28}$$

leads to the filled trap density

$$T_\mathrm{d} = \frac{T\left(C_1 + C_2\alpha\right)}{C_1 + C_2\alpha + \beta}, \tag{3.29}$$

where α and β are given by

$$\alpha = \frac{t_2}{t_1} \tag{3.30}$$

$$\beta = \frac{e_1 + e_2}{t_1}. \tag{3.31}$$

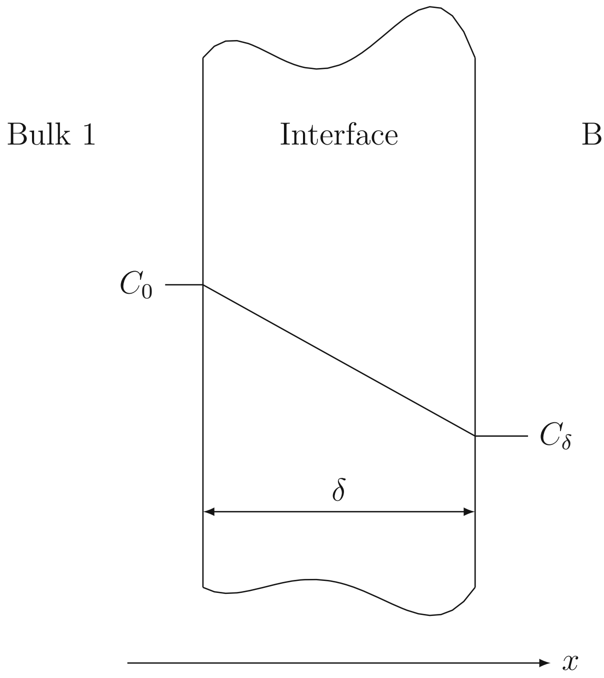

Figure 3.3.: Schematics for the derivation of the segregation model as an infinite thin representation of an interface with δ thickness.

Inserting the filled trap density in the flow equations (3.24) and (3.25) keeping in mind (3.28) results in

$$F = F_1 = -F_2 = T \frac{t_1 e_2}{t_1 C_1 + t_2 C_2 + e_2 + e_1} \left(C_1 - \frac{e_1 t_2}{e_2 t_1} C_2 \right) = h \left(C_1 - m C_2 \right), \tag{3.32}$$

with h named the transport coefficient, and m the segregation coefficient. In the calculations the segregation coefficient is taken to be constant.

In the following it is shown that the segregation model can also be used for an infinitely thin representation of a domain with a thickness δ and a diffusion coefficient D_I, if m is set to one. As the domain thickness is small compared to a characteristic length (e.g. grain radius) the concentration profile in this thin domain can be approximated with the first order *Taylor* expansion (c.f. Figure 3.3)

$$C(x) = C_0 + \frac{x}{\delta} \left(C_\delta - C_0 \right), \tag{3.33}$$

where C_0 can be identified as the concentration in the left bulk material equaling C_1 and C_δ as the concentration in the right bulk material C_2. Differentiation of (3.33) with respect to x and putting the result in the flux driven by diffusion (cf. (3.11)) regarding only the x direction leads to

$$J_{\mathrm{D},2\to 1} = \frac{D_{\mathrm{I},x}}{\delta} \left(C_2 - C_1 \right), \tag{3.34}$$

giving exactly the result of the segregation model shown above. It should be emphasized that this interface has in the limit of an infinitely small thickness no capability to store any vacancies, as all the flow from the left side is compensated by an equal flow on the right side. This behavior has to be taken into account as for mechanical stress calculations in FEM there is no easy way to handle a volume decrease due to the pile-up of vacancies in infinitely thin interfaces exhibiting zero volume.

3.4. Continuum Mechanical Model

The vacancy flux due to the mechanisms described above and the generation and annihilation of vacancies has an influence on the stress inside the structure, as the volume is smaller for vacancies then for atoms. The ratio of the atom volume and the vacancy volume is represented by f. Therefore the inelastic strain due to vacancy flow is given by

$$\frac{\partial \epsilon^{\mathrm{v}}_{\mathrm{flow},ij}}{\partial t} = \Omega\left(1-f\right)\nabla\cdot\mathbf{J}_{\mathrm{v}}\delta_{ij}, \tag{3.35}$$

where the negative divergence of the vacancy flux, representing an accumulation of vacancies, leads to a contraction of the material. For the generation/annihilation term inelastic strain is built up due to the creation of a lattice position where no atom is present, occupying a volume of $f\Omega$ leading to the tensor components of the inelastic strain

$$\frac{\partial \epsilon^{\mathrm{v}}_{\mathrm{G},ij}}{\partial t} = \Omega f G \delta_{ij}. \tag{3.36}$$

These equations connect the solid mechanics to the vacancy dynamics. The solid mechanics model is given by *Hook*'s law

$$\boldsymbol{\sigma} = \mathbf{S} : \left(\boldsymbol{\epsilon} - \boldsymbol{\epsilon}^{\mathrm{v}} - \boldsymbol{\epsilon}^{\mathrm{T}}\right), \tag{3.37}$$

where the inelastic strain due to thermal expansion is already included and **S** stands for the elastic tensor with its components given by

$$S_{ijkl} = \lambda\delta_{ij}\delta_{kl} + \mu\left(\delta_{il}\delta_{jk} + \delta_{ik}\delta_{jl}\right) \tag{3.38}$$

where μ and λ are the *Lamé* parameters. The components of the strain tensor of the thermal expansion are given by

$$\epsilon^{\mathrm{T}}_{ij} = \alpha_{\mathrm{T}}\left(T - T_{\mathrm{ref}}\right)\delta_{ij}, \tag{3.39}$$

where α_{T} is the thermal expansion coefficient. The connection between the strain tensor and the displacement field is given component-wise by

$$\epsilon_{ij} = \frac{1}{2}\left(\frac{\partial u_i}{\partial x_j} + \frac{\partial u_j}{\partial x_i}\right). \tag{3.40}$$

The momentum conservation is expressed by

$$\rho\frac{\partial^2\mathbf{u}}{\partial t^2} - \nabla\cdot\boldsymbol{\sigma} = \mathbf{f}_{\mathrm{body}}, \tag{3.41}$$

where $\mathbf{f}_{\text{body}}$ is the body force density, the first term stands for the acceleration according to *Newton*'s law, and the second is the force due to the stress in the structure. For EM calculations the only body force is gravity and can be neglected. Furthermore, the accelerations in the structure are low and negligible leading to

$$\nabla \cdot \boldsymbol{\sigma} = \mathbf{0}. \tag{3.42}$$

Putting (3.36), (3.37), and (3.39) into the equation above leads to the mechanical problem for the displacement field $\mathbf{u}$.

$$\mu \nabla^2 u_i + (\lambda + \mu) \frac{\partial}{\partial x_i} (\nabla \cdot \mathbf{u}) = \frac{\mu(3\lambda + 2\mu)}{\lambda + \mu} \frac{\partial}{\partial x_i} \operatorname{Tr} \left(\boldsymbol{\epsilon}^{\text{v}} + \boldsymbol{\epsilon}^{\text{T}} \right) \tag{3.43}$$

3.5. Void Nucleation

In early days void nucleation was understood as a vacancy condensation in the structure. For the vacancy condensation an unrealistic high concentration of the vacancies is needed to reach the supersaturation for condensation. Therefore, the process of condensation under classical thermodynamics can not be responsible for the void nucleation due to EM [49].

In contrast to the process of void nucleation mentioned above, various authors have determined the cause for void nucleation by the excess of the mechanical stress over a critical threshold [34]. *Gleixner et al.* [49] investigated nucleation rates within an interconnect line and gave a formula for the free energy F change due to the void formation in aluminium.

$$\Delta F = -\sigma V_{\text{void}} + \gamma_{\text{Al}} A_{\text{Al}} \tag{3.44}$$

V_{void} is the volume of the void, A_{Al} the area, σ the hydraulic pressure, and γ_{Al} the surface energies of aluminium. The first part stands for the energy freed by the dissipation of the elastic strain energy and the second denotes the energy consumed by the creation of new surfaces. The calculations of *Gleixner et al.* [49] revealed small rates for nucleation at grain boundaries, at interfaces of metals and surrounding isolation layers, and even at grain boundary intersecting metal/isolation interfaces. Therefore, this mechanism can be responsible for void nucleation.

Nevertheless, the nucleation of voids at interfaces between a isolation layer and a metal are frequently observed at positions where they intersect with grain boundaries. This phenomenon was resolved by *Flinn* [43], who assumed that the void forms at preexisting free surfaces. Free surfaces are formed due to contamination, while the line is fabricated. This contamination lowers the adhesion between the metal and the isolation layer. Based on this assumption, he derived a threshold stress σ_{th} for a flaw of the radius R_{p}.

$$\sigma_{\text{th}} = \frac{2\gamma_{\text{s}}}{R_{\text{p}}} \tag{3.45}$$

Clemens et al. [25] showed that the formula of *Flinn* is only valid as long as the void grows on the free surface of the contaminated region. As the void grows further beyond the flaw area, the contact angle θ_c is in the range $0 < \theta_\mathrm{c} < 90°$ leading to a reduced threshold stress given by

$$\sigma_\mathrm{th} = \frac{2\gamma_\mathrm{s} \sin\theta_\mathrm{c}}{R_\mathrm{p}}. \tag{3.46}$$

Both equations show an inverse dependence of the threshold stress on the flaw radius. The stress required to form a void is in the order of $350\mathrm{MN/m^2}$ and can therefore be reached by the mechanical stress build-up by thermal stress [21]. For bigger flaw radii in the range of 100nm the threshold stress is in the range of $70\mathrm{MN/m^2}$ and can therefore also be built up by EM [34, 50].

3.6. Void Evolution

The void evolution phenomenon causes degradation by increasing the resistance of an interconnect after the void has nucleated. This process is modeled by equations tracking the movement of an interface, representing the boundary between the interconnect metal and the void [73]. For the calculations *Bhate et al.* [8, 9] introduced a local coordinate system at the void surface (shown in Figure 3.4). The chemical potential of the surface, when no current is present, is given by [58]:

$$\mu_\mathrm{s} = \Omega\left(-\gamma_\mathrm{s}\kappa + W\right) \tag{3.47}$$

κ is the surface curvature, γ_s is the surface energy, and W is the elastic strain energy density.

$$W = \frac{1}{2}\boldsymbol{\epsilon} : \boldsymbol{\sigma} = \frac{1}{2}\boldsymbol{\epsilon} : \mathbf{C}\boldsymbol{\epsilon} \tag{3.48}$$

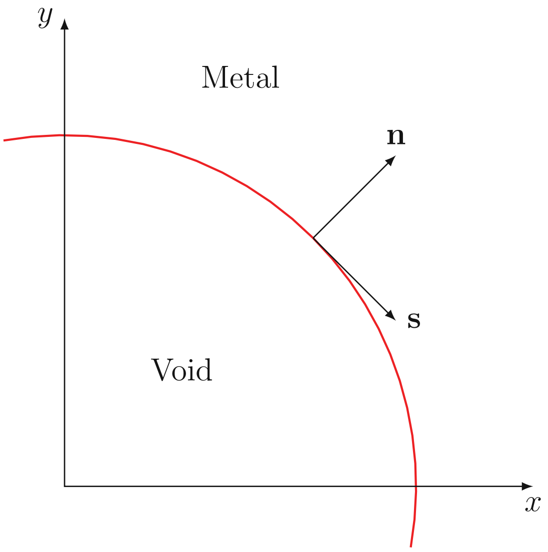

Figure 3.4.: Local coordinate system.

The “double-dot” operator is defined for the tensors **A** and **B** by

$$\mathbf{A} : \mathbf{B} = \sum_{i,j} A_{ij} B_{ij} \tag{3.49}$$

and A_{ij}, B_{ij} stands for the components of the tensor **A** and **B**, respectively. The flux parallel to the surface is driven by the chemical potential of the surface and the EM flux summing up to

$$J_\mathrm{s} = -\frac{D_\mathrm{s}\delta_\mathrm{s}}{k_\mathrm{B}T}\left(\frac{\partial \mu_\mathrm{s}}{\partial s} - eZ^* \frac{\partial \phi_\mathrm{E}}{\partial s}\right), \tag{3.50}$$

where the derivatives are taken along the interface and the surface diffuse coefficient D_s obeys an *Arrhenius* law

$$D_\mathrm{s} = D_\mathrm{s,0} \exp\left(-\frac{E_\mathrm{A}}{k_\mathrm{B}T}\right). \tag{3.51}$$

Furthermore, a flux normal to the surface due to a flow of vacancies from the bulk to the surface, reasoned by the difference of the chemical potentials in the bulk and at the surface, is given by

$$J_\mathrm{nv} = \hat{D}\left(\mu_\mathrm{bv} - \mu_\mathrm{sv}\right), \tag{3.52}$$

where $\hat{D}$ controls the rate of vacancy exchange between the bulk and the surface. For the chemical potential of the vacancies at the surface the negative chemical potential of the surface is taken as given by (3.47). For the bulk the chemical potential is given by:

$$\mu_\mathrm{bv} = k_\mathrm{B}T \ln\left(\frac{C_\mathrm{v}}{C_\mathrm{v,eq}}\right) - (f-1)\,\Omega\sigma \tag{3.53}$$

Given these equations and considering the mass conservation the normal velocity of the void surface can be expressed as:

$$v_\mathrm{n} = -\frac{\partial J_\mathrm{s}}{\partial s} - J_\mathrm{nv} \tag{3.54}$$

A problem with this model arises from the need to track the interface for every simulation time step, if the FEM is employed as the simulation domains have to be separated in a void region and a metal region and these regions change in shape. The metal region has to be remeshed for every time step, increasing the simulation complexity. Therefore a model was proposed by *Bhate et al.* [9] according to *Cahn et al.* [19], where the boundary between the void and the metal is not modeled by a sharp interface, but by a thin region called the diffuse interface. To distinguish between the three regions a function called the order parameter $\phi(\vec{x}, t)$ is defined, which has the property to be 1 in the metal decreasing smoothly in the interface region and being -1 in the void region. The free energy functional is defined by

$$\mathcal{F}(\phi, \boldsymbol{\epsilon}) = \int F(\phi, \nabla\phi, \boldsymbol{\epsilon})\,\mathrm{d}V \tag{3.55}$$

$$= \int \left(\frac{2\gamma_\mathrm{s}}{\epsilon_\mathrm{pf}\pi}\left(f(\phi) + \frac{1}{2}\epsilon_\mathrm{pf}^2|\nabla\phi|^2\right) + W(\boldsymbol{\epsilon}, \phi)\right)\mathrm{d}V, \tag{3.56}$$

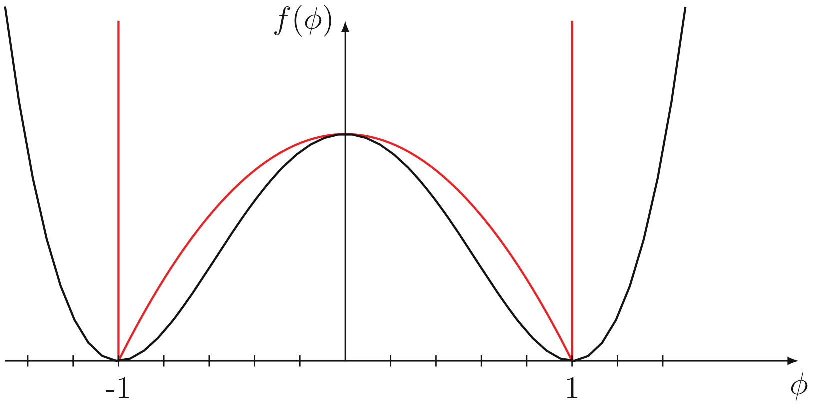

Figure 3.5.: Two shapes proposed for the bulk free energy function $f(\phi)$. The quadratic double well potential in black and the double obstacle potential in red.

where $W(\boldsymbol{\epsilon}, \phi)$ is the elastic strain energy density given by

$$W(\boldsymbol{\epsilon}, \phi) = \frac{1}{2}\boldsymbol{\epsilon} : \mathbf{C}(\phi)\,\boldsymbol{\epsilon} \tag{3.57}$$

and $f(\phi)$ is the bulk free energy function. The shape of this function has to meet the requirements to be positive everywhere and zero for ϕ equaling one or minus one. Two shapes proposed by different authors are shown in Figure 3.5. The black line is the quadratic double well potential proposed by *Mahadevan et al.* [99]. The red line is the double obstacle potential proposed by *Oono et al.* [106]. This potential was employed by *Bhate et al.* [9] in a calculation utilizing the finite-difference method, as it reduces the computational effort only to those areas, where the interface is located and the potential has a finite value. The second term in the energy functional stands for the energy cost due to a gradient of the phase field. ϵ_{pf} is the parameter which controls the thickness of the interface and has therefore to be chosen carefully, taking into account the meshing diameter and the minimum curvatures of the interface which can occur.

From this energy functional the chemical potential can be calculated by [36] employing the variational principle [53, 54].

$$\mu_\phi = 2\Omega \frac{\delta \mathrm{F}}{\delta \phi} \tag{3.58}$$

$$= 2\Omega \left(\frac{\partial F}{\partial \phi} - \nabla \cdot \frac{\partial F}{\partial \nabla \phi} \right) \tag{3.59}$$

$$= 2\Omega \left(\frac{2\gamma_{\mathrm{s}}}{\epsilon_{\mathrm{pf}}\pi} \left(\frac{\mathrm{d}f(\phi)}{\mathrm{d}\phi} - \epsilon_{\mathrm{pf}}^2 \Delta\phi \right) + \frac{\partial W}{\partial \phi} \right) \tag{3.60}$$

Adopting the flow of the surface (3.50) leads to the phase field flux

$$\mathbf{J}_\phi = -\frac{2D(\phi)}{\epsilon_{\mathrm{pf}}\pi} \left(\nabla\mu_\phi - eZ^* \nabla\phi_{\mathrm{E}} \right) \tag{3.61}$$

and the conservation equation derived from the equation of the normal velocity of the surface

$$\frac{\partial \phi}{\partial t} = -\nabla \cdot \mathbf{J}_{\phi} - \frac{4}{\epsilon_{\mathrm{pf}} \pi} J_{\mathrm{nv}}, \tag{3.62}$$

where the flux from the bulk to the interface J_{nv} as a function of the order parameter has to vanish outside the interface and is expressed by

$$J_{\mathrm{nv}} = \hat{D} f\left(\phi\right)\left(\mu_{\mathrm{bv}} - \mu_{\mathrm{sv}}\right). \tag{3.63}$$

As described above the phase field model is an approximation of the sharp interface model for EM. In Section A it is shown, that for the limit, where the interface controlling parameter ϵ_{pf} goes to zero, the phase field model converges to the sharp interface model [99].

Chapter 4

Numerical Implementation

Finding the analytical solution for partial differential equations in three dimensions is in general only for quite simple problems regarding

- geometries,
- boundary conditions,
- boundaries between domains with different material behavior, and
- material behavior

possible. General TCAD simulations are to complicated and numerical methods have to be used. Numerical methods produce approximations of the solutions. One of the methods mainly used and widespread for Partial Differential Equations (PDEs) in engineering is the Finite Element Method (FEM). Due to the availability of powerful computers since the mid 20th century this method got practicable. Since this method was used for the simulations in this work, the basics will be described in this, followed by a discussion of the implementation of the EM model in the two software packages used.

4.1. Finite Element Method

The finite element method is a common approach to solve PDEs [67]. Thereby the simulation region is filled with a mesh and the solution is approximated by a linear combination of weighted base functions, which is called the *Ritz-Galerkin*-approximation [17]. This approach enables the software to approximate the solution by solving a system of linear equations representable by matrix equations.

A second order PDE can generally be written as

$$\sum_{i,j=1}^{d} \frac{\partial}{\partial x_i} a_{ij}(\mathbf{x}) \frac{\partial u}{\partial x_j} + \sum_{i}^{d} a_i(\mathbf{x}) \frac{\partial u}{\partial x_i} + a(\mathbf{x})u = f(\mathbf{x}), \qquad \mathbf{x} \in \Omega \tag{4.1}$$

for $\Omega \subset \mathbb{R}^d$. Without loss of generality it can be assumed that $a_{ij} = a_{ji}$, which easily can be achieved due to the commutativity of the differentiation order.

Definition 1. *The differential equation 4.1 is elliptic in* $\mathbf{x} \in \Omega$*, iff all eigenvalues of the matrix* (a_{ij}) *have the same sign and are not equal to zero.*

Definition 2. *The differential equation 4.1 is elliptic (in* Ω*), iff it is elliptic in (almost) all* $\mathbf{x} \in \Omega$*.*

For the further description d will be set to three, as the simulations are carried out in the three-dimensional real space and the time derivatives are realized by time stepping to reduce the problem order by solving it iteratively approximated by a finite differences schema. Furthermore, the material parameters in EM are rotationally symmetric leading to the following simplified form of the differential equations, where the symbols ∇ and Δ are used for the nabla and the *Laplace* operator, respectively.

$$\nabla \cdot (\alpha(\mathbf{x})\nabla u(\mathbf{x})) + \boldsymbol{\beta}(\mathbf{x}) \cdot \nabla u(\mathbf{x}) + \gamma(\mathbf{x})u(\mathbf{x}) = b(\mathbf{x}) \qquad \mathbf{x} \in \Omega \tag{4.2}$$

4.1.1. Weak Formulation of PDEs

In order to derive the weak formulation of (4.2) one first has to multiply (4.2) by a test function $\phi(\mathbf{x})$ and then integrate the result over the domain Ω giving [17]

$$\int\limits_{\Omega} \left(\nabla \cdot (\alpha(\mathbf{x})\nabla u(\mathbf{x})) + \boldsymbol{\beta}(\mathbf{x}) \cdot \nabla u(\mathbf{x}) + \gamma(\mathbf{x})u(\mathbf{x}) - b(\mathbf{x})\right)\phi(\mathbf{x})\mathrm{d}V = 0. \tag{4.3}$$

For FEM based simulations only gradients of the solution $u(\mathbf{x})$ and of the test function $\phi(\mathbf{x})$ occur in the integral, allowing the usage of solution functions with lower smoothness. This makes the employment of *Green*'s first identity necessary.

Theorem 1. *Divergence theorem: If* $\mathbf{F}$ *is a vector field and* $\mathbf{n}$ *is an outward pointing normal vector of the surface* $\partial\Omega$ *surrounding the volume* Ω*, then the volume integral of the divergence of* $\mathbf{F}$ *can be converted to the flux integral through the surface by*

$$\int_{\Omega} \nabla \cdot \mathbf{F}\, dV_n = \oint_{\partial\Omega} \mathbf{F} \cdot \mathbf{n}\, dS_{n-1}. \tag{4.4}$$

Applying Theorem 1 to a vector field defined by $\mathbf{F} = \alpha\psi\nabla\phi$ leads to *Green*'s first identity [70].

Theorem 2. Green*'s first identity*

$$\int_{\Omega} (\psi\nabla \cdot (\alpha\nabla\varphi) + \alpha\nabla\varphi \cdot \nabla\psi)\; dV = \oint_{\partial\Omega} \alpha\psi\,(\nabla\varphi \cdot \mathbf{n})\; dS = \oint_{\partial\Omega} \alpha\psi\nabla\varphi \cdot d\mathbf{S} \tag{4.5}$$

Employing Theorem 2 to (4.3) results in the so called weak formulation of the problem, which is given by

$$\begin{aligned}&\oint_{\partial\Omega} \alpha\,(\mathbf{x})\,\phi(\mathbf{x})\nabla u(\mathbf{x}) \cdot d\mathbf{S} + \\ &\int\limits_{\Omega} \left(-\alpha(\mathbf{x})\nabla u(\mathbf{x}) \cdot \nabla\phi(\mathbf{x}) + \boldsymbol{\beta}(\mathbf{x}) \cdot \nabla u(\mathbf{x})\phi(\mathbf{x}) + \gamma(\mathbf{x})u(\mathbf{x})\phi(\mathbf{x}) - b(\mathbf{x})\phi(\mathbf{x})\right)\mathrm{d}V = 0,\end{aligned} \tag{4.6}$$

where the first part is a surface integral and the second integral is carried out over the whole volume. For the further discussion it is assumed that $a(\mathbf{x})$ is a material parameter being piecewise constant and therefore not depending on the position. For example in the drift-diffusion equation of the vacancies it is proportional to the diffusion coefficient (c.f. Section 3.2).

4.1.2. Meshing of the Simulation Domains

Before the actual solving of the PDE can be started, the simulation domain has to be meshed. The meshing procedure subdivides the simulation domain into many small elements, described by nodes, edges, and faces. The generated mesh can either be structured by simple subdivision rules or unstructured for arbitrary domains. Typical shapes used for FEM are triangles (cf. Figure 4.1a) and quadrilaterals (cf. Figure 4.1b) for two-dimensional (2D) domains and tetrahedrons (cf. Figure 4.1c) and hexahedrons (cf. Figure 4.1d) in 3D simulation domains [6]. Figure 4.2 shows an example triangular mesh for an L shaped 2D domain. The mesh is refined at locations of higher interest and smaller geometrical features. In this example this is the fillet, as the boundary is a quarter of a circle.

(a) Triangle (b) Quadrilateral

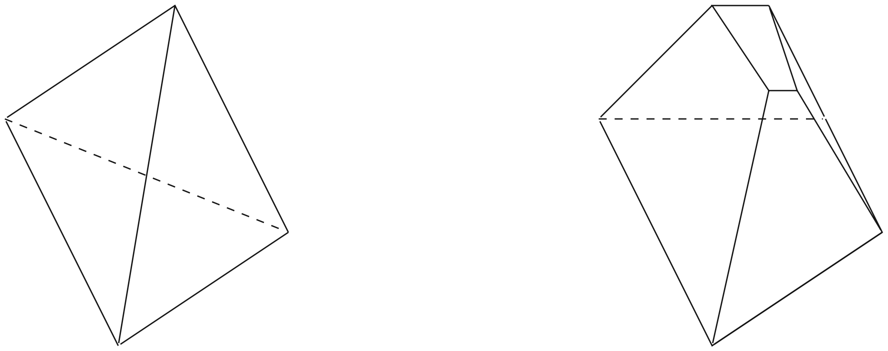

(c) Tetrahedron (d) Hexahedron

Figure 4.1.: Example meshing elements for 2D and 3D domains.

Based on the meshing and its element type a simple reference element can be chosen establishing a mapping. For triangular meshing this mapping is shown in Figure 4.3. Due to this mapping the integration of every element can be formulated as an integration

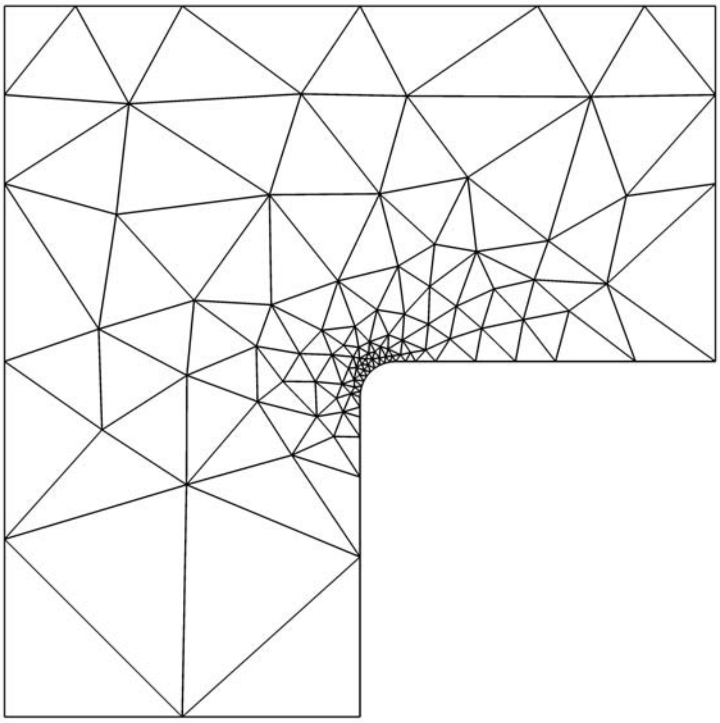

Figure 4.2.: An example mesh for an L shaped structure with a fillet.

over the reference element by employing the determinant $\mathcal{J}\left(\mathbf{x}\left(s,t\right)\right)$ of the *Jacobian* matrix. If the mapping can be written as a linear combination of the vectors spanning the element, where the origin of the element is one of the corner coordinates, the integral melts down to the volume of the original element times an integral not depending on the original element giving the possibility to precompute the integrals of (4.6). For triangular meshing elements (cf. Figure 4.3) the transformation of the integral over an element and the reference element is given by [68]

$$\int\limits_{T} f(\mathbf{x})\mathrm{d}V = \int\limits_{\substack{0\leq s+t\leq 1\\ 0\leq s,t\leq 1}} f(\mathbf{x}(s,t))\mathcal{J}\left(\mathbf{x}\left(s,t\right)\right)\mathrm{d}s\mathrm{d}t = \int\limits_{\substack{0\leq s+t\leq 1\\ 0\leq s,t\leq 1}} f(\mathbf{x}(s,t))\left|\left(\mathbf{x}_1-\mathbf{x}_0,\mathbf{x}_1-\mathbf{x}_0\right)\right|\mathrm{d}s\mathrm{d}t = 2\mathrm{Vol}(T)\int\limits_{\substack{0\leq s+t\leq 1\\ 0\leq s,t\leq 1}} f(\mathbf{x})\mathrm{d}s\mathrm{d}t. \tag{4.7}$$

Important for the transformation is the preservation of the orientation. Choosing for this meshing a test function space V_h and, therefore, a solution space leads to the *Ritz-Galerkin*-approximation [17].

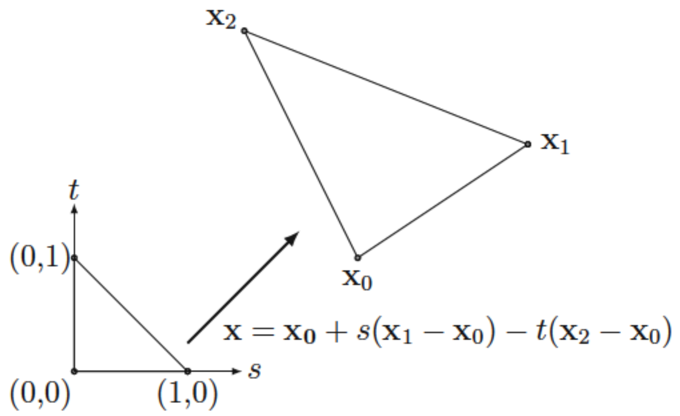

Figure 4.3.: Mapping between an arbitrary triangle and the reference triangle for 2D triangular meshing with the transformation law.

4.1.3. *Ritz-Galerkin*-Approximation

Let V be a (real) *Hilbert* space and $a : V \times V \to \mathbb{R}$ a continuous bilinear form and F a bounded linear functional on V. To solve a problem, given by [17]

$$a\left(u, v\right) = F\left(v\right) \qquad \forall v \in V, \tag{4.8}$$

approximately, the infinite space V is substituted by the finite space $V_h \subset V$. The *Ritz-Galerkin*-Approximation $u_h \in V_h$ is defined as the solution of

$$a\left(u_h, v\right) = F\left(v\right) \qquad \forall v \in V_h. \tag{4.9}$$

This problem is finite-dimensional and with $\{\phi_1, ..., \phi_N\}$ being a complete basis of V_h the solution can be written by the linear combination

$$u_h = \sum_{i=1}^{N} u_{h,i} \phi_i. \tag{4.10}$$

(4.9) has to be valid for all $v \in V_h$ and to solve the problem it is enough to use only the basis functions ϕ_i transforming the problem to

$$a\left(u_h, \phi_i\right) = F\left(\phi_i\right), \qquad i = 1, ..., N \tag{4.11}$$

and by substituting u_h by (4.10) a system of N linear equations

$$\sum_{j=1}^{N} a\left(\phi_j, \phi_i\right) u_{h,j} = F\left(\phi_i\right), \qquad i = 1, ..., N \tag{4.12}$$

with N unknowns is obtained. By defining the matrix $\mathbf{A} = (A_{ij}) = (a(\phi_j, \phi_i))$ and the vectors $\mathbf{b} = (b_i) = (F(\phi_i))$ and $\mathbf{u} = (u_j)$ the system can be written in matrix notation

$$\mathbf{A}\mathbf{u} = \mathbf{b} \tag{4.13}$$

and reduces the implementation to the calculation of the solution of a system of linear equations.

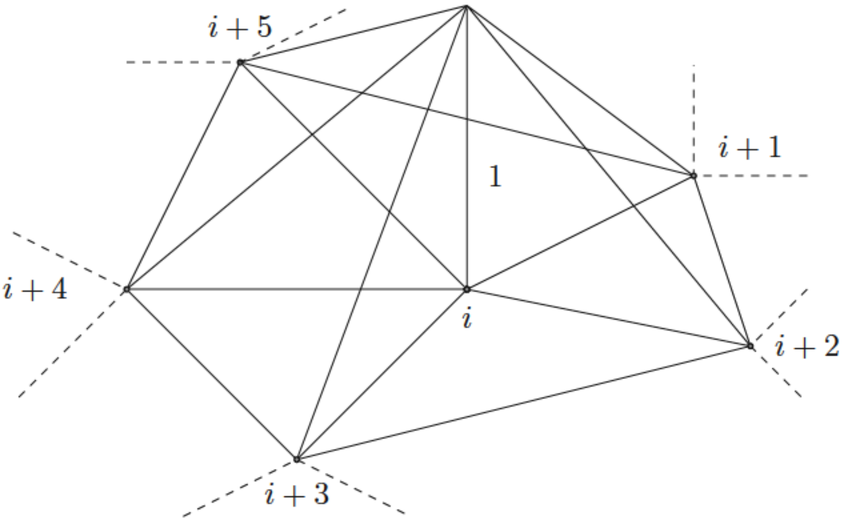

Figure 4.4.: The hat test function for a single node located in the middle.

A typical test function used for the weak formulation (4.6) is the so called hat function shown in Figure 4.4 [6]. It is defined to be 1 at the meshing point considered and decreases linearly in direction of the neighboring meshing points to zero. For a single triangle the function is defined by

$$f(\mathbf{x}) = \frac{\left|(\mathbf{x}_j - \mathbf{x}) - \left((\mathbf{x}_j - \mathbf{x}) \cdot \frac{\mathbf{x}_j - \mathbf{x}_k}{|\mathbf{x}_j - \mathbf{x}_k|}\right) \frac{\mathbf{x}_j - \mathbf{x}_k}{|\mathbf{x}_j - \mathbf{x}_k|}\right|}{\left|(\mathbf{x}_j - \mathbf{x}_i) - \left((\mathbf{x}_j - \mathbf{x}_i) \cdot \frac{\mathbf{x}_j - \mathbf{x}_k}{|\mathbf{x}_j - \mathbf{x}_k|}\right) \frac{\mathbf{x}_j - \mathbf{x}_k}{|\mathbf{x}_j - \mathbf{x}_k|}\right|}. \tag{4.14}$$

For the reference triangle the coordinates of the points are given by

$$\mathbf{x}_i = (0,0)^T \tag{4.15}$$

$$\mathbf{x}_j = (0,1)^T \tag{4.16}$$

$$\mathbf{x}_k = (1,0)^T \tag{4.17}$$

$$\tag{4.18}$$

and a general coordinate by

$$\mathbf{x} = (s,t)^T \tag{4.19}$$

resulting in the hat function

$$f_{i,(s,t)}(\mathbf{x}) = 1 - s - t. \tag{4.20}$$

The same procedure can be applied to the other two meshing points of this triangle leading to the functions

$$f_{j,(s,t)}\left(\mathbf{x}\right) = s \tag{4.21}$$

and

$$f_{k,(s,t)}\left(\mathbf{x}\right) = t. \tag{4.22}$$

The weak formulation (4.6) can now be transformed in a summation of integrals over each of the N triangles T_l, leading to

$$\begin{gathered}\sum_{l=1}^{N} \oint\limits_{\partial T_l \cap \partial \Omega} \alpha\phi(\mathbf{x})\nabla u(\mathbf{x}) \cdot d\mathbf{S}+ \\ \sum_{l=1}^{N} \int\limits_{T_l} \left(-\alpha \nabla u(\mathbf{x}) \cdot \nabla\phi(\mathbf{x}) + \boldsymbol{\beta}(\mathbf{x}) \cdot \nabla u(\mathbf{x})\phi(\mathbf{x}) + \gamma(\mathbf{x})u(\mathbf{x})\phi(\mathbf{x}) - b(\mathbf{x})\phi(\mathbf{x})\right) \mathrm{d}V = 0\end{gathered} \tag{4.23}$$

and by applying the approximation of all functions as a linear combination of the hat functions given by

$$g(\mathbf{x}) = \sum_{i=1}^{M} g_i f_i(\mathbf{x}) \tag{4.24}$$

for M mesh points it follows

$$\begin{aligned}&\sum_{i=1}^{M}\sum_{j=1}^{M} u_j\phi_i \sum_{l=1}^{N} \Bigg(\oint\limits_{\partial T_l \cap \partial \Omega} \alpha f_i(\mathbf{x}) \nabla f_j(\mathbf{x}) \cdot d\mathbf{S}- \\ &\qquad \alpha \int\limits_{T_l} \nabla f_j(\mathbf{x}) \cdot \nabla f_i(\mathbf{x}) \mathrm{d}V + \sum_{k=1}^{M} \boldsymbol{\beta}_k \int\limits_{T_l} f_k(\mathbf{x}) \cdot \nabla f_j(\mathbf{x}) f_i(\mathbf{x}) \mathrm{d}V+ \\ &\qquad \sum_{k=1}^{M} \gamma_k \int\limits_{T_l} f_k(\mathbf{x}) f_j(\mathbf{x}) f_i(\mathbf{x}) \mathrm{d}V \Bigg) - \sum_{k=1}^{M}\sum_{l=1}^{N} b_k \int\limits_{T_l} f_k(\mathbf{x}) f_i(\mathbf{x}) \mathrm{d}V = 0.\end{aligned} \tag{4.25}$$

As this result has to be valid for every function ϕ it is enough to choose only one hat function at a time.

$$\begin{aligned}&\sum_{j=1}^{M} u_j \Bigg(\sum_{l=1}^{N} 2\mathrm{Vol}(T_l) \Bigg(\oint\limits_{\partial T_l \cap \partial \Omega} \alpha f_i(\mathbf{x}) \nabla f_j(\mathbf{x}) \cdot d\mathbf{S}'- \\ &\qquad \alpha \int\limits_{T_l} \nabla f_j(\mathbf{x}) \cdot \nabla f_i(\mathbf{x}) \mathrm{d}V' + \boldsymbol{\beta}_k \int\limits_{T_l} f_k(\mathbf{x}) \cdot \nabla f_j(\mathbf{x}) f_i(\mathbf{x}) \mathrm{d}V'+ \\ &\qquad \gamma_k \int\limits_{T_l} f_k(\mathbf{x}) f_j(\mathbf{x}) f_i(\mathbf{x}) \mathrm{d}V' \Bigg)\Bigg) = \sum_{l=1}^{N} b_k \int\limits_{T_l} f_k(\mathbf{x}) f_i(\mathbf{x}) \mathrm{d}V' \quad \forall i \in \{1, \cdots, M\}\end{aligned} \tag{4.26}$$

The primed coordinate system is the coordinate system of the reference system and allows the calculation of every integral in advance. This leads to the matrix representation

$$\mathbf{A}(\boldsymbol{\beta},\boldsymbol{\gamma})\mathbf{u} = \mathbf{C}\mathbf{b}. \tag{4.27}$$

The elements of matrix $\mathbf{A}$ are defined by

$$\begin{aligned} A_{ij} = \sum_{l=1}^{N} 2\mathrm{Vol}(T_l)\Bigg(& \oint\limits_{\partial T_l \cap \partial\Omega} \alpha f_i(\mathbf{x})\nabla f_j(\mathbf{x}) \cdot d\mathbf{S}' - \alpha \int\limits_{T_l} \nabla f_j(\mathbf{x}) \cdot \nabla f_i(\mathbf{x})\mathrm{d}V' + \\ & \boldsymbol{\beta}_k \int\limits_{T_l} f_k(\mathbf{x}) \cdot \nabla f_j(\mathbf{x}) f_i(\mathbf{x})\mathrm{d}V' + \gamma_k \int\limits_{T_l} f_k(\mathbf{x}) f_j(\mathbf{x}) f_i(\mathbf{x})\mathrm{d}V' \Bigg) \end{aligned} \tag{4.28}$$

and of matrix $\mathbf{C}$ by

$$C_{ik} = \sum_{l=1}^{N} b_k \int\limits_{T_l} f_k(\mathbf{x}) f_i(\mathbf{x})\mathrm{d}V' \tag{4.29}$$

and b_k, u_j, and γ_k is represented by the vectors $\mathbf{b}$, $\mathbf{u}$, and $\boldsymbol{\gamma}$, respectively. The $\boldsymbol{\beta}_k$ are joined into the matrix $\boldsymbol{\beta}'$. These are sparse matrices as only those integrals in (4.26), where the i, j and k are edges of the triangle that is integrated over are not zero.

4.2. Implementation in FEDOS

FEDOS (Finite Element Diffusion and Oxidation Simulator) is a general FEM simulation software developed at the Institute for Microelectronics [60]. It is capable to handle every PDE of first order in time and arbitrary differential order in space. Furthermore, it can handle coupled PDE [62]. The generation of the geometry and the meshing are preformed by external programs. As output FEDOS can write a solution file for every time step or only for the end of the simulation. FEDOS output can be used for the presentation and interpretation in external programs (e.g. visualization tools) as well as a list of maximal and minimal values for every time step. The capability of outputting the maximum and minimum values makes it a very useful tool for EM simulations, as the maximum tensile stress in the structure is a key parameter for cracking and void formation.

4.2.1. Implementation of Models in FEDOS

To set up a new model in FEDOS a model file is written, where the assembly rules for the matrix $\mathbf{A}$ and $\mathbf{C}$ of (4.27) are specified. Due to the element-wise assembly this definition is used for each triangle giving its nodes as input and returning the values which have to be passed into the matrices. Models can be implemented for domains, for boundaries between domains or for boundaries of the simulation domain, realizing thereby boundary conditions.

4.2.2. Simulation Stepping

After starting the simulation, FEDOS solves the modeled problems sequentially. Figure 4.5 depicts the sequence of an EM simulation in a flow chart. First the electro-thermal problem is solved and the values needed for the vacancy dynamics are passed to the next simulation phase. There the vacancy dynamics is simulated, followed by a stress calculation in the solid mechanics simulation step. After all these steps are performed the accuracy of the solution is checked. If a given precision of the solution result is reached, the solution is accepted and the maximum stress is compared against a threshold for the void formation or for cracking. If the error threshold of the solution is exceeded, the time step size is reduced by multiplying it with a user chosen factor (smaller 1) and the simulation of the last time step is reperformed. The time step size gets multiplied by the inverse of the same factor, if the solution of the following time steps are in a given error range.

4.3. Implementation in COMSOL

COMSOL [30] is a commercial program widely used in industry and research for the simulation of FEM based problems. It offers a complete solution for various physics and engineering applications starting from the geometry generation over the modeling to the simulation and evaluation with various plotting tools and data exporting capabilities. In addition it offers a material data base from where material parameters can be imported.

4.3.1. Electro-Mechanical Model

The electro-mechanical model is a preconfigured model including the electric potential

$$\mathbf{E} = -\nabla V \tag{4.30}$$

$$\mathbf{J} = \left(\sigma + \epsilon_0\epsilon_\mathrm{r}\frac{\partial}{\partial t}\right)\mathbf{E} + \mathbf{J}_\mathrm{e} \tag{4.31}$$

$$\nabla\cdot\mathbf{J} = Q_\mathrm{e}, \tag{4.32}$$

where V stands for the electric potential, $\mathbf{J}$ for the current density, $\mathbf{J}_\mathrm{e}$ for a user predefined current density, Q_e for the free charge distribution and σ for the conductivity. The *Joule* heating modeling is formulated by the equation system

$$Q = \mathbf{E}\cdot\mathbf{J} \tag{4.33}$$

$$\rho C_\mathrm{p}\frac{\partial T}{\partial t} + \rho C_\mathrm{p}\mathbf{u}\cdot\nabla T = \nabla\cdot(k\nabla T) + Q, \tag{4.34}$$

where Q stand for the thermal energy dissipated per time, C_p for the thermal expansion coefficient under constant pressure, ρ for the volumetric mass density, k for the thermal conductivity, and $\mathbf{u}$ for the velocity field. The mechanical stress modeling is implemented

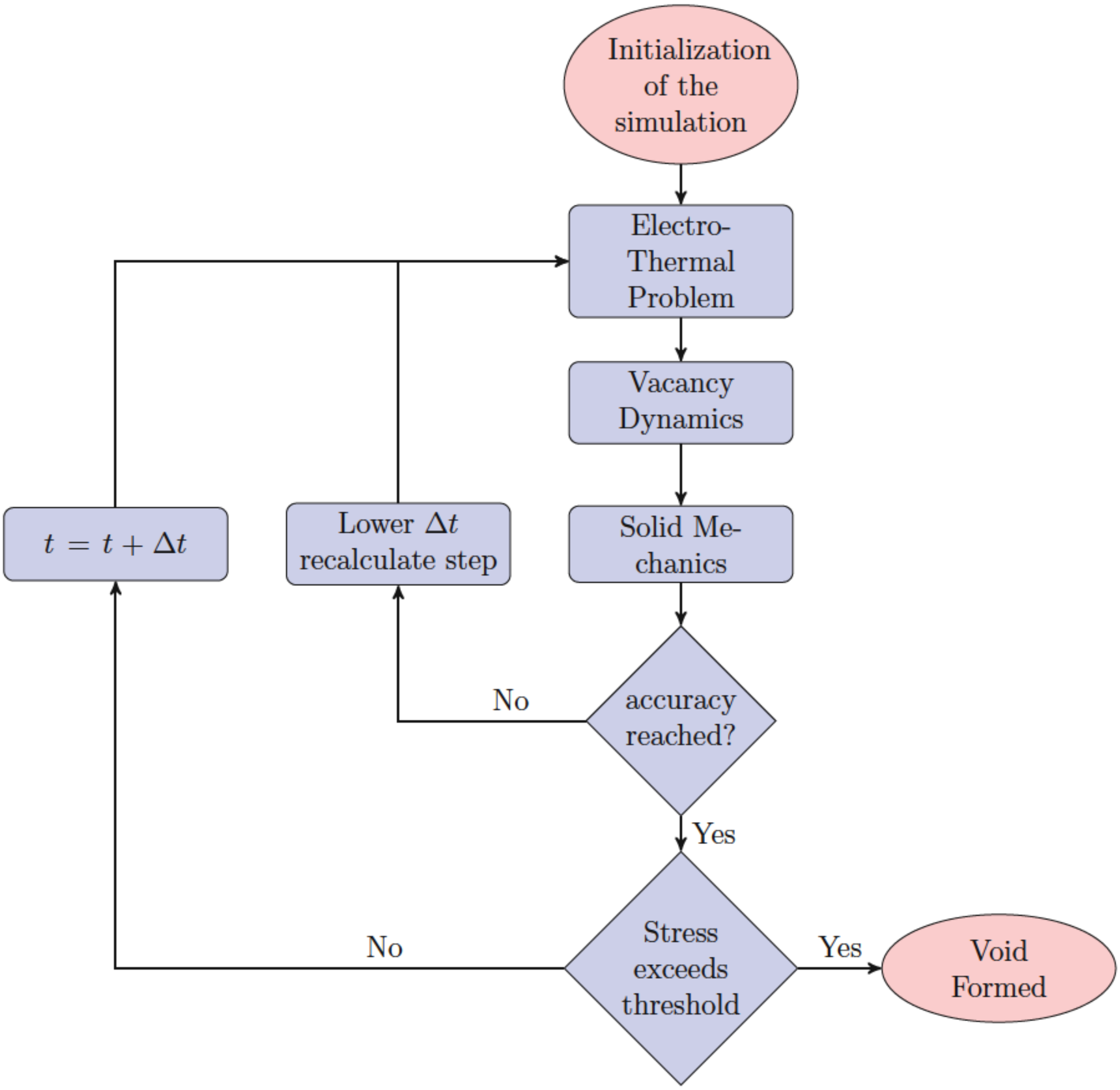

Figure 4.5.: Flowchart of the EM simulation in FEDOS.

for small deformations by

$$-\nabla \cdot \boldsymbol{\sigma} = \mathbf{F}_{\text{v}} \tag{4.35}$$

$$\boldsymbol{\sigma} - \boldsymbol{\sigma}_0 = C : (\boldsymbol{\epsilon} - \boldsymbol{\epsilon}_0 - \boldsymbol{\epsilon}_{\text{inel}}) \tag{4.36}$$

$$\boldsymbol{\epsilon}_{\text{inel}} = \alpha \left(T - T_{\text{ref}}\right) \mathbf{1} \tag{4.37}$$

$$\boldsymbol{\epsilon} = \frac{1}{2} \left((\nabla \mathbf{u})^T + \nabla \mathbf{u} \right) . \tag{4.38}$$

where $\mathbf{F}_{\text{V}}$ stands for the body force density, T_{ref} for the reference temperature of the thermal expansion, and $\boldsymbol{\epsilon}_{\text{inel}}$ for the strain originating from the thermal expansion. This model has the ability to include strains by $\boldsymbol{\epsilon}_0$ or stresses by $\boldsymbol{\sigma}_0$ from another model and is used to includes the strain arising from the vacancy flux and vacancy generation/annihilation in the EM model.

4.3.2. PDE as Electromigration Model

Since not for all physical problems models are included in COMSOL, it provides the "Coefficient Form PDE", which allows to express a huge set of technical relevant linear and non-linear PDEs. This general PDE has the following form:

$$e_a \frac{\partial^2 u}{\partial t^2} + d_a \frac{\partial u}{\partial t} - \nabla \cdot (c \nabla u + \boldsymbol{\alpha} u - \boldsymbol{\gamma}) + \boldsymbol{\beta} \cdot \nabla u + a u = f \tag{4.39}$$

EM is represented by two differential equations, one for the vacancy flux and one for the strain due to the movement of the vacancies as well as their generation/annihilation. The vacancy dynamics is modeled by a conservation law with a generation/annihilation term given by (3.9). By comparing this equation against (4.39) it follows that e_a, $\boldsymbol{\gamma}$ and $\boldsymbol{\beta}$ have to be set to zero and d_a has to be set to one. Taking this into account and rearranging the equation leads to

$$\frac{\partial u}{\partial t} = \nabla \cdot (c \nabla u + \boldsymbol{\alpha} u) + (f - a u)\,. \tag{4.40}$$

The equation parameters have to be set as follows to model vacancy dynamics.

$$c = -D_\mathrm{v} \tag{4.41}$$

$$\boldsymbol{\alpha} = D_\mathrm{v} \left(\frac{|Z^*| e}{k_\mathrm{B} T} \mathbf{E} - \frac{f \Omega}{k_\mathrm{B} T} \nabla \sigma + \frac{Q^*}{k_\mathrm{B} T^2} \nabla T \right) \tag{4.42}$$

$$f = \frac{C_\mathrm{eq}}{\tau_\mathrm{v,eq}} \tag{4.43}$$

$$a = \frac{1}{\tau_\mathrm{eq}} \tag{4.44}$$

The electric field $\mathbf{E}$ and the hydraulic pressure σ are taken from the electro-mechanical model (cf. Section 4.3.1).

For the strain build-up by the vacancy dynamics and generation/annihilation the same general equation (4.39) can be used with the parameters set as following:

$$c = -\Omega \,(1 - f) \tag{4.45}$$

$$\boldsymbol{\alpha} = \Omega \,(1 - f) \left(\frac{|Z^*| e}{k_\mathrm{B} T} \mathbf{E} - \frac{f \Omega}{k_\mathrm{B} T} \nabla \sigma + \frac{Q^*}{k_\mathrm{B} T^2} \nabla T \right) \tag{4.46}$$

$$f = \Omega f \frac{C_\mathrm{eq}}{\tau_\mathrm{v,eq}} \tag{4.47}$$

$$a = \Omega f \frac{1}{\tau_\mathrm{eq}} \tag{4.48}$$

Since also the strain build-up is described by a first derivative in time analogously the parameters e_a, $\boldsymbol{\gamma}$, and $\boldsymbol{\beta}$ are set to zero and d_a to one. It should be emphasized that the vacancy dynamics model is connected through the stress gradient to the solid mechanics model, which by itself depends on the strain build-up by the vacancies as an input value making those models highly nonlinear.

4.3.3. Phase Field Model

In COMSOL a phase field model is implemented by the equation

$$\frac{\partial \phi}{\partial t} + \mathbf{u} \cdot \nabla \phi = \nabla \cdot \frac{\gamma \lambda}{\epsilon_{\mathrm{pf}}^2} \nabla \psi \left(\phi \right), \tag{4.49}$$

where $\mathbf{u}$ is a velocity field. Taking into account that the velocity field is divergence free ($\nabla \cdot \mathbf{u} = 0$) this equation can be rearranged to

$$\frac{\partial \phi}{\partial t} = \nabla \cdot \left(-\mathbf{u}\phi + \frac{\gamma \lambda}{\epsilon_{\mathrm{pf}}^2} \nabla \psi \left(\psi \right) \right). \tag{4.50}$$

Independent of the form of the function $\psi\left(\phi\right)$, this equation has the form of a conservation.

$$\frac{\partial \phi}{\partial t} = \nabla \cdot \mathbf{J} \tag{4.51}$$

Therefore, the phase field model of COMSOL is not suitable to implement the vacancy exchange between the bulk and the interface of the void evolution model, described in Section 3.6, represented by the last term of

$$\frac{\partial \phi}{\partial t} = \frac{2}{\epsilon_{pf}\pi} \nabla \cdot \mathcal{D}_s(\phi) \left(\nabla \mu_s - eZ\mathbf{E} \right) - \frac{4A}{\epsilon_{pf}\pi} (\mu_s - \mu_v). \tag{4.52}$$

Therefore, for the implementation of the phase field model the “Coefficient Form PDE” (4.39) has to be chosen with the parameters set as follows:

$$e_a = 0, \tag{4.53}$$

$$\boldsymbol{\gamma} = \frac{2}{\epsilon_{pf}\pi} \mathcal{D}_s(\phi) \left(\nabla \mu_s - eZ\mathbf{E} \right), \tag{4.54}$$

$$\boldsymbol{\beta} = \mathbf{0}, \tag{4.55}$$

$$c = 0, \tag{4.56}$$

$$\boldsymbol{\alpha} = \mathbf{0}, \tag{4.57}$$

$$f = -\frac{4A}{\epsilon_{pf}\pi} (\mu_s - \mu_v), \tag{4.58}$$

$$a = 0. \tag{4.59}$$

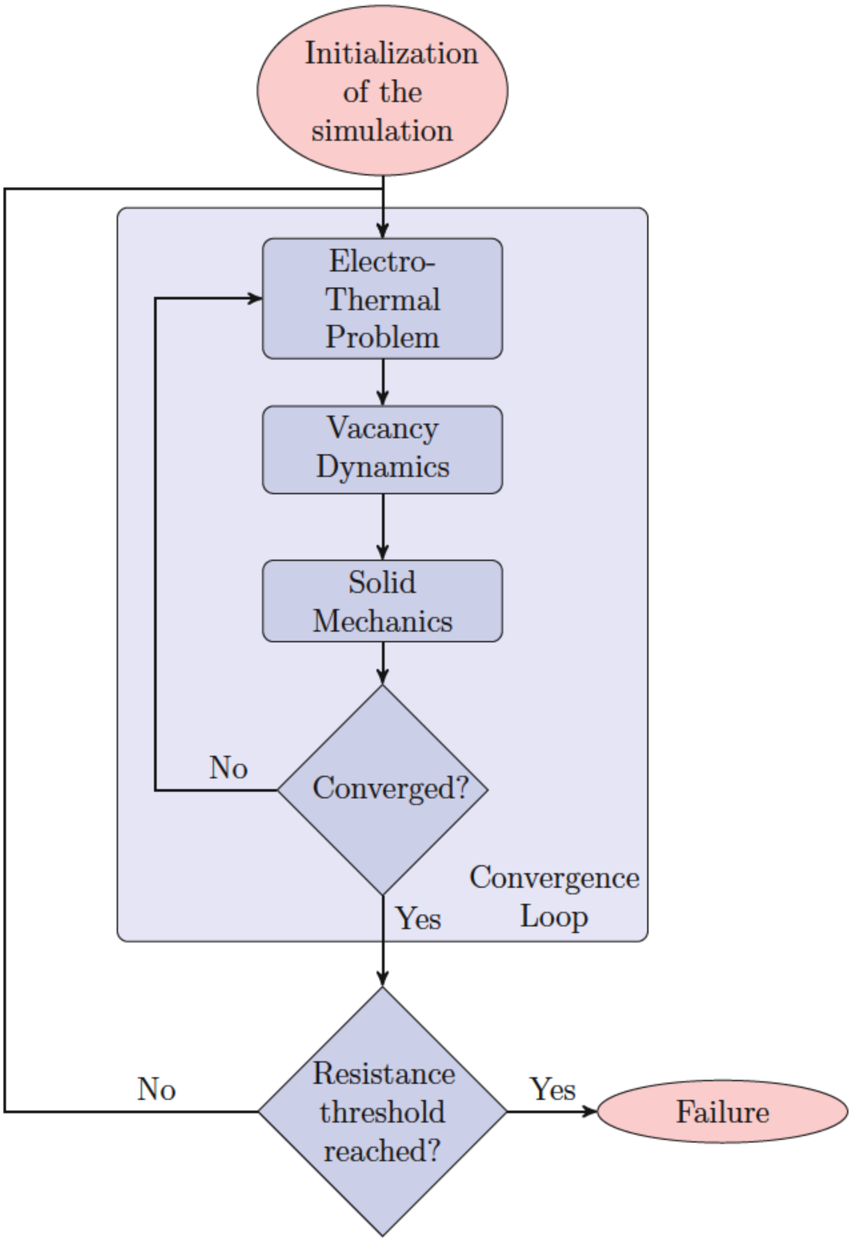

Figure 4.6.: Flowchart of the EM simulation in COMSOL.

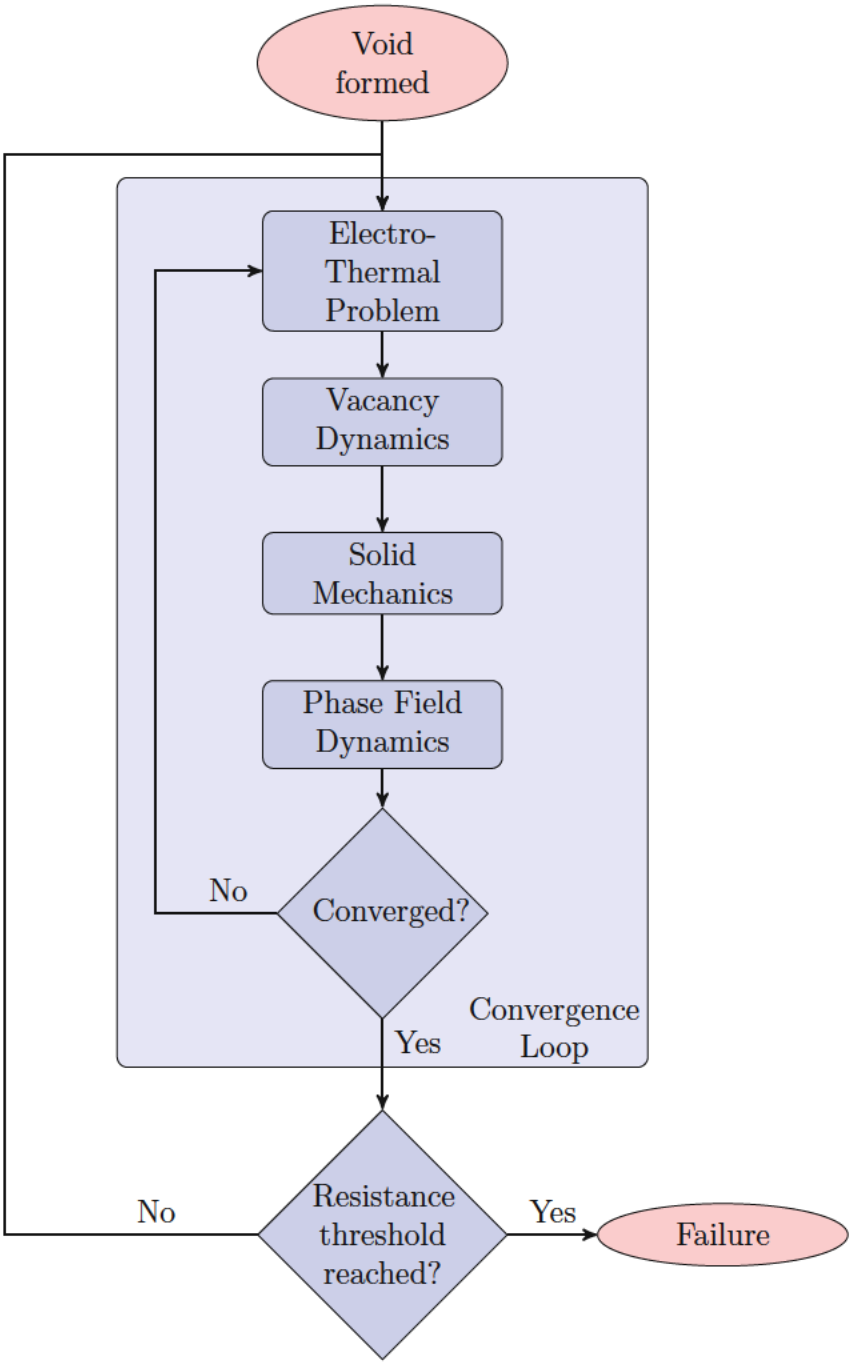

Figure 4.7.: Flowchart of the EM induced void simulation in COMSOL.

4.3.4. Time Stepping

COMSOL offers two methods to compute the solution. The first method called “Fully Coupled” generates the matrices **A** and **C** of (4.27) where all differential equations are included at once. These matrices depend on the solution vector (e.g. the coupling of the vacancy flux and the stress equations) and therefore, first (4.27) is solved where $\boldsymbol{\beta}$ and $\boldsymbol{\gamma}$ is retrieved from the old solution vectors. This step is followed by a regeneration of the matricies using $\boldsymbol{\beta}$ and $\boldsymbol{\gamma}$ calculated from the new solution vector and solving again. These steps are repeated untill convergence is reached. The simulation is terminated under user chosen conditions (e.g. maximum step number), if the problem does not converge. After the solution has converged, the next time step is computed. The time step size depends on various conditions (e.g. step size to the next chosen output time).

The second method called “Segregated Step” generates the matrices **A** and **C** in (4.27) for every system separately and calculates the solutions sequentially. The number and the included differential equations of the systems can by chosen by the user. For EM without void modeling the sequence is depicted in Figure 4.6 and for EM modeling with void modeling in Figure 4.7. This method is the method of choice as the “Fully Coupled” method often needs too much memory, since the size of the matrices grows with second order of the number of mesh points.

Chapter 5

Results and Discussion

The reliability of interconnects in ICs is a key issue for the overall quality of electronic systems. In this section the assessment of a structure called open TSV is presented. Open TSVs are 3D structures made out of different materials, which exhibit corners and interfaces. These regions suffer from current crowding which breaks the homogeneity of the current density. Thereby, the available cross section is not optimally used. Furthermore, the interfaces between the different conducting layers show a behavior which promotes the EM induced effects. Therefore, current crowding is of major interest and analyzed in detail. This is followed by a full EM study of this structure regarding the most prominent locations, where EM leads to a failure. This failure is examined for two different modes. The first mode is the so called early mode, where a crack leads to an open circuit and an immediate failure. In the second so called late failure mode not a crack but a void is formed. This does not lead to an instant failure, but initializes a phase where the void grows and evolves. This evolution leads to a failure as soon as the void has grown big enough to block a significant part of the current conducting cross section, leading to an open circuit or a resistance increase over a critical value. These results are fitted to the generalized *Black* equation which is a widely used compact model for EM [12].

5.1. Current Crowding

Current crowding is the effect of peaks in the current density due to locations of nonhomogeneous material parameters (e.g. lower resistance regions) or areas of elevated electrical field strength. These effects lead in metals to areas with raised *Joule* heating, which influence the material parameters and their behavior (e.g. *Kirkendall* effect [51]). Therefore, these areas are particularly studied for open TSV structures with respect to the geometry and the resistance of the conducting materials.

Corners are typical regions where current crowding occurs. *Sabelka* [115] gave an analytic solution for a corner with an arbitrary angle α shown in Figure 5.1. For this geom-

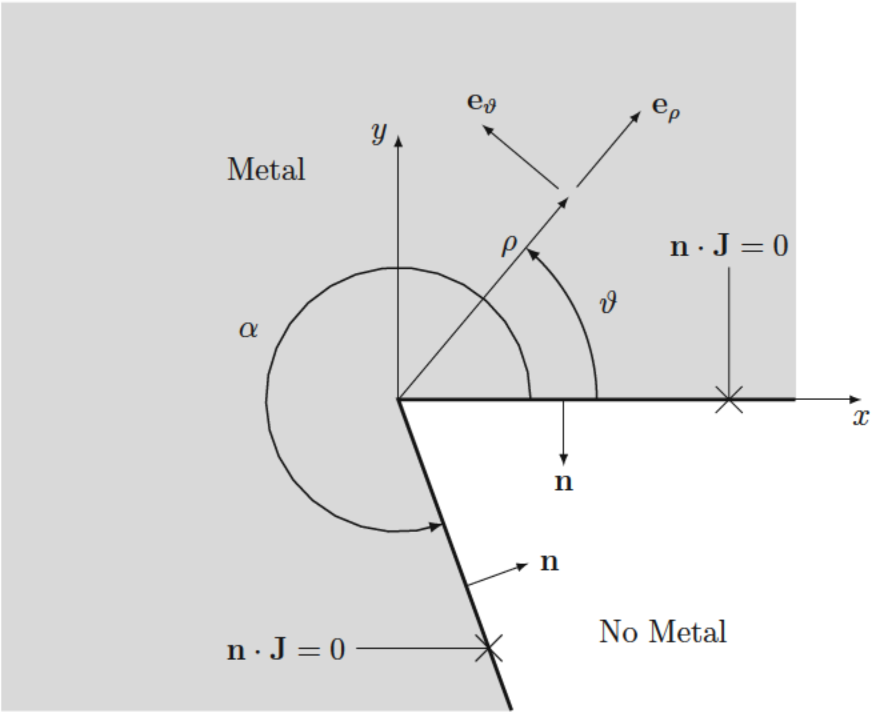

Figure 5.1.: Schematics of the current crowding calculation at a corner.

etry the *Poisson* equation can be written in polar coordinates for two dimensions [150].

$$\Delta\phi(\rho,\vartheta) = \frac{\partial^2\phi(\rho,\vartheta)}{\partial\rho^2} + \frac{1}{\rho}\frac{\partial\phi(\rho,\vartheta)}{\partial\rho} + \frac{1}{\rho^2}\frac{\partial^2\phi(\rho,\vartheta)}{\partial\vartheta^2} = 0 \tag{5.1}$$

This equation can be transformed into

$$\rho^2\frac{\partial^2\phi(\rho,\vartheta)}{\partial\rho^2} + \rho\frac{\partial\phi(\rho,\vartheta)}{\partial\rho} + \frac{\partial^2\phi(\rho,\vartheta)}{\partial\vartheta^2} = 0, \tag{5.2}$$

which allows the use of the ansatz

$$\phi(\rho,\vartheta) = P(\rho)\,\Theta(\vartheta), \tag{5.3}$$

leading to two separate equations depending only on one of the independent variables ρ and ϑ

$$a = -\frac{\Theta''(\vartheta)}{\Theta(\vartheta)} \quad \text{and} \tag{5.4}$$

$$a = \rho^2\frac{P''(\rho)}{P(\rho)} + \rho\frac{P'(\rho)}{P(\rho)}. \tag{5.5}$$

The solution for the first differential equation is given by

$$\Theta(\vartheta) = C_1\sin\left(\vartheta\sqrt{a}\right) + C_2\cos\left(\vartheta\sqrt{a}\right), \tag{5.6}$$

where the application of the boundary conditions, no normal flux at the metal edges (cf. Figure 5.1),

$$\mathbf{e}_\vartheta \cdot \left(-\frac{\mathbf{J}}{\sigma_\mathrm{E}}\right) = \mathbf{e}_\vartheta \cdot \nabla\phi = \mathbf{e}_\vartheta \cdot \left(\frac{\partial\phi}{\partial\rho}\mathbf{e}_\rho + \frac{1}{\rho}\frac{\partial\phi}{\partial\vartheta}\mathbf{e}_\vartheta\right) = \frac{1}{\rho}\frac{\partial\phi}{\partial\vartheta} = 0 \tag{5.7}$$

for the angles $\vartheta = 0°$ and $\vartheta = \alpha$ only allows solutions of the form

$$\Theta\left(\vartheta\right) = C_{1,n}\cos\left(\vartheta\frac{n\pi}{\alpha}\right) \qquad \forall n \in \mathbb{N}_0. \tag{5.8}$$

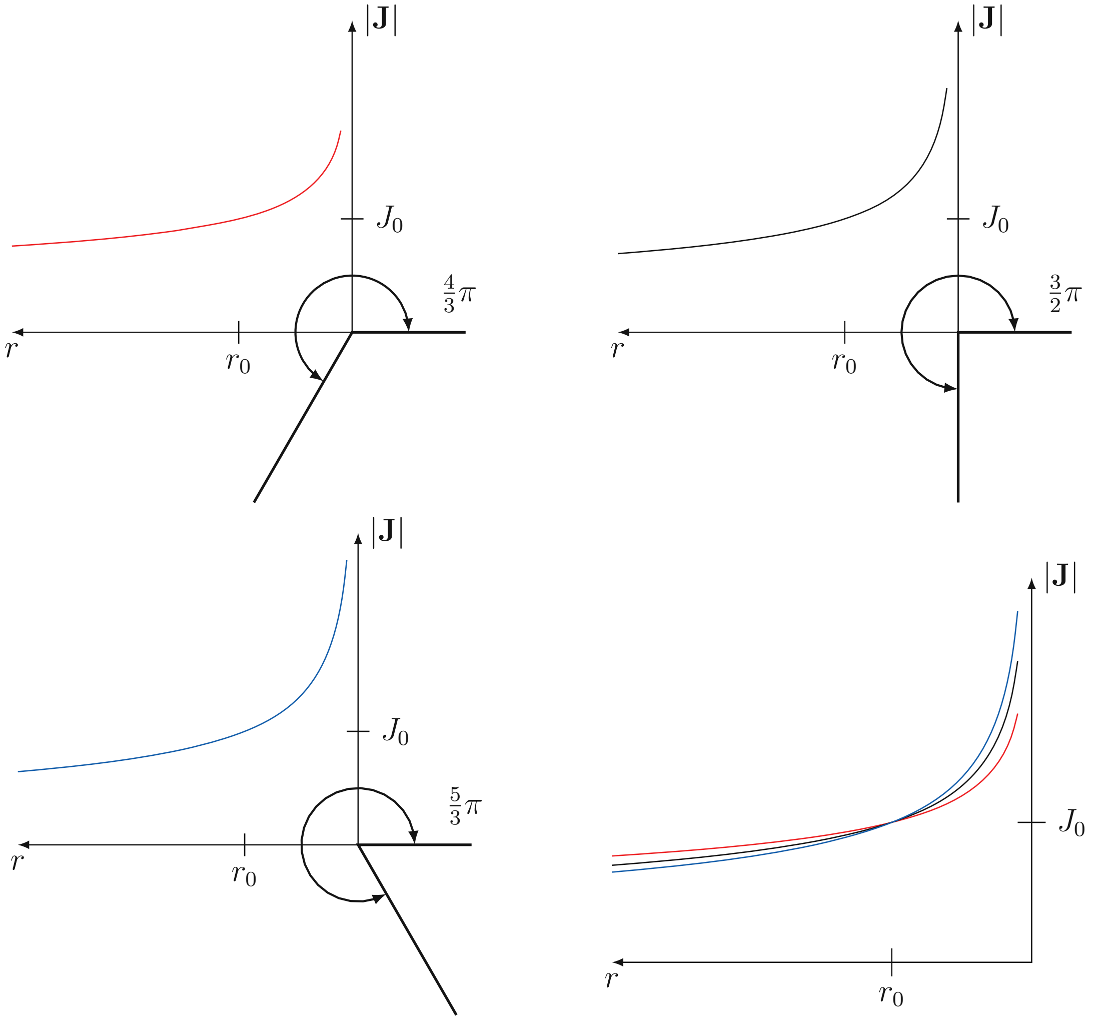

Figure 5.2.: The current density at corners for different angles versus the radial distance. The current densities are normalized to J_0 at the radius r_0. The lower the angle of the corner, the higher the current density rises in the vicinity of the corner. In the last plot the three curves are put together to facilitate comparison.

For the second equation with $\sqrt{a} = \frac{n\pi}{\alpha}$ the solution has the form

$$P(\rho) = D_{1,n}\rho^{\frac{n\pi}{\alpha}} + D_{2,n}\rho^{-\frac{n\pi}{\alpha}}, \tag{5.9}$$

where only the first term has a physical meaning as the second has a singularity at the origin. Putting (5.8) and (5.9) together results in

$$\phi(\rho, \vartheta) = C_n r^{\frac{n\pi}{\alpha}} \cos\left(\vartheta \frac{n\pi}{\alpha}\right), \tag{5.10}$$

with $C_n = C_{1,n}D_{1,n}$ and the gradient for positive non-zero n is given by

$$\begin{aligned}\left(-\frac{\mathbf{J}}{\sigma_{\mathrm{E}}}\right) = \nabla\phi &= \frac{\partial\phi}{\partial\rho}\mathbf{e}_\rho + \frac{1}{\rho}\frac{\partial\phi}{\partial\vartheta}\mathbf{e}_\vartheta \\ &= C_n\frac{n\pi}{\alpha}\rho^{-1+\frac{n\pi}{\alpha}}\cos\left(\vartheta\frac{n\pi}{\alpha}\right)\mathbf{e}_\rho - C_n\frac{n\pi}{\alpha}\rho^{-1+\frac{n\pi}{\alpha}}\sin\left(\vartheta\frac{n\pi}{\alpha}\right)\mathbf{e}_\vartheta. \end{aligned}\tag{5.11}$$

The gained solutions can show a singularity at the origin, where the exponent of ρ gets negative. This is true for those sections where n meets the condition

$$0 < n < \frac{\alpha}{\pi}, \tag{5.12}$$

which is only possible, when α is between π and two times π and n equals one. The norm of the current density for $n = 1$ is given by

$$|\mathbf{J}| = C_1\sigma\frac{\pi}{\alpha}\rho^{-1+\frac{\pi}{\alpha}}. \tag{5.13}$$

Figure 5.2 shows the radial dependence of the current density for different angles. As the exponent of the equation points out, corners with higher angles show higher current densities in the vicinity of the corner, which is called current crowding.

In conventional vias and TSVs the whole vertically connecting structure is filled by the conducting metal. At present there are two kinds of material systems in use. The first one is the copper system, where the vertical and the horizontal connections are made out of copper, and the second is the aluminium tungsten system, where the horizontal or planar connections are made out of aluminium and the vertically connecting structures are made out of tungsten. For the later configuration, Figure 5.3 shows the current density at the interface of the planar interconnect and the via for different ratios of the via height and the via width. For higher ratios the current density at the interface between the horizontal interconnect and the vertical structure has a higher variation than for lower ratios. The highest current densities are found at the edges of the structures, where the right corner values are significantly higher compared to the left ones. In Figure 5.3a the current at the right corner is 3.5 times larger compared to the left corner.

The open TSV [83] is constructed as a hollow cylinder consisting of a tungsten coating, where at the top an aluminium cylinder is placed, overlapping the tungsten from the inside. Figure 5.4 depicts the structure, where the aluminium is shown in yellow, the

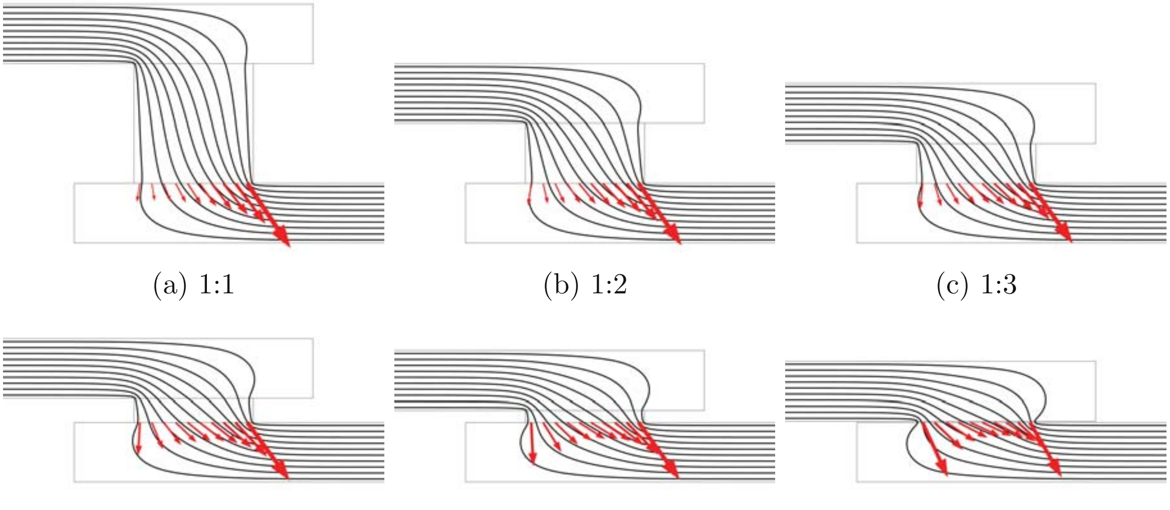
(a) 1:1 (b) 1:2 (c) 1:3

(d) 1:5 (e) 1:10 (f) 1:100

Figure 5.3.: The current density is presented by the red arrows at the interface between the planar connecting structure and the via, for different ratios of the via width and the via height. The lines represent the electric flow lines.

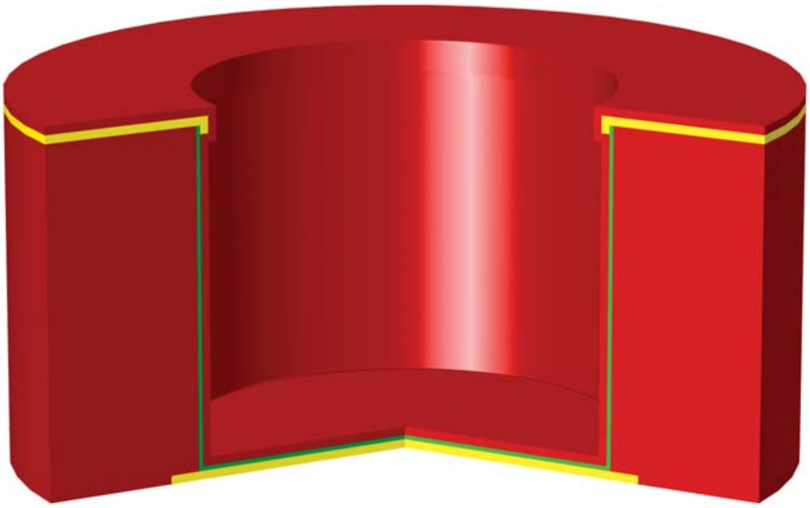

Figure 5.4.: Profile view of the TSV structure: Aluminium in yellow, tungsten in green, and substrate and seal layer in red. The tungsten cylinder is shortened to 10% of the real length.

tungsten in green, and the surrounding isolation layers and the silicon substrate in red. Cutting out the segment of interest results in the piece shown in Figure 5.5, where the curvature of the cylinder is neglected. This is a permissible assumption as the ratio of the layer thicknesses and the radius of the whole open TSV is in the order of 1 to 100. Therefore, this structure was chosen for the simulations of the current crowding behavior at the aluminium/tungsten interface. Furthermore, the corner at the top of the TSV was not taken into account, as the results are only slightly changed by it.

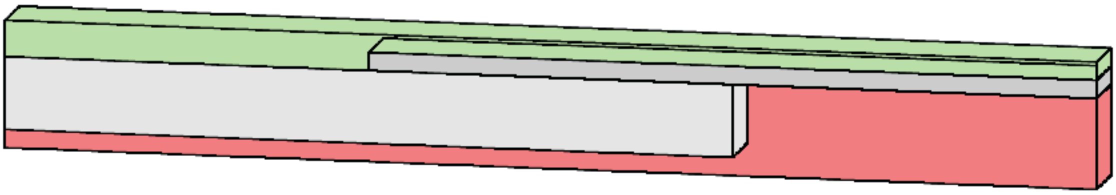

Figure 5.5.: The structure of a segment of the overlapping area of the tungsten cylinder and the aluminium cylinder. Green represents titanium nitride, red silicon oxide, dark gray tungsten, and light gray aluminium.

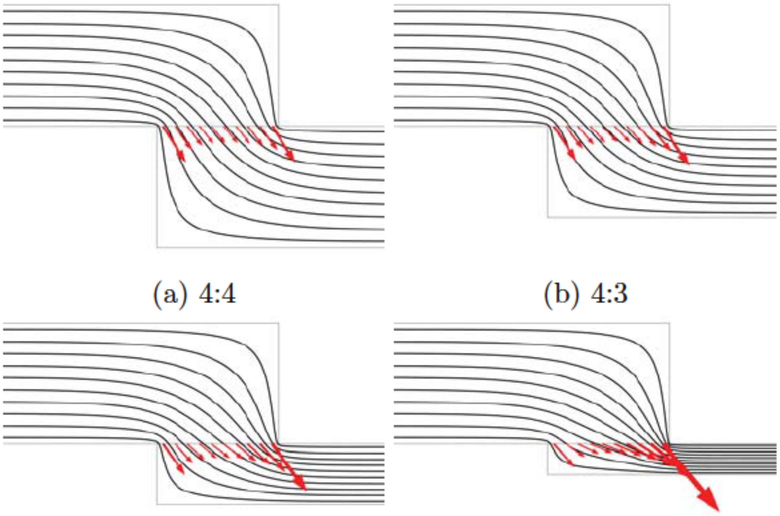

(a) 4:4

(b) 4:3

(c) 4:2

(d) 4:1

Figure 5.6.: The current density is shown by the red arrows at the interface between the aluminium layer on the top and the tungsten layer at the bottom for different ratios of the thicknesses of the two layers. The lines represent the electric flow lines.

The open TSV structure has a tungsten layer with a different thickness than the aluminium layer. Figure 5.6 shows the current densities, where the thickness of the aluminium layer on the top is kept constant and the thickness of the tungsten layer at the bottom is varied. There the assumption of equal conductivities is chosen to particularly see the impact of different thicknesses. In Figure 5.6 it can be seen that the current crowding takes place on both edges in the same range for a ratio of 1, as the red current density arrows are equal at both edges (cf. Figure 5.6). The smaller the thickness of the tungsten, the more current is transferred at the right corner, whereas the current crowding at the left corner gets smaller. In the studied TSV structure the ratio is in the range of 4, which is the reason that the higher current crowding takes place at the right corner.

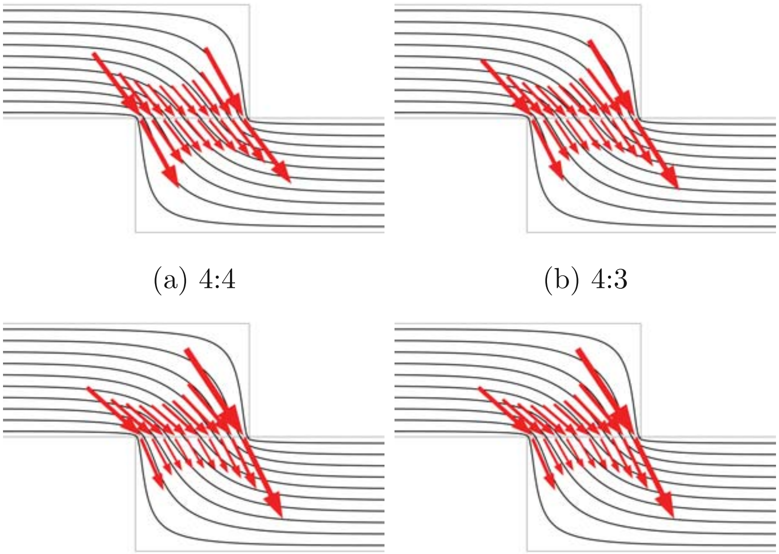

(a) 4:4

(b) 4:3

(c) 4:2

(d) 4:1

Figure 5.7.: The current density is shown by the red arrows at the interface between the planar connecting structure and the via for different ratios of the resistances of the upper and the lower layer. The lines represent the electric flow lines.

In the simulations for different thicknesses the assumption of equal conductivity was chosen. This is in the case of tungsten and aluminium not true as tungsten has approximately half the conductivity of aluminium. In Figure 5.7 the conductivity of the aluminium is varied in multiples of the conductivity of tungsten with both layers having the same thickness to examine only the influence of resistance differences. The black lines are the current streamlines and the red arrows show the current density close to the interface. The upper ones show the current density in the aluminium and the lower ones show the same in the tungsten. The higher the ratio, the more deviation is present in the current densities between the materials. Furthermore, the current crowding is shifted to the right corner, the higher the ratio gets. Therefore, the current transfer between the two metals mainly occurs at the right side of the interface due to its special geometry on one hand and the difference in conductivities on the other hand, which leads to the high current crowding depicted in Figure 5.8.

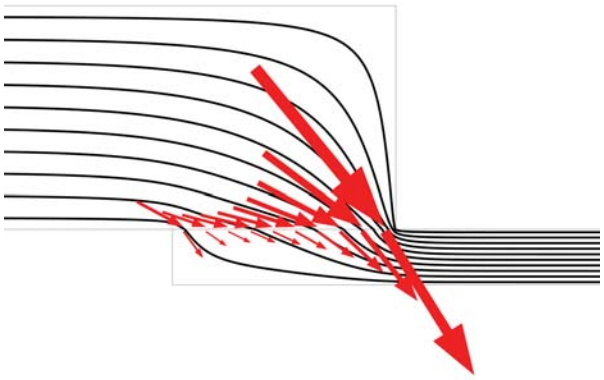

Figure 5.8.: The current density is shown by the red arrows at the interface between the planar connecting structure and the via. The lines represent the electric flow lines and show that the transfer of current between the two metals is mainly occurring closed to the right interface end.

The current densities at the ends of the interface show a saturation in relation to the interface length. For short interfaces the transfer of current between the two metals takes place over the whole interface length, whereas for an interface length over a characteristic length l_0 the middle part of the interface carries only current densities parallel to the interface and therefore, does not contribute to the current transfer between the metals. The characteristic length l_0 is in the range of six times the layer thickness. In Figure 5.9 the current density component normal to the interface is depicted, showing this behavior in the middle of the interface.

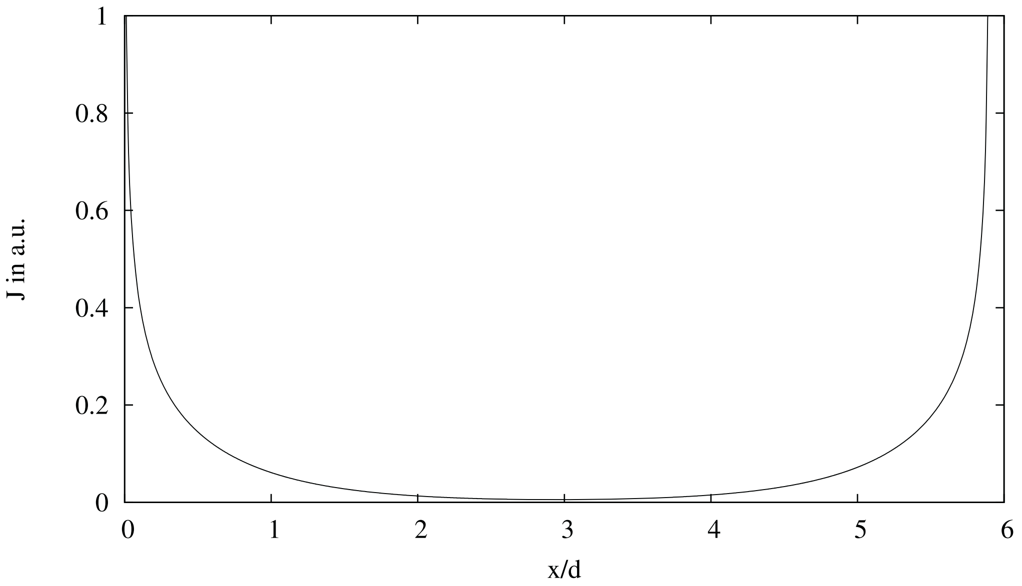

Figure 5.9.: Component of the current density vector normal to the interface.

5.2. Interface Vacancy Pile-Up

This study deals with the question of how different interface structures change the vacancy concentrations at the interface. Interfaces can limit the flux of vacancies, according to the segregation model (c.f. Section 3.3.3), as well as they can act as high diffusive paths for the vacancies along them [34]. For the tungsten/aluminium interface the interface behavior was studied for different parameters to get an idea, which results have to be expected for the structure shown in Figure 5.5.

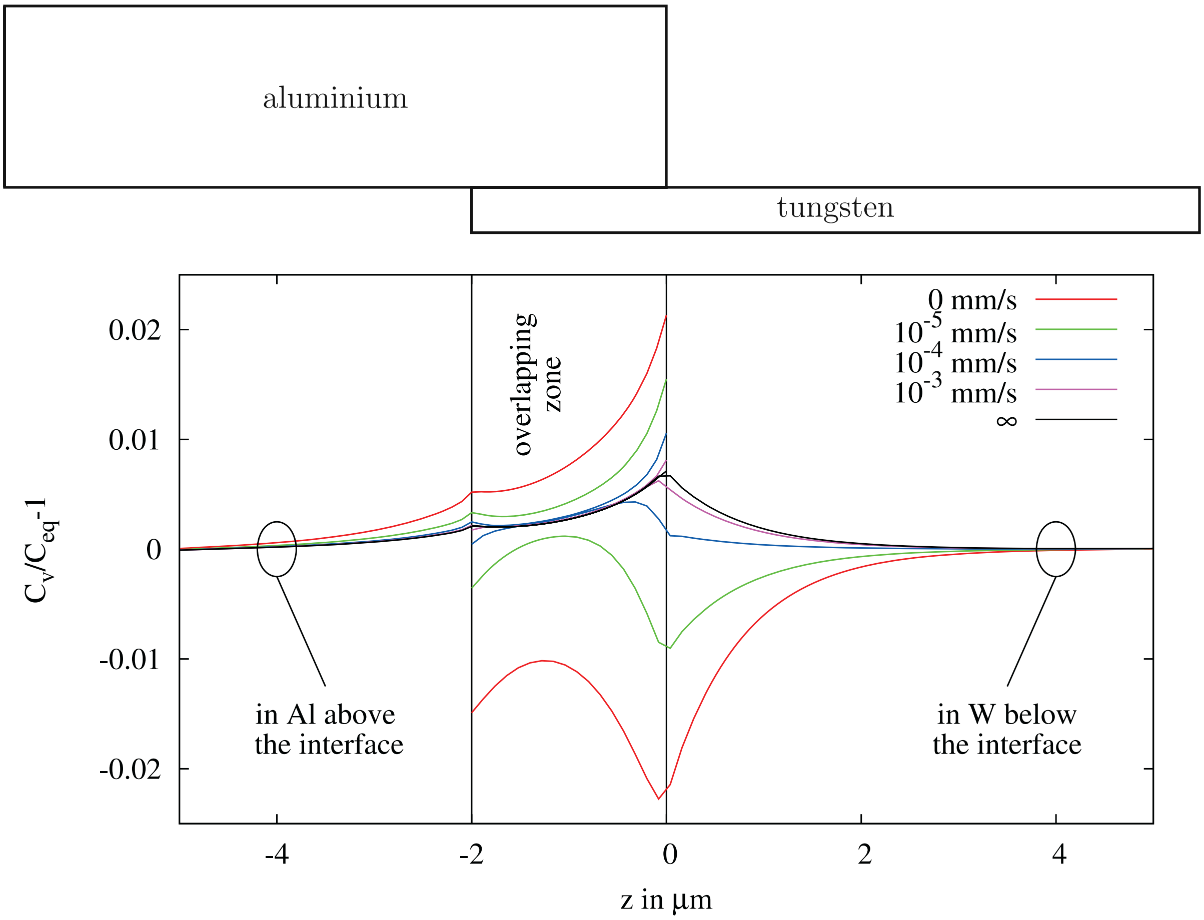

Figure 5.10.: Segregation model: Variation of the transport coefficient h. Vacancy concentration in aluminium and in tungsten versus the location of the interface.

Figure 5.10 shows the vacancy concentration close to the interface in the aluminium represented by the upper curves and the tungsten by the lower curves for different interface conductivities normalized by the equilibrium concentration. Due to the partial blocking of the interface, vacancies are piled up in the aluminium layer close to the interface, whereas in the tungsten layer the vacancies close to the interface flow away and cannot be recovered. Therefore, the concentration in this region is lower compared to the

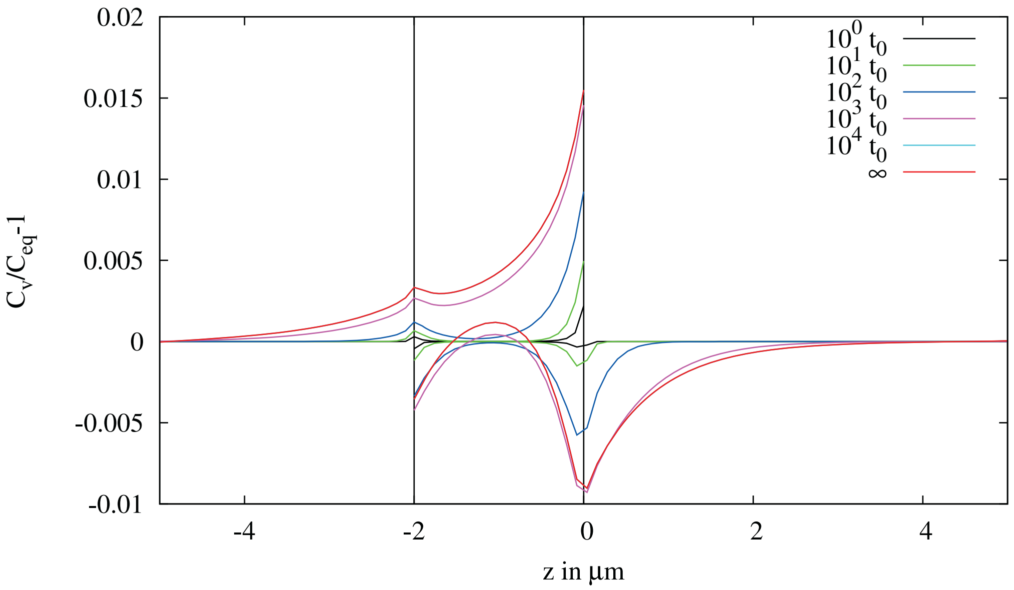

Figure 5.11.: Simulation of a highly blocking interface ($h = 10^{-5}$ mm/s) for different time steps in arbitrary t_0 units.

equilibrium concentration. The highest deviations from the equilibrium concentrations are found at the edges of the interface. There, as shown in Section 5.1, the highest perpendicular component of the current density is found. This component of the current density is responsible for the delivery of vacancies to the interface in the aluminium and for the transport of vacancies away from the interface in the tungsten region. This phenomenon gets stronger the more the interface exhibits a blocking behavior. As explained in the segregation model (cf. Section 3.3.3) the interface can be understood as the infinitely thin limit of a region with a diffusion coefficient low against the other materials. Seen form this point, the interface has a high divergence due to the deviation of the diffusion coefficient which explains the observed results. Farther away from the interface the concentration converges back to the equilibrium.

Figure 5.11 shows the development of the vacancy pile-up in time for a chosen highly blocking value. At the corners the deviation increases fast compared to the middle region. After some time the concentration in the tungsten starts to increase in the middle region in contrast to the edge areas. This is caused by the vacancies that at first diffuse form the edge area in the aluminium to the middle part of the aluminium interface region and then are transported back through the interface into the tungsten, as they experience there a lower EM induced driving force. It should be remarked that also for an interface without segregation a deviation from the equilibrium concentration can be observed, due to current crowding at the edges. However, this effect is of equal strength in both layers.

A second phenomenon which can occur at interfaces between materials is a higher vacancy equilibrium concentration in the *Rosenberg-Ohring* term (c.f. Section 5.7). Figure 5.12 depicts the results of simulations, where the equilibrium concentration of the interface is varied. The black line represents the result for a simulation where the interface behaves exactly like the metal layers. The increase of the concentration is driven by the in-homogeneous current, which again has the highest impact at the interface edges due to current crowding. For lower interface equilibrium concentrations the results decrease as the interface annihilates vacancies. Here, current crowding at

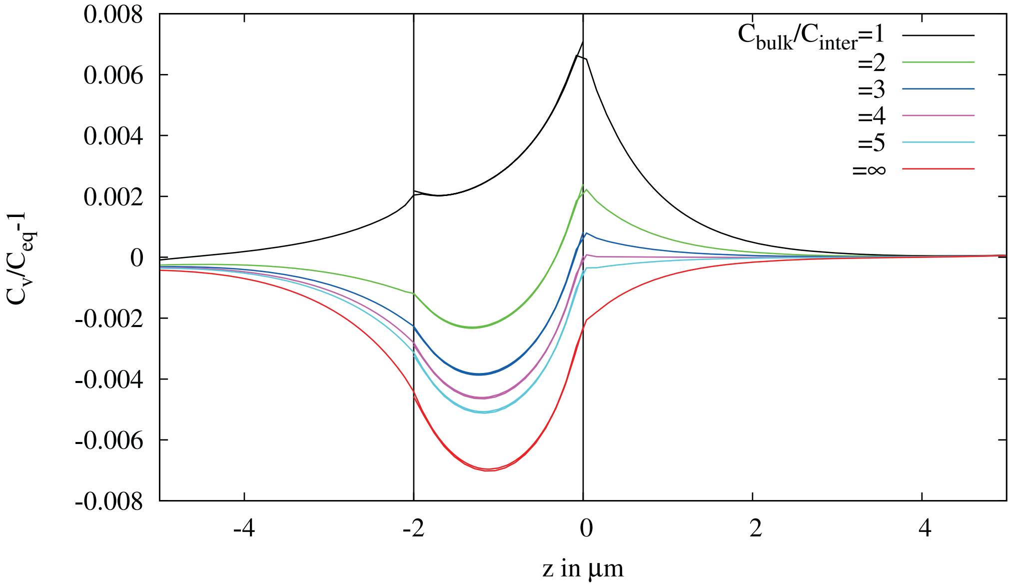

Figure 5.12.: Variation of the equilibrium concentration in the interface region.

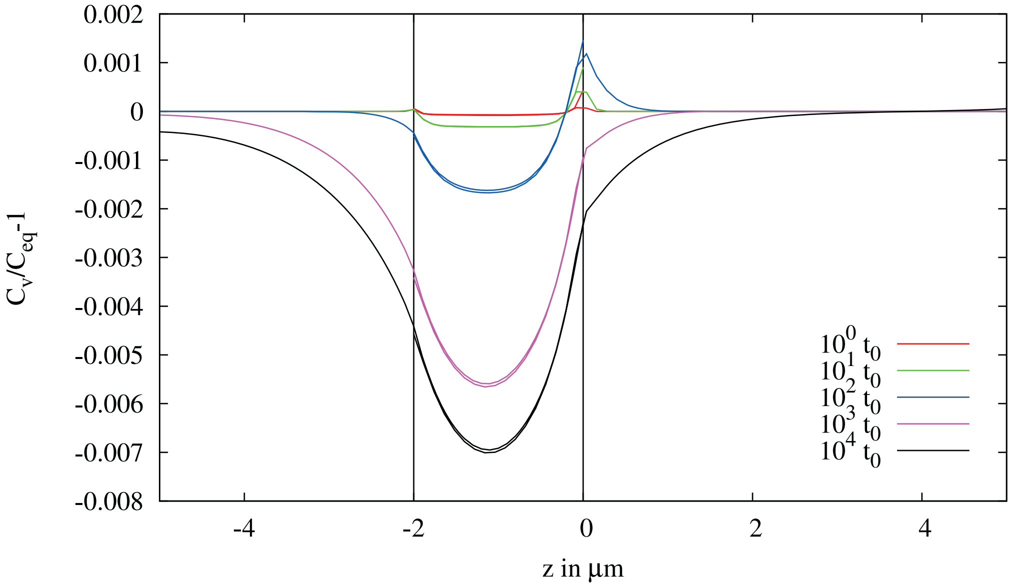

Figure 5.13.: Rosenberg-Ohring model: Results at different time steps for the lowest possible equilibrium concentration ($C_{inter} = 0$).

the edges floods the interface region with vacancies and, therefore, to some degree the impact of the vacancy annihilation is compensated. Figure 5.13 shows the evolution in time for the lowest possible equilibrium concentration of the interface of $C_{\mathrm{inter}} = 0$. For short periods the EM induced vacancy transport at the left corner overwhelms the process of annihilation, as can be seen by the slightly positive vacancy concentration. Whereas after longer time periods the behavior flips into an annihilation dominated one.

The results show that the worst case behavior is the total blocking interface, as there the pile-up of vacancies in the aluminium layer and the depletion in the tungsten layer lead to the highest deviation from the equilibrium concentration. Furthermore, for the annihilation behavior there are two extremes observable. For equilibrium concentrations the vacancy concentrations at the corners increase relative to the outer regions, whereas for highly annihilating interfaces the concentrations of the vacancies decrease compared to the outer regions. Therefore, for the aluminium layer in addition to the segregation behavior, the non-annihilating interface is the worst case. In contrast, for the tungsten layer the highly annihilating interface is the worst case. As the diffusion constant of the tungsten is much lower compared to the aluminium, for the following simulation the blocking interface with non-annihilation character is admissible.

5.3. The Three Phases of the Electromigration Induced Vacancy Accumulation

The time development of the maximum vacancy concentration for the test structure introduced in Figure 5.5 is shown in Figure 5.14. As can be readily seen, the development of the maximum vacancy concentration can be divided into three phases [75]. In the first phase extending from the beginning of the simulation till approximately one second the vacancies show a linear dependence in time. The curvature is introduced due to the logarithmic scale of the time axis. In this period the flux is only driven by the EM induced driving force. This phase is followed by the second phase with a constant maximum vacancy concentration. In this phase the EM induced flow is compensated by the flows due to concentration and stress gradients on the one hand side and on the other hand side by the generation and annihilation modeled with the *Rosenberg-Ohring* term. Generation/annihilation leads to an increase in stress (build-up) in the structure. After approximately 10^4s the maximum vacancy concentration rises rapidly. This is the beginning of the third phase.

Figure 5.15 shows the development of the stress in the structure. In the first phase of the vacancy pile-up the stress increases linearly in time as the inelastic strain is only sustained by the shift of vacancies in the structure. After a short time the concentration of vacancies has reached a certain threshold value and the back flow due to the other flux phenomena reduces the stress growth rate leading to a sub-linear stress development. In the third phase the stress level has obtained a value where cracking or void nucleation is expected and, therefore, these phenomena have to be taken into account. This is the point, where a soft failure has to be expected.

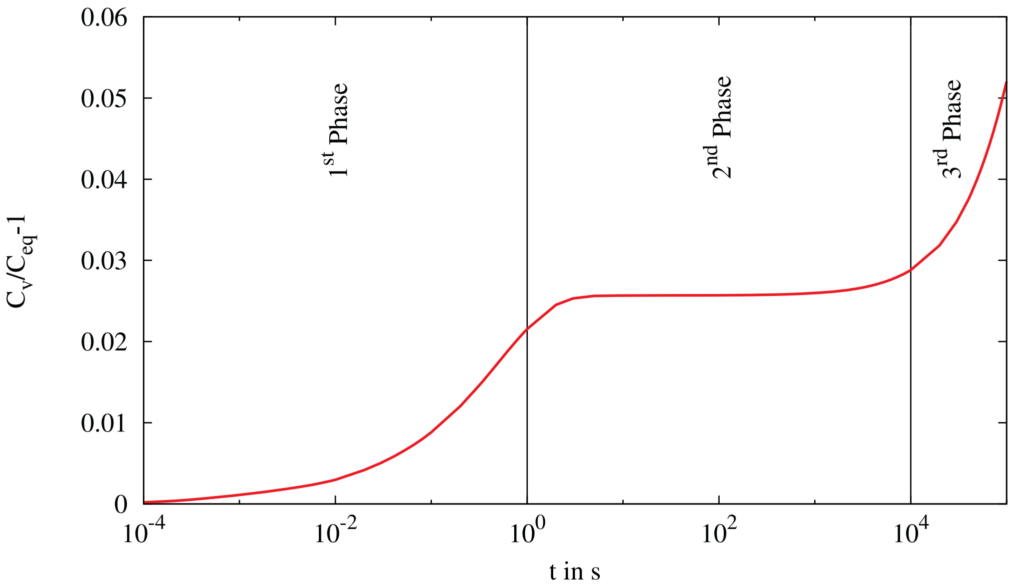

Figure 5.14.: The maximum concentration of vacancies piled up at the interface.

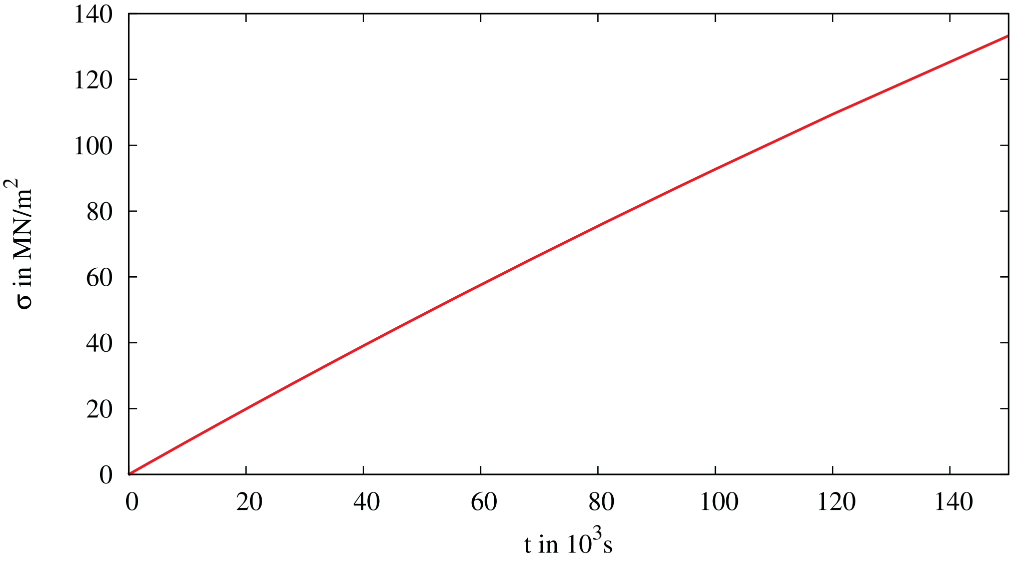

Figure 5.15.: Maximum *Von Mises* stress build-up at the interface.

5.4. Electromigration Induced Stress at the Interfaces of Open TSVs

As described in Section 1.5 the open TSV technology is based on a hollow cylinder of overlapping conducting metal layers reaching from one side of the die to the other (cf. Figure 5.4). For FEM based simulation these arrangements with metal layer thick-

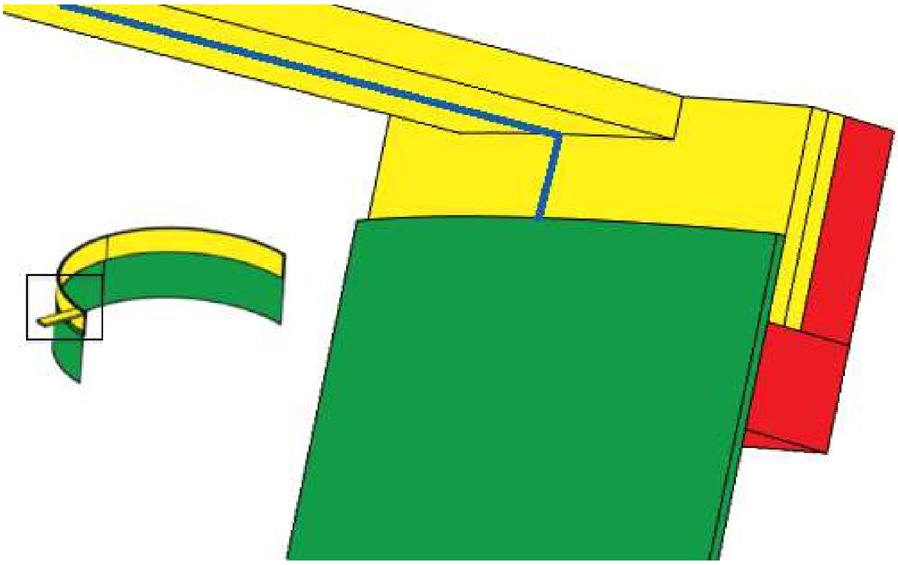

Figure 5.16.: Segment of the TSV closest to the current introducing planar interconnect line. The inset shows the half of the upper open TSV structures aluminium cylinder at the top and tungsten cylinder at the bottom. The blue line indicates the cross section for which the following simulation results are plotted. In this zone the highest current densities are foreseen and therefore EM has the biggest influence.

nesses in the order of tenth of a micrometer and the TSV diameter in the range of hundreds of micrometers make the meshing for 3D computations close to impossible. Therefore, a representative small segment of the open TSV has to be chosen in order to carry out simulations. This segment is located centrally under the planar interconnection which connects the open TSV with the integrated circuit, as shown in Figure 5.16. There the aspect ratio of the layer thicknesses and the overall structure is in the range of one to hundred, leading to an acceptable meshing quality inside the metal layers. Furthermore, as the results of Section 5.2 show, that a blocking interface has the highest impact on the vacancy pile-up and the high resistance of tungsten against EM, due to its low diffusion coefficient compared to aluminium, the vacancy flux calculations were restricted to the aluminium based structures.

Figure 5.17 shows the appearance of the current crowding effect, as described in Section 5.1. This current crowding influences especially the vacancy pile-up for short times, as the highest vacancy concentration in the structure is found at the corner for a simulated time period in the range of one second shown in Figure 5.18a. In the phase of quasi-equilibrium, where the maximum vacancy concentration stays constant, the vacancies pile-up in the whole structure due to the concentration gradient and stress gradient induced fluxes till the third phase starts. The vacancy concentration in this second phase is depicted in Figure 5.18b and shows that the vacancies are not transported to the interface but accumulated already before. In the third picture (Figure 5.18c) the vacancy concentration has very high values at the tungsten/aluminium interface, but also

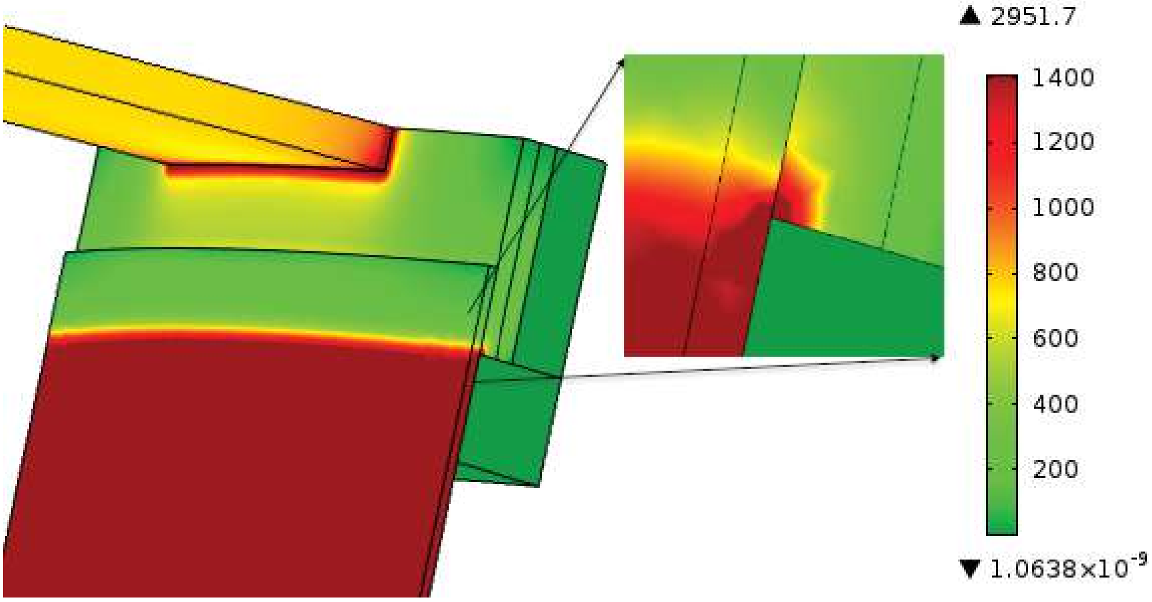

Figure 5.17.: Current density in $10^3\mathrm{A/cm^2}$ in the simulated segment of the open TSV. At the bottom of the aluminium cylinder the current crowding is pronounced.

at the silicon oxide/aluminium interfaces. This behavior will get clear by considering the *Von Mises* stress distribution inside the open TSV shown in Figure 5.19.

For short times the stress is mainly driven by the shift of vacancies. Therefore, the highest stress, as shown in Figure 5.19a, is located in those areas where the highest vacancy concentrations are found (c.f. Figure 5.18a) with a linear dependence between them. As soon as phase two starts the stress increases over time and spreads out into the areas further away from the interface shown in Figure 5.19b according to the behavior described in Section 5.3. The vacancy concentration stays constant at the interface and the concentration in the rest of the aluminium rises asymptotically to the one of the interface. After this second phase the stress reaches a value where the vacancy concentration diverges. Due to the tendency of the aluminium to shrink, while the surrounding material tends to stay in size, a high stress is built up at the interfaces (cf. Figure 5.19c) leading in the real structure to cracking or the formation of voids. At this point the simulation can be interrupted as a so called soft failure has been reached [35].

The development of the maximum *Von Mises* stress in the structure versus time is shown in Figure 5.20. By choosing a stress threshold for cracking or void formation according to Section 3.5 for every current density a TTF can be found and fitted to *Black*'s equation. In Figure 5.21 the data points for a threshold *Von Mises* stress of $200\mathrm{MN/m^2}$ are shown. Furthermore, the graph of a fit to *Black*'s equation is shown. Due to the chosen logarithmic scale of the axis the fitted graph is represented by a straight line. The fitted exponent of the current density in (2.6) was found to be 0.74.

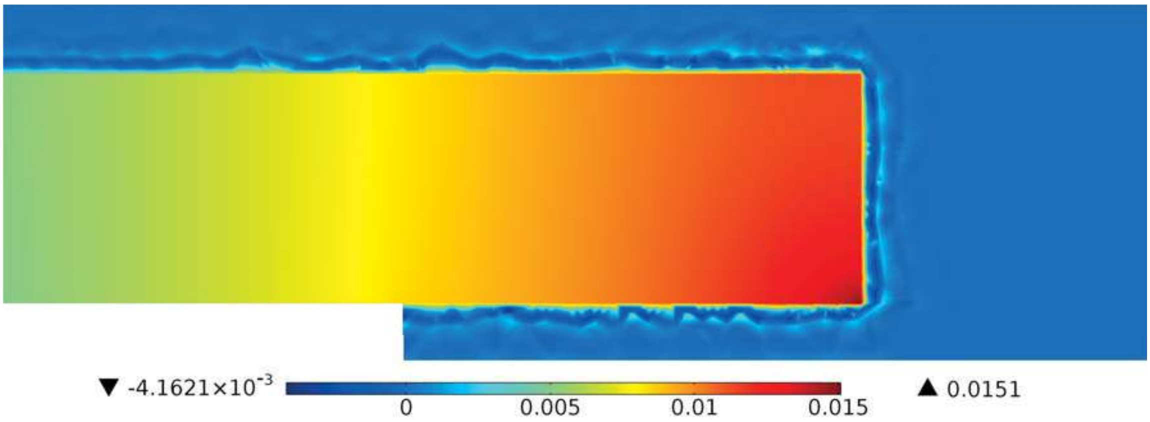

(a) $t_{\mathrm{sim}} = 1\mathrm{s}$

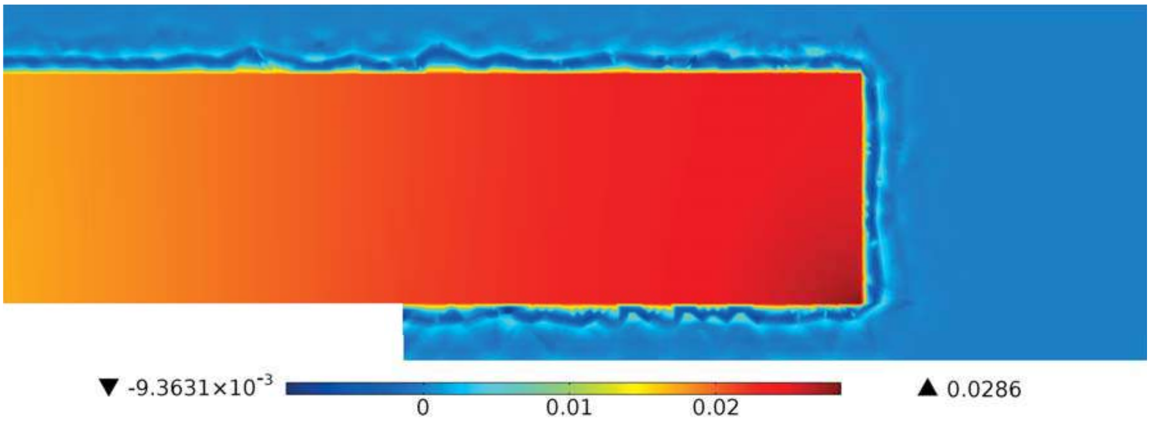

(b) $t_{\mathrm{sim}} = 10^3\mathrm{s}$

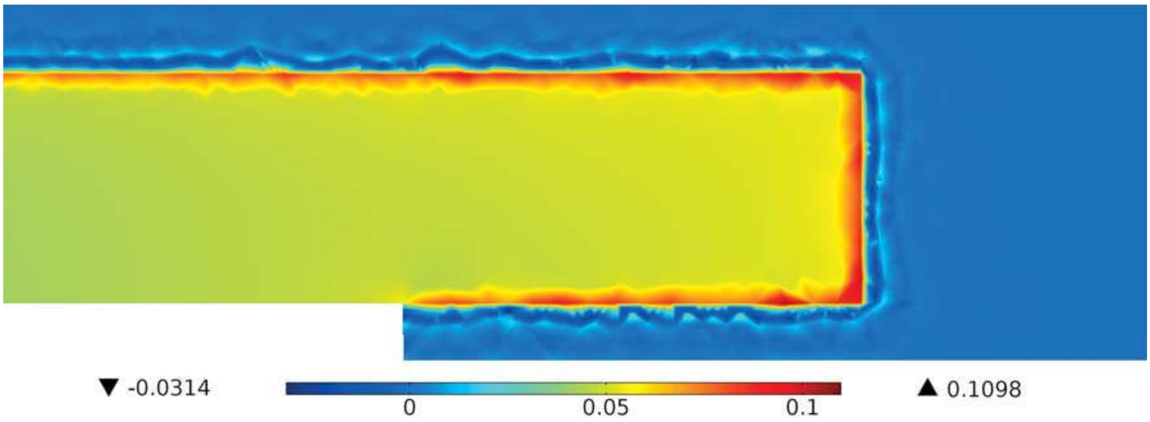

(c) $t_{\mathrm{sim}} = 10^6\mathrm{s}$

Figure 5.18.: Relative vacancy concentration deviation ($C_{\mathrm{v}}/C_{\mathrm{v,eq}} - 1$) piled up in the structure for three different simulated time periods. The cross section is the cut of the blue line in Figure 5.16.

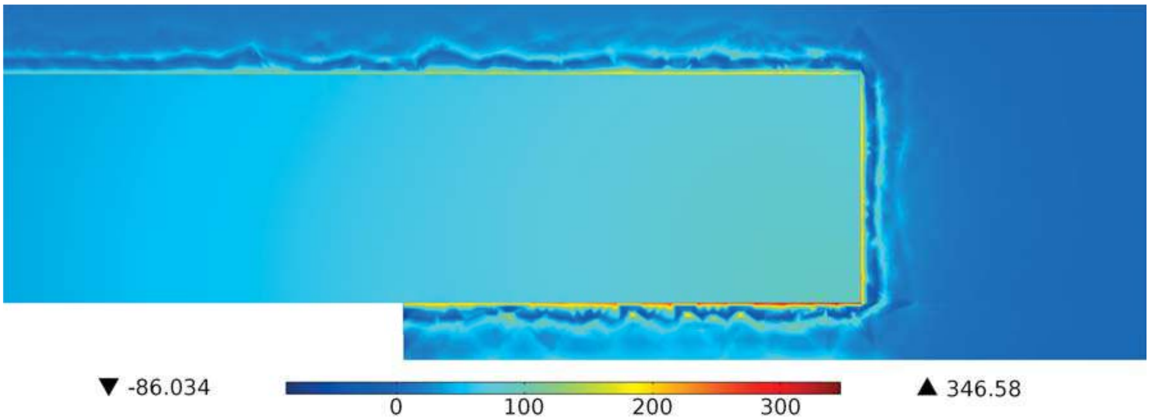

(a) $t_{\mathrm{sim}} = 1\mathrm{s}$

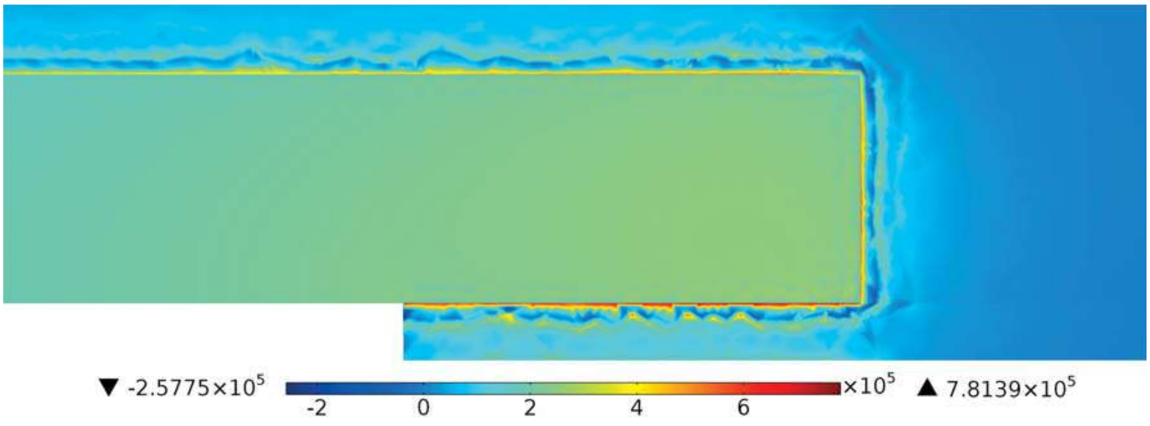

(b) $t_{\mathrm{sim}} = 10^3\mathrm{s}$

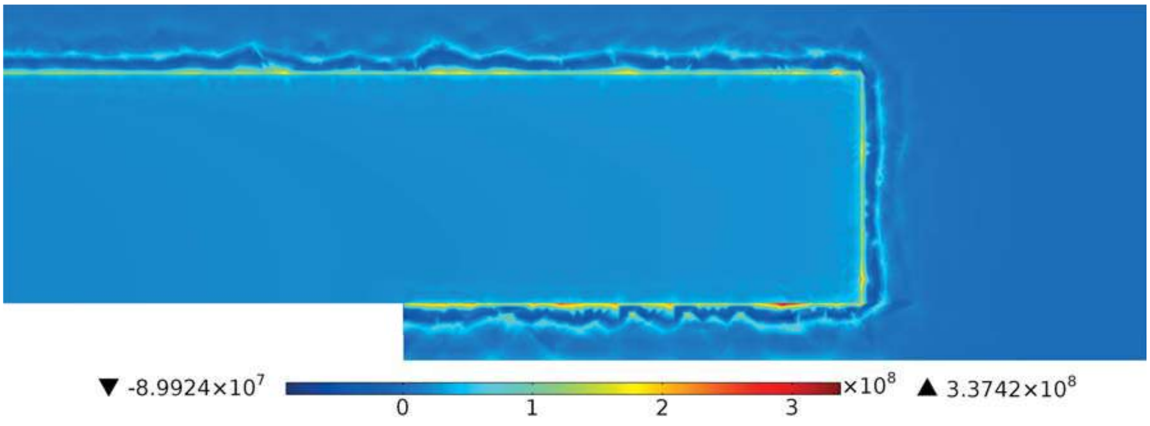

(c) $t_{\mathrm{sim}} = 10^6\mathrm{s}$

Figure 5.19.: *Von Mises* stress in $\mathrm{N/m^2}$ build-up in the structure for three different simulated time periods. The cross section is the cut of the blue line in Figure 5.16.

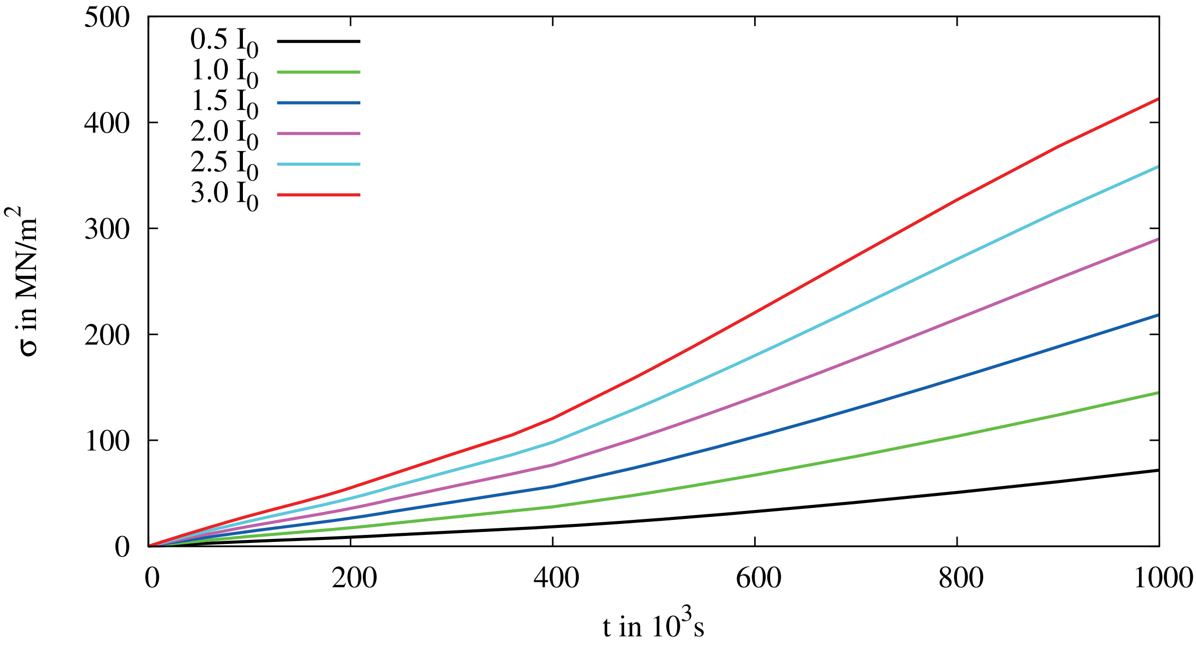

Figure 5.20.: Maximum *Von Mises* stress build-up at the interface for different currents.

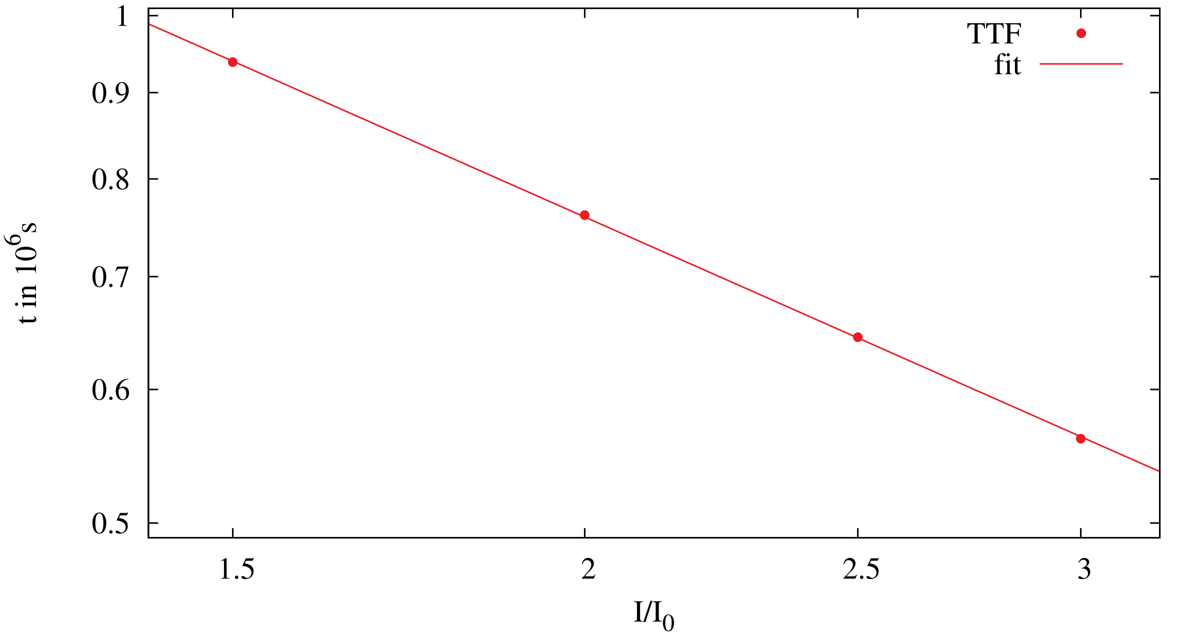

Figure 5.21.: TTF for different currents with a fitting to *Black*'s equation. The axis are logarithmically scaled.

5.5. Void Growth and Evolution

After a certain stress is reached in the structure a crack or a void forms. In the case that a crack forms it can lead to an open circuit failure causing a malfunction of the whole integrated circuit. For the scenario of a phase one failure the estimation of the TTF ends with the analysis shown in the section before.

In the second case the formation of a void is the result of the first phase. Thereby, the structure does not fail immediately, but a void will get formed in the structure. This void starts to move in the structure due to EM at its surface as well as it might grow. For the open TSV segment (cf. Figure 5.16) this simulation was performed using the phase field method described in Section 3.6. Thereby, a void is placed in the aluminium at the region where the highest stress was found in the simulation before. As the highest stress was located at the interface between the aluminium and the tungsten close to the corner in the aluminium, the void was placed under the interconnect joining the TSV to the planar metallization structure. Due to the symmetry of the problem with respect to the blue line indicated in Figure 5.16, only one half of the structure was simulated with appropriate boundary conditions at the boundary formed by cutting through the blue line. These boundary conditions are vanishing fluxes for electric currents, vacancies, and the phase field function as well as free to slip at the cutting surface for the mechanical calculations. The results of this simulations are shown in Figure 5.22.

First the void starts to move in the structure. The movement is in the same direction as the current density and therefore in the direction towards the tungsten. This phase is depicted in Figure 5.22a. It shows the aluminium layer from the direction where the tungsten is placed. The tungsten layer was left out to reveal the void. On the right side the cut due to the mirror symmetry is located. In Figure 5.22b the void has reached the end of the aluminium structure, where the aluminium touches the silicon oxide. Due to the tendency of the void to minimize the surface energy the before circular void reforms into a semicircle minimizing the surface area. From now on the void stops moving and only continuous to grow as depicted in Figure 5.22c. This evolution of the void influences the cross section of the conducting metal and therefore, affects the resistance of the metallization of ICs.

5.6. Resistance Development due to Void Evolution

The simulation of the void evolution is accompanied by a resistance evaluation. In Figure 5.23 the resistance development in time is shown for different current densities. Due to the growth of the void the conducting cross section decreases leading to a higher resistance. Furthermore, the current density at the void surface increases too, leading to higher EM driving forces at the void surface accelerating the resistance growth.

Here, the failure is caused by an increase of the resistance above a certain value depending on the circuit the open TSV is used in. Therefore, a criterion has to be chosen by the circuit designers with regard to the circuit. For the fit to *Black*'s equation an increase of the resistance to twice the value and three times the value of the initial

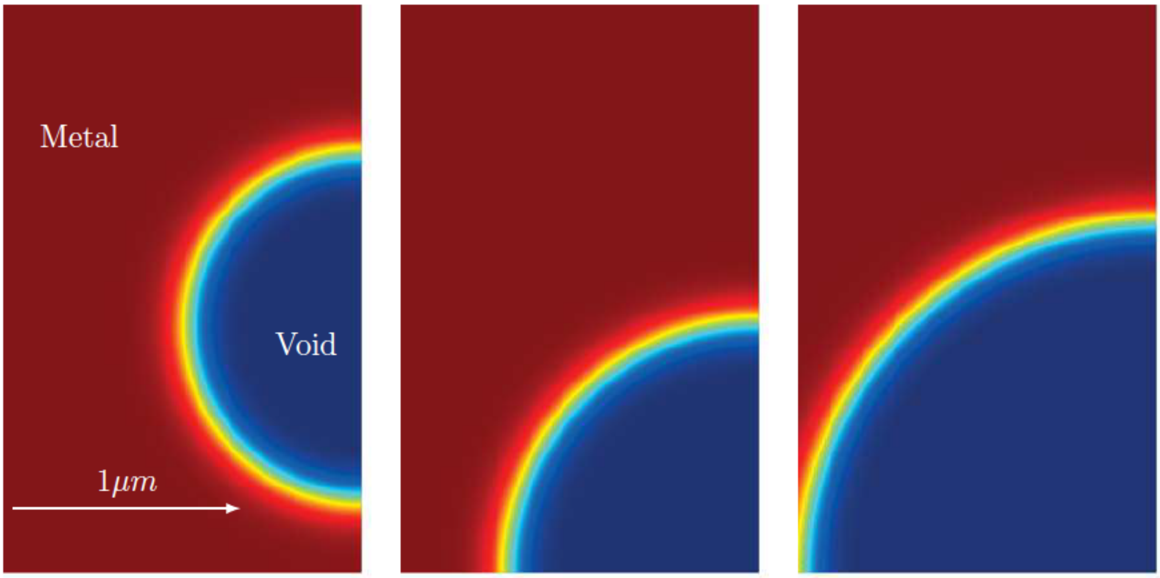

(a) $t = 0\,\mathrm{s}$ (b) $t = 1 \cdot 10^6\,\mathrm{s}$ (c) $t = 2 \cdot 10^6\,\mathrm{s}$

Figure 5.22.: Void evolution in time. The void is placed into the structure and starts to move in the current density direction. After a certain time it has reached the end of the aluminium close to the tungsten. The circle shape deforms to a half circle to reduce the surface energy which is proportional to the surface itself. After this phase the vacancies accumulate at the void surface whereby it grows. Due to the increase of the current density along the surface the growth process gets accelerated.

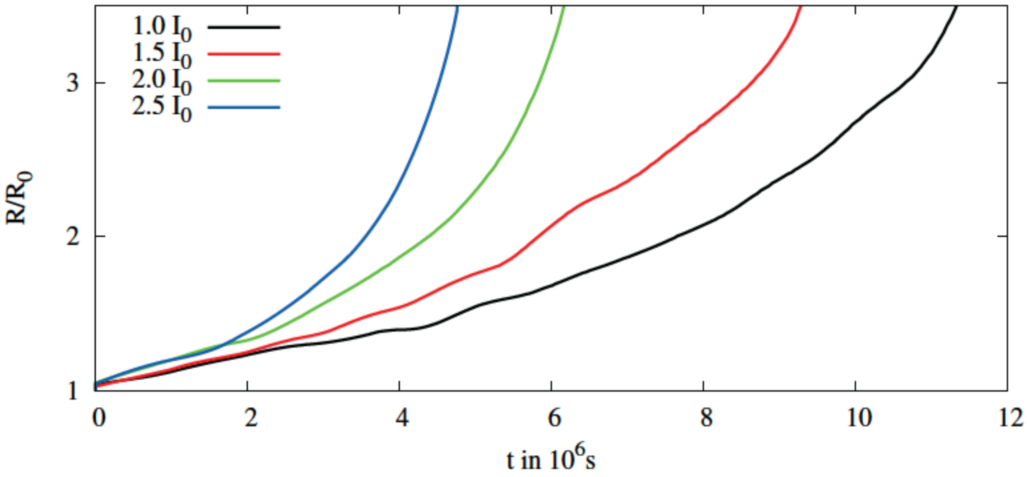

Figure 5.23.: Resistance growth due to void movement and growth in the open TSV structure for different electrical currents.

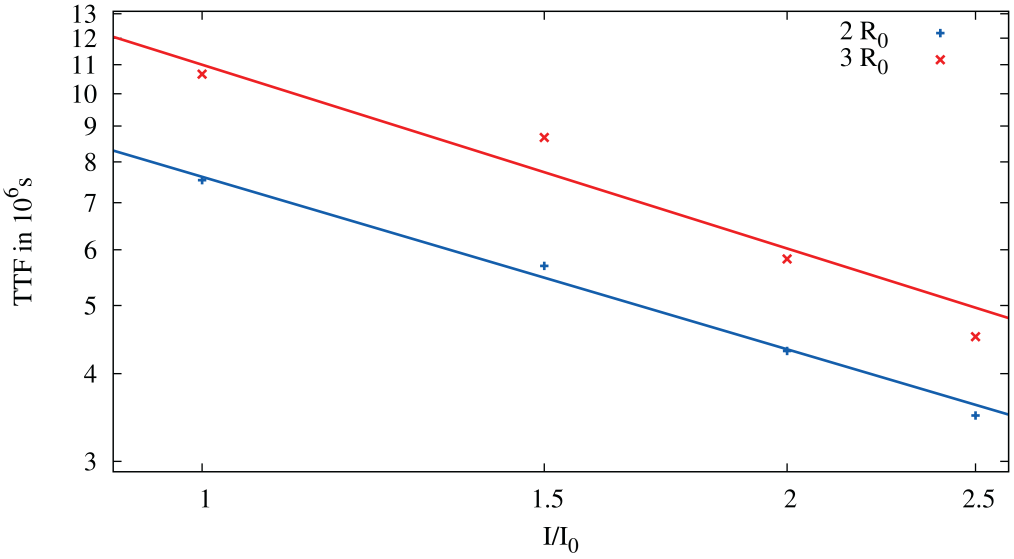

Figure 5.24.: Fitting of the TTF to *Black*'s equation.

resistance was chosen. In Figure 5.24 the data points of the TTF for different currents for both criteria are plotted and the graphs of the two fits are sketched, again using a log-log plot. For the double value criterion a current exponent of 0.81 and for the triple value of 0.87 were obtained.

Changes in the residual stress, due to the fabrication process or surrounding elements as well as actual operating temperature distributions, have to be accounted for in order to gain meaningful TTF predictions.

Chapter 6

Summary and Outlook

For many decades Moore's law has been the main driving force behind transistor scaling and miniaturization efforts in the semiconductor industry. For each technology node the technological problems become more pronounced and will inevitable reach fundamental physical limits in the near future. Thus, alternative trends in technological advancements, which attempt to deal with the integration of devices beyond memory and logic, dubbed More-than-Moore, gain in importance. One of those trends is the addition of technologies which do not scale according to Moore's Law but nevertheless add functionality and complement to the trend to integrate digital logic, analog/RF, memory, sensors, actuators, bio chips, etc. in a single package. This requires the three-dimensional stacking of different technologies by using TSVs. The resulting benefits are denser device packaging, lower power consumption, and reduced RC-delay.

Although TSVs present many advantages, there are still significant reliability concerns with this technology, such as permissible thermal budget, mechanical stability, process variability, and device reliability, which must be addressed before mass production is viable. One of the main concerns for the reliability of open TSVs is their degradation under EM.

This work concerns itself with the quantum mechanical understanding of EM. Furthermore, the development of the continuum mechanical descriptions of EM including the material flow and the thereby arising long-time failure issues is addressed. Finally the state of the art models, which cover the two different modes of failure are presented and their implementation in a commercial tool is described. The two failure modes differ in the way the device malfunction is triggered, as previously studied in dual-damascene interconnects. In the first mode a crack interrupts the conduction of the metallization structure due to an increased mechanical stress, while in the second mode a void is formed which does not immediately trigger a failure. This void migrates and grows inside the metallization, until its induced resistance overcomes a critical value needed for the system to operate uninterruptedly. In this study it was found that open TSV structures are prone to the same modes of failure as interconnects, while particular attention must be paid to the metal-metal interfaces.

In order to assess the reliability of a state-of-the-art open TSV structure, the EM through the metal layers in the TSV is analyzed. Two different metals are employed in the TSV design: aluminium for the top and bottom wafer contacts and tungsten for the current conduction through the wafer. The first step was the analysis and identification of the parameters showing the highest EM impact and their relations to the adjoining metal layers. In order to achieve this the interface behavior between the metals was studied to determine the worst case scenario. It was found that, for certain material combinations, a blocking behavior between the metals leads to a vacancy pile up at the interface resulting in an increased stress, which eventually triggers one of the two possible failure modes. This worst case is unfortunately the scenario when using a metal combination of tungsten and aluminium as employed in the considered open TSV structure. Therefore, it was found that a vacancy pile-up and thereby increased stress can be found at the top and bottom of the TSV, where the tungsten and aluminum layers are in contact.

Since EM is driven by the divergence of the current density, locations where current crowding occurs are highly relevant. Therefore, these locations were identified and are typically situated at corners and sharp edges. They are further augmented at interfaces with conductivity discontinuities. As this is a feature found in the particular device under investigation a variation of the geometry and conductivity was carried out in order to investigate methods to minimize the current crowding. For the studied device, current crowding was found to be most pronounced at the tungsten/aluminium overlap at the TSV top. As a general rule regarding overlapping metal lines the layer with the higher resistance should have a proportionally higher layer thickness to achieve a more homogeneous current density at the interface. This was found not to be the case for the studied structure, meaning that increasing the tungsten thickness would alleviate the interface current crowding.

Due to the high aspect ratios present in the TSV, a fully three-dimensional EM simulation of the entire structure using the finite element approach is only manageable with a fairly coarse mesh, reducing the accuracy of the results. Therefore, only a segment of the TSV structure was selected for detailed analysis, taking into account the current crowding simulations carried out previously. In addition, considering the fact that tungsten has a higher EM resistance than aluminium, a separate consideration was made for the top of the TSV. These simulations revealed the locations, where the highest tensile stress is located. The location is typically close to the interfaces between the aluminium and the tungsten as well as the aluminium and the silicon dioxide. Void nucleation or cracking will appear there as soon as a critical threshold stress is exceeded.

Assuming a critical stress in the order of $200\mathrm{MN/m^2}$ the time to failure varies between about 110 days and 65 days under accelerated conditions, while the applied current is varied from $1.5\mathrm{MA/cm^2}$ to $3\mathrm{MA/cm^2}$, respectively. The results were further used to calibrate the well known *Black* equation. This calibration showed the validity of the compact model based on *Black* equation and allows for an extrapolation to normal operating conditions for the technology under consideration and thus completes the assessment of the first mode of failure under EM.

Following this simulation the void evolution model was employed to examine the second failure mode under EM. Since the phase field model allows for the simulation of the void propagation without computationally expensive remeshing, it was implemented in the finite element code for the second failure mode to study open TSV structures. For the study an initial void was placed at the locations where the previous simulations showed high stress levels. This void begins to migrate in the aluminium in the direction of the current, while continuously increasing the resistance of the metal line.

While in the initial failure mode a critical stress determined failure, the mode studied in the second section deals with a failure due to an increased resistance. Reaching the threshold resistance determines the time to failure for a given device. The time to failure for the open TSV was analyzed and compiled within a compact model, suitable for failure predictions under non-accelerated operating conditions. Assuming a failure is reached, when the resistance increases to double or triple the unvoided metal resistance, a failure will occur after operating for 870 days or 1270 days, respectively, under accelerated conditions, when a current density of $1\mathrm{MA}/\mathrm{cm}^2$ is applied.

The demonstrated EM results and simulations provide circuit designers with a useful tool based on TCAD methods to estimate the time-to-failure due to EM of modern interconnect structures. Nevertheless further extensions for EM simulations should be addressed. In future studies the residual stress emerging from the fabrication process, which has a significant impact on the device reliability must be taken into account. Therefore, this stress must also be evaluated and included in the simulations. As this stress is not only dependent on the metal line itself, but also on the surrounding structures and materials, the variability of the material properties has to be considered as well. The influence of the process variability on the device performance is usually modeled using a statistical approach. Furthermore, the micro-structure of the metallization (eg. bamboo structure) and the surrounding interfaces can impact the EM behavior significantly and should be also taken into account.

The impact of the micro-structure, grain boundaries, and interfaces to the surrounding materials are especially pronounced in nano-interconnects. Nano-sized interconnects are connectors between the metal lines and the drains or sources of nano-sized transistors. An approach to model EM in these structures must be examined. The question, if the continuum model implemented in this work is still valid, has to be answered and the EM behavior at grain boundaries and interfaces must be properly addressed. Furthermore, the coefficient Z^* is currently treated as a material-dependent, but geometry-independent constant. Due to an increased number of scattering sources, such as at a rough metal interface, Z^* will likely need to be adjusted according to the metal thickness or grain sizes.

Appendix A

The Asymptotic Limit of the Phase Field Model

In this chapter the behavior of the phase field model in its asymptotic limit is discussed, as described by *Bhate et al.* [9]. The analysis shows that in the limit of an infinitely thin interface the phase field model equations converge to the equations of the sharp interface model. The interface thickness, described in Section 3.6, is controlled by the parameter ϵ_{pf} and, therefore, the asymptotic limit to an infinitely thin interface is accomplished by driving this parameter against zero [38].

For an easier handling the governing equations are rewritten in a dimensionless form [9]:

$$\frac{\partial \phi}{\partial \tilde{t}} = \frac{2}{\tilde{\epsilon}\pi}\tilde{\nabla}\cdot\left(\tilde{D}_{\text{s}}\left(\tilde{\nabla}\tilde{\mu} - \chi\tilde{\nabla}\tilde{\phi}_{\text{E}}\right)\right) - \frac{4}{\tilde{\epsilon}\pi}\tilde{J}_{\text{nv}}, \tag{A.1}$$

$$= \frac{2}{\tilde{\epsilon}\pi}\tilde{\nabla}\cdot\left(\tilde{D}_{\text{s}}\tilde{\nabla}\tilde{\mu}^{*}\right) - \frac{4}{\tilde{\epsilon}\pi}\tilde{J}_{\text{nv}}, \tag{A.2}$$

where in $\tilde{\nabla}\tilde{\mu}^{*}$ both the gradient of the chemical potential $\tilde{\nabla}\tilde{\mu}$ and the therm due to the electric field $-\chi\tilde{\nabla}\tilde{\phi}_{\text{E}}$ are added and

$$\tilde{\mu} = \frac{4}{\tilde{\epsilon}\pi}\left(f'(\phi) - \tilde{\epsilon}^{2}\tilde{\Delta}\phi\right) + 2\Lambda\frac{\partial\tilde{W}}{\partial\phi}, \tag{A.3}$$

where the connection between the dimensionless quantities and the quantities with units

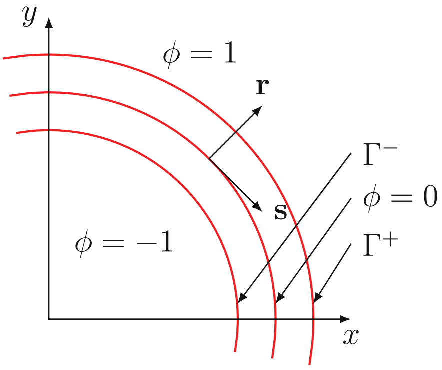

Figure A.1.: Illustration of the partitioning of the void metal region into interface, void, and metal domains for the inner expansion [9].

are given by

$$\epsilon_{\mathrm{pf}} = \tilde{\epsilon} a, \tag{A.4}$$

$$x = \tilde{x} a, \tag{A.5}$$

$$t = \tilde{t} \frac{a^4}{\Omega \gamma_{\mathrm{s}} D_{\mathrm{s}}}, \tag{A.6}$$

$$\phi_{\mathrm{E}} = \tilde{\phi}_{\mathrm{E}} E^* a, \tag{A.7}$$

$$W = \tilde{W} W^*, \tag{A.8}$$

$$J_{\mathrm{nv}} = \tilde{J}_{\mathrm{nv}} \frac{\Omega \gamma_{\mathrm{s}} D_{\mathrm{s}}}{a^3}, \tag{A.9}$$

$$\mu = \tilde{\mu} \frac{\Omega \gamma_{\mathrm{s}}}{a}. \tag{A.10}$$

There a is a characteristic length, E^* is a characteristic electric field strength, and W^* is a characteristic strain energy. Furthermore, Ω is the volume of an atom in the lattice, γ_{s} is the surface energy of the metal/void interface, and D_{s} is the diffusion coefficient at the metal surface.

In the further discussion the tilde sign above the dimensionless values will be omitted for easier reading. If a distinction is needed, it will be explicitly pointed out. The parameters in (A.1) and (A.3) are given by

$$\chi = \frac{e Z^* E^* a^2}{\Omega \gamma_{\mathrm{s}}}, \tag{A.11}$$

$$\Lambda = \frac{W^* a}{\gamma_{\mathrm{s}}}, \tag{A.12}$$

where the quantities χ and Λ are dimensionless numbers characteristic for the formulated problem.

For the derivation a local coordinate system is chosen, as already used for the sharp interface model. This coordinate system is extended to the region of the diffuse interface and splits up the simulation domain into three regions. The regions are the metal region, the void region, and the interface region separating the two former (cf. Figure A.1).

The derivations for the asymptotic limit is carried out in two steps. First the formulas are transformed into the local coordinate system. This step is followed by the introduction of the *Taylor* expansion in ϵ of the functions and a splitting of the equations in terms of ϵ-orders.

For the local coordinate system, some definitions are required regarding the calculation of the normal vector $\mathbf{n}$

$$\mathbf{n} = -\nabla_x r \tag{A.13}$$

and the curvature κ for the $\phi = 0$ contour.

$$\kappa = \Delta_x r \tag{A.14}$$

The subscript x is used for the common differential operators. Furthermore, the normal velocity of the interface is expressed by the time derivative of the $\phi = 0$ contour (interface)

$$v_n = \frac{\partial r}{\partial t}, \tag{A.15}$$

and the r-coordinate of the local coordinate system is normalized as

$$\rho = \frac{r}{\epsilon}. \tag{A.16}$$

As the asymptotic expansion is carried out in the local coordinate system all functions have to be expressed in this coordinate system as well:

$$\psi\left(\mathbf{x}\right) = \Psi\left(r\left(\mathbf{x}\right), s\left(\mathbf{x}\right)\right) \tag{A.17}$$

For the time derivative the chain rule gives

$$\frac{\partial \psi}{\partial t} = \Psi_{,t} + \Psi_{,s}\frac{\partial s}{\partial t} + \Psi_{,r}\frac{\partial r}{\partial t}, \tag{A.18}$$

where the indices after the comma stand for the derivative

$$\Psi_{,k} = \frac{\partial \Psi}{\partial k}. \tag{A.19}$$

By again employing the chain rule the ∇_x operator can be expressed in the new coordinate system by

$$\nabla_x \psi = \Psi_{,s}\nabla_x s + \Psi_{,r}\nabla_x r. \tag{A.20}$$

The last needed differential operator is the *Laplace* operator given by

$$\Delta_x \psi = \Delta_s \Psi + \Psi_{,r}\Delta_x r + \Psi_{,rr}|\nabla r|^2 \tag{A.21}$$

in the new coordinate system, where the first term, containing only functions Ψ differentiated with respect to s, is defined by

$$\Delta_s \Psi = \Psi_{,ss}|\nabla s|^2 + \Psi_{,s}\Delta_x s. \tag{A.22}$$

The boundary conditions for the Γ^- and Γ^+ contour for the phase field function (cf. Figure A.1) are given by

$$\lim_{x\to\Gamma^\pm} \phi = \pm 1 \tag{A.23}$$

as there the pure metal or the pure void starts and

$$\lim_{x\to\Gamma^\pm} \frac{\partial\phi}{\partial\mathbf{n}} = 0, \tag{A.24}$$

as the phase field function has to be a smooth function everywhere and, therefore, also at the boundary contours between the metal and the interface and between the void and the interface. The flux at the interface has to be limited to the interface leading to a third boundary condition of zero flux from the interface into the metal or the void given by

$$\lim_{x\to\Gamma^\pm} \left(\frac{2D_\mathrm{s}}{\epsilon\pi}\left(\nabla\mu - \chi\nabla\varphi\right)\right) = 0. \tag{A.25}$$

The inner expansion of the order parameter and the chemical potential, where the EM therm is included, is the *Taylor* expansion with respect to the interface thickness controlling parameter ϵ.

$$\phi = \phi_0 + \epsilon\phi_1 + \epsilon^2\phi_2 + \mathcal{O}(\epsilon^3) \tag{A.26}$$

$$\mu = \mu_0 + \epsilon\mu_1 + \epsilon^2\mu_2 + \mathcal{O}(\epsilon^3) \tag{A.27}$$

$$\mu^* = \mu_0^* + \epsilon\mu_1^* + \epsilon^2\mu_2^* + \mathcal{O}(\epsilon^3) \tag{A.28}$$

The constant multipliers $\frac{1}{n!}$ from the *Taylor* expansion are absorbed into the functions ϕ_n, μ_n and μ_n^*. First the differential operators (A.18)-(A.21) for functions in the local coordinate system in (A.1) are employed, resulting in

$$\begin{aligned}
\frac{\partial\phi}{\partial t} &= \phi_{,t} + \underbrace{\phi_{,s}}_{=0}\frac{\partial s}{\partial t} + \phi_{,r}\frac{\partial r}{\partial t} \\
&= \nabla\cdot\left(\frac{2D_\mathrm{s}}{\epsilon\pi}\nabla\mu^*\right) - \frac{4}{\epsilon\pi}J_\mathrm{nv} = \frac{2}{\epsilon\pi}\nabla D_\mathrm{s}\cdot\nabla\mu^* + \frac{2}{\epsilon\pi}D_\mathrm{s}\Delta\mu^* - \frac{4}{\epsilon\pi}J_\mathrm{nv} \\
&= \frac{2}{\epsilon\pi}\left(\frac{\partial D_\mathrm{s}}{\partial\phi}\underbrace{\phi_{,s}}_{=0}\nabla_x s + \frac{\partial D_\mathrm{s}}{\partial\phi}\phi_{,r}\nabla_x r\right)\cdot\left(\mu^*_{,s}\nabla_x s + \mu^*_{,r}\nabla_x r\right) + \frac{2}{\epsilon\pi}D_\mathrm{s}\Delta\mu^* - \frac{4}{\epsilon\pi}J_\mathrm{nv} \\
&= \frac{2}{\epsilon\pi}\left(\frac{\partial D_\mathrm{s}}{\partial\phi}\phi_{,r}\mu^*_{,s}\underbrace{\nabla_x r\cdot\nabla_x s}_{=0} + \frac{\partial D_\mathrm{s}}{\partial\phi}\phi_{,r}\mu^*_{,r}\underbrace{\nabla_x r\cdot\nabla_x r}_{=1}\right) + \frac{2}{\epsilon\pi}D_\mathrm{s}\Delta\mu^* - \frac{4}{\epsilon\pi}J_\mathrm{nv} \\
&= \frac{2}{\epsilon\pi}\left(\frac{\partial D_\mathrm{s}}{\partial\phi}\phi_{,r}\mu^*_{,r}\right) + \frac{2}{\epsilon\pi}D_\mathrm{s}\left(\Delta_s\mu^* + \mu^*_{,r}\Delta_x r + \mu^*_{,rr}\right) - \frac{4}{\epsilon\pi}J_\mathrm{nv},
\end{aligned} \tag{A.29}$$

where the derivatives of the phase field function with respect to the tangential direction are zero as in this direction the phase field function is constant (zero). Furthermore, ∇r and ∇s are orthogonal to each other and due to the normalization of $\mathbf{n}$, the inner product of ∇r with itself is equal to one. Using $\frac{\partial}{\partial r} = \frac{1}{\epsilon}\frac{\partial}{\partial \rho}$ (e.g. $\mu^*_{,r} = \frac{\mu^*_{,\rho}}{\epsilon}$), derived from (A.16), results in

$$\epsilon^2 \frac{\pi}{2}\phi_{,t} + \epsilon\frac{\pi}{2}\phi_{,\rho}\frac{\partial r}{\partial t} = \frac{1}{\epsilon}\frac{\partial D_{\mathrm{s}}}{\partial \phi}\phi_{,\rho}\mu^*_{,\rho} + \epsilon D_s \Delta_s \mu^* + D_s \mu^*_{,\rho}\kappa + \frac{1}{\epsilon}D_s\mu^*_{,\rho\rho} - 2J_{\mathrm{nv}}. \tag{A.30}$$

Inserting the inner expansions (A.26) and (A.28) defined above and taking only terms to the first order in ϵ into account leads to the equation

$$\begin{aligned}\epsilon\frac{\pi}{2}\phi_{0,\rho}\frac{\partial r}{\partial t} + \mathcal{O}(\epsilon^2) = {}& \overbrace{\frac{1}{\epsilon}\frac{\partial D_{\mathrm{s}}}{\partial \phi}\phi_{0,\rho}\mu^*_{0,\rho} + \frac{\partial D_{\mathrm{s}}}{\partial \phi}\phi_{0,\rho}\mu^*_{1,\rho} + \epsilon\frac{\partial D_{\mathrm{s}}}{\partial \phi}\phi_{0,\rho}\mu^*_{2,\rho} + \mathcal{O}(\epsilon^2)}^{\frac{1}{\epsilon}\frac{\partial D_{\mathrm{s}}}{\partial \phi}\phi_{,\rho}\mu^*_{,\rho}} + \\ & \overbrace{\epsilon D_{\mathrm{s}}\Delta_s\mu^*_0 + \mathcal{O}(\epsilon^2)}^{\epsilon D_{\mathrm{s}}\Delta_s\mu^*} + \overbrace{D_{\mathrm{s}}\mu^*_{0,\rho}\kappa + \epsilon D_{\mathrm{s}}\mu^*_{1,\rho}\kappa + \mathcal{O}(\epsilon^2)}^{D_{\mathrm{s}}\mu^*_{,\rho}\kappa} + \\ & \overbrace{\frac{1}{\epsilon}D_{\mathrm{s}}\mu^*_{0,\rho\rho} + D_{\mathrm{s}}\mu^*_{1,\rho\rho} + \epsilon D_{\mathrm{s}}\mu^*_{2,\rho\rho} + \mathcal{O}(\epsilon^2)}^{\frac{1}{\epsilon}D_s\mu^*_{,\rho\rho}} - 2J_{\mathrm{nv}}.\end{aligned} \tag{A.31}$$

Reordering the equation by collecting the terms with the same order of ϵ and leaving away the terms of the second order leads to the equation

$$\begin{aligned}\epsilon\frac{\pi}{2}\phi_{0,\rho}\frac{\partial r}{\partial t} = {}& \frac{1}{\epsilon}\left(\frac{\partial D_{\mathrm{s}}}{\partial \phi}\phi_{0,\rho}\mu^*_{0,\rho} + D_{\mathrm{s}}\mu^*_{0,\rho\rho}\right) + \left(D_{\mathrm{s}}\mu^*_{0,\rho}\kappa + \frac{\partial D_{\mathrm{s}}}{\partial \phi}\phi_{0,\rho}\mu^*_{1,\rho} + D_{\mathrm{s}}\mu^*_{1,\rho\rho}\right) \\ & + \epsilon\left(D_{\mathrm{s}}\Delta_s\mu^*_0 + D_{\mathrm{s}}\mu^*_{1,\rho}\kappa + \frac{\partial D_{\mathrm{s}}}{\partial \phi}\phi_{0,\rho}\mu^*_{2,\rho} + D_{\mathrm{s}}\mu^*_{2,\rho\rho} - 2J_{\mathrm{nv}}\right)\end{aligned} \tag{A.32}$$

and the different orders of ϵ can be handled separately giving the following set of equations:

$$\mathcal{O}\left(\epsilon^{-1}\right): \qquad 0 = \overbrace{\frac{\partial D_{\mathrm{s}}}{\partial \phi}\phi_{0,\rho}\mu^*_{0,\rho} + D_{\mathrm{s}}\mu^*_{0,\rho\rho}}^{(D_{\mathrm{s}}\mu^*_{0,\rho})_{,\rho}=0} \tag{A.33}$$

$$\mathcal{O}\left(\epsilon^{0}\right): \qquad 0 = D_{\mathrm{s}}\overbrace{\mu^*_{0,\rho}}^{=0}\kappa + \overbrace{\frac{\partial D_{\mathrm{s}}}{\partial \phi}\phi_{0,\rho}\mu^*_{1,\rho} + D_{\mathrm{s}}\mu^*_{1,\rho\rho}}^{(D_s\mu^*_{1,\rho})_{,\rho}=0} \tag{A.34}$$

$$\mathcal{O}\left(\epsilon^{1}\right): \qquad \frac{\pi}{2}\phi_{0,\rho}\frac{\partial r}{\partial t} = D_{\mathrm{s}}\Delta_s\mu^*_0 + D_{\mathrm{s}}\mu^*_{1,\rho}\kappa + \frac{\partial D_{\mathrm{s}}}{\partial \phi}\phi_{0,\rho}\mu^*_{2,\rho} + D_{\mathrm{s}}\mu^*_{2,\rho\rho} - 2J_{\mathrm{nv}} \tag{A.35}$$

The first over-brace in (A.33) shows that the term $D_s\mu^*_{0,\rho}$ is constant in ρ. With the definition of the diffusion coefficient

$$D_{\mathrm{s}}(\phi) = \begin{cases} 1 & \text{if } |\phi| < 1, \\ 0 & \text{otherwise} \end{cases}, \tag{A.36}$$

it can be concluded that

$$\mu_0^* = F\left(s,t\right) \tag{A.37}$$

and the first over-brace in (A.34) is zero as μ_0^* is independent of ρ and the second over-brace in (A.34) can be handled like the first over-brace in (A.33).

$$\mu_1^* = G\left(s,t\right) \tag{A.38}$$

Applying the same procedure of the transformation into the local coordinate system and applying the *Taylor* expansion to the chemical potential results in the equation

$$\begin{aligned}\frac{\pi}{4}(\mu_0 + \epsilon\mu_1 + \mathcal{O}(\epsilon^2)) &= \frac{1}{\epsilon}(-\phi_{0,\rho\rho} + f'(\phi_0)) \\ &+ \left(-\phi_{0,\rho}\kappa - \phi_{1,\rho\rho} + f''(\phi_0)\phi_1 + \frac{\pi}{2}\Lambda\frac{\partial W_0}{\partial \phi_0}\right) + \mathcal{O}(\epsilon),\end{aligned} \tag{A.39}$$

and a separation of the equation into a set of equations ordered by the order in ϵ gives

$$\mathcal{O}\left(\epsilon^{-1}\right): \qquad 0 = -\phi_{0,\rho\rho} + \overbrace{f'(\phi_0)}^{-\phi_0} \tag{A.40}$$

$$\mathcal{O}\left(\epsilon^{0}\right): \qquad \frac{\pi}{4}\mu_0 = -\phi_{0,\rho}\kappa - \phi_{1,\rho\rho} + f''(\phi_0)\phi_1 + \frac{\pi}{2}\Lambda\frac{\partial W_0}{\partial \phi_0}, \tag{A.41}$$

where the double obstacle function defined in Section 3.6 was used for the bulk free energy defined by

$$f\left(\phi\right) = \begin{cases} \frac{1}{2}\left(1-\phi^2\right) & \text{if } |\phi| < 1, \\ \infty & \text{otherwise} \end{cases}. \tag{A.42}$$

Setting the term of the order $\frac{1}{\epsilon}$ equal zero leads to the differential equation

$$\phi_{0,\rho\rho} + \phi_0 = 0 \tag{A.43}$$

with the solutions

$$\phi_0 = A\sin\left(\rho\right) + B\cos\left(\rho\right), \tag{A.44}$$

where, due to the boundary conditions (A.23) and (A.24), A equals one and B equals zero and the thickness of the interface in the ρ coordinate is π. Taking the terms of the zeroth order of ϵ of (A.39) and rearranging them leads to

$$\phi_{1,\rho\rho} - f''(\phi_0)\phi_1 = -\frac{\pi}{4}\mu_0 - \phi_{0,\rho}\kappa + \frac{\pi}{2}\Lambda\frac{\partial W_0}{\partial \phi_0} = R, \tag{A.45}$$

where R is not a function of ϕ_1. This equation has the same structure as the derivative of (A.43) with respect to ρ. Therefore only the trivial solution can meet the boundary conditions given by (A.24) and

$$\phi_1\left(\pm\frac{\pi}{2}, s, t\right) = 0. \tag{A.46}$$

Integrating (A.45) in ρ direction over the whole interface region results in

$$\frac{\pi}{4}\mu_0 \underbrace{\int_{\Gamma^+}^{\Gamma^-} \phi_{0,\rho} d\rho}_{2} = -\kappa \underbrace{\int_{\Gamma^+}^{\Gamma^-} \phi_{0,\rho}^2 d\rho}_{\frac{\pi}{2}} + \frac{\pi}{2}\Lambda \underbrace{\int_{\Gamma^+}^{\Gamma^-} \frac{\partial W_0}{\partial \phi_0}\phi_{0,\rho} d\rho}_{[\![W_0]\!]}, \tag{A.47}$$

where the under-braces give the results of the integrals. With the assumption of zero elastic strain energy in the void this leads to

$$\mu_0 = -\kappa + \Lambda W_0. \tag{A.48}$$

This is the same equation as (3.47) and shows that the chemical potential in the asymptotic limit converges to the sharp interface model. Coming back to (A.32), taking the terms of first order in ϵ, and again integrating over the interface in ρ gives

$$\begin{aligned}\frac{\pi}{2}\overbrace{\frac{\partial r}{\partial t}}^{v_n} \overbrace{\int_{\Gamma^+}^{\Gamma^-} \phi_{0,\rho} \mathrm{d}\rho}^{2} = D_\mathrm{s}\Delta_s\mu_0^* \overbrace{\int_{\Gamma^+}^{\Gamma^-} \mathrm{d}\rho}^{\pi} + \int_{\Gamma^+}^{\Gamma^-} D_\mathrm{s} \overbrace{\mu_{1,\rho}^*}^{0} \kappa \mathrm{d}\rho + \\ \int_{\Gamma^+}^{\Gamma^-} \underbrace{\left(\frac{\partial D_\mathrm{s}}{\partial \phi}\phi_{0,\rho}\mu_{2,\rho}^* + D_\mathrm{s}\mu_{2,\rho\rho}^*\right)}_{\left(D_\mathrm{s}\mu_{2,\rho}^*\right)_{,\rho}=0} \mathrm{d}\rho - \int_{\Gamma^+}^{\Gamma^-} 2J_\mathrm{nv}\mathrm{d}\rho,\end{aligned} \tag{A.49}$$

where for the third term on the right hand side the zero flux condition was employed, resulting in the equation for the normal velocity of the sharp interface model

$$\begin{aligned} v_n &= \Delta_s\mu_0^* - \hat{D}\left(\mu_\mathrm{bv} - \mu_\mathrm{sv}\right) \\ &= \Delta_s\mu_0 - \chi\Delta_s\phi_\mathrm{E} - \hat{D}\left(\mu_\mathrm{bv} - \mu_\mathrm{sv}\right). \end{aligned} \tag{A.50}$$

These evaluations show that the phase field model for ϵ_pf going to zero converges to the sharp interface model and can therefore be used for the simulations of voids as long as ϵ_pf is chosen carefully. The upper limit is in the order of the smallest curvature occurring at the surface of the voids. The lower limit is given by the meshing resolution. From one side of the boundary region to the other a minimum of five meshing elements is needed to guarantee the stability of the FEM simulation, as was found by empirical studies.

Appendix B

Vacancies in a Crystal Lattice

According to [16, 51] the appearance of vacancies in a lattice can be explained by thermodynamical arguments. Suppose atoms are taken away from lattice positions and migrated to the surface leaving back vacancies. This kind of defects are called *Schottky* defects illustrated in Figure B.1. By assuming an atom positioned on a lattice site has the energy $-\epsilon$ and an empty position has zero energy the state energy of a lattice with N_0 defects can be expressed by

$$U = \epsilon N_0. \tag{B.1}$$

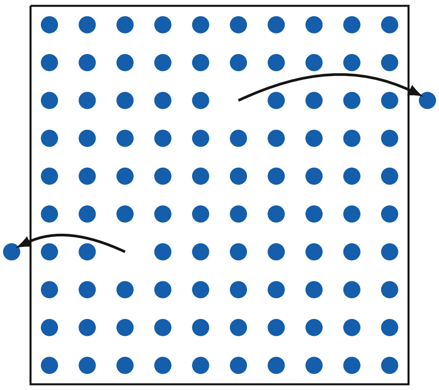

Figure B.1.: Crystal lattice with atoms migrated to the surface leaving back *Schottky* defects [51].

As the vacancies are indistinguishable the number of distinct ways of distributing N_0 vacancies in a lattice with N lattice sites is given by

$$N_\Gamma = \frac{N!}{N_0!(N - N_0)!}. \tag{B.2}$$

For a micro-canonical assembly, the entropy is defined by

$$S = k_\mathrm{B} \ln N_\Gamma. \tag{B.3}$$

Employing *Stirling*'s approximation for big N

$$\ln n! \approx n \ln n - n + \frac{1}{2} \ln 2\pi n, \tag{B.4}$$

and omitting the terms of the order of $\ln n$ results in

$$S = k_\mathrm{B} \Big[N \ln N - N_0 \ln N_0 - (N - N_0) \ln (N - N_0) \Big]. \tag{B.5}$$

With (B.1) the entropy can be expressed as a function of the state energy and can further be related to the temperature by

$$\frac{1}{T} = \left(\frac{\partial S}{\partial U} \right)_N, \tag{B.6}$$

resulting in

$$\begin{aligned} \frac{1}{T} &= k_\mathrm{B} \left(\frac{\partial S}{\partial N_0} \right)_N \frac{\partial N_0}{\partial U} && \text{(B.7)} \\ &= k_\mathrm{B} \Big[\ln (N - N_0) - \ln N_0 \Big] \frac{\partial N_0}{\partial U} && \text{(B.8)} \\ &= \frac{k_\mathrm{B}}{\epsilon} \ln \frac{N - N_0}{N_0}. && \text{(B.9)} \end{aligned}$$

The final result can be rewritten giving

$$\frac{N_0}{N} = \frac{1}{\mathrm{e}^{\frac{\epsilon}{T k_\mathrm{B}}} - 1}, \tag{B.10}$$

which makes only sense when the ratio is much less then one. Otherwise the solid would by perforated with holes and collapse. For a typical energy value ϵ of 1eV $\epsilon / T k_\mathrm{B}$ is in the range of 39 and the ratio of vacancies to the total available sites is in the order of 10^{-17} at room temperature. For small temperature the vacancy to lattice sites ratio function converges to

$$\frac{N_0}{N} = \mathrm{e}^{-\frac{\epsilon}{k_\mathrm{B} T}} \tag{B.11}$$

and has the form of an *Arrhenius* law used in the modeling of electromigration introduced in Chapter 3.

The specific heat for vacancy formation can be calculated by [48]

$$C = \frac{\partial U}{\partial T} = \frac{\partial (\epsilon N_0)}{\partial T} = N k_\mathrm{B} \left(\frac{\epsilon}{2 k_\mathrm{B} T} \right)^2 \operatorname{sech} \left(\frac{\epsilon}{2 k_\mathrm{B} T} \right)^2 \tag{B.12}$$

and vanishes at low temperature due to the excitation gaps. At high temperature the energy spectrum is bounded from above. For practically used materials not only the configuration entropy but also other entropies like the vibration entropy are present. Still the derivation shows that in a real crystal lattice vacancies are always present.

Bibliography

[1] *International technology roadmap for semiconductors (ITRS).* 2013. http://www.itrs.net/reports.html.

[2] Andricacos, P., Uzoh, C., Dukovic, J., Horkans, J., and Deligianni, H. Damascene copper electroplating for chip interconnections. *IBM J. Res. Dev. 42*, 5 (1998), 567–574.

[3] Ashcroft, N., and Mermin, N. *Solid state physics.* Saunders College, Philadelphia, 1976.

[4] Basaran, C., and Lin, M. Damage mechanics of electromigration induced failure. *Intl. J. Solids Struct. 40*, 1–2 (2008), 66–79.

[5] Basaran, C., Lin, M., and Ye, H. A thermodynamic model for electrical current induced damage. *Intl. J. Solids Struct. 40*, 26 (2003), 7315–7327.

[6] Bathe, K.-J., and Wilson, E. L. Numerical methods in finite element analysis.

[7] Beyne, E. 3D system integration technologies. In *Intl. Symposium on VLSI Technology, Systems, and Applications* (2006), pp. 1–9.

[8] Bhate, D. N., Bower, A. F., and Kumar, A. A phase field model for failure in interconnect lines due to coupled diffusion mechanisms. *J. Mech. Phys. Solids 50*, 10 (2002), 2057–2083.

[9] Bhate, D. N., Kumar, A., and Bower, A. F. Diffuse interface model for electromigration and stress voiding. *J. Appl. Phys. 87*, 4 (2000), 1712–1721.

[10] Black, J. R. Mass transport of aluminum by momentum exchange with conducting electrons. In *Proc. Reliability Physics Symposium* (1967), pp. 148–159.

[11] Black, J. R. Aluminum conductor failure by mass transport. In *Proc. Intl. Congress on Microelectronics, Munich* (1968), pp. 141–162.

[12] Black, J. R. Electromigration–A brief survey and some recent results. *IEEE Trans. Electron Devices 16*, 4 (1969), 338–347.

[13] Black, J. R. Electromigration failure modes in aluminum metallization for semiconductor devices. *Proc. IEEE 57*, 9 (1969), 1587–1594.

[14] Blech, I. A. Electromigration in thin aluminum films on titanium nitride. *J. Appl. Phys. 47*, 4 (1976), 1203–1208.

[15] Bly, D. N., and Rous, P. J. Theoretical study of the electromigration wind force for adatom migration at metal surfaces. *Phys. Rev. B 53* (May 1996), 13909–13920.

[16] Bowley, R., and Sánchez, M. *Introductory statistical mechanics*. Clarendon Press Oxford, 1999.

[17] Brenner, S. C., and Scott, R. *The mathematical theory of finite element methods*, vol. 15. Springer Science & Business Media, 2008.

[18] Cacho, F., Fiori, V., Chappaz, C., Tavernier, C., and Jaouen, H. Modeling of electromigration induced failure mechanism in semiconductor devices. *Proc. COMSOL Users Conference, Grenoble* (2007).

[19] Cahn, J. W., and Hilliard, J. E. Free energy of a nonuniform system. I. interfacial free energy. *J. Chem. Phys. 28*, 2 (1958), 258–267.

[20] Cassidy, C., Kraft, J., Carniello, S., Roger, F., Ceric, H., Singulani, A., Langer, E., and Schrank, F. Through silicon via reliability. *IEEE Trans. Device Mat. Rel. 12*, 2 (2012), 285–295.

[21] Ceric, H., de Orio, R. L., Cervenka, J., and Selberherr, S. A comprehensive TCAD approach for assessing electromigration reliability of modern interconnects. *IEEE Trans. Dev. Mat. Rel. 9*, 1 (2009), 9–19.

[22] Ceric, H., and Selberherr, S. Electromigration in submicron interconnect features of integrated circuits. *Mater. Sci. Eng. R-Rep. 71*, 5–6 (2011), 53–86.

[23] Chang, C., Wang, Y.-F., Kanamori, Y., Shih, J.-J., Kawai, Y., Lee, C.-K., Wu, K.-C., and Esashi, M. Etching submicrometer trenches by using the Bosch process and its application to the fabrication of antireflection structures. *J. Micromech. Microeng. 15*, 3 (2005), 580.

[24] Choa, S. H. Experimental studies of through-wafer copper interconnect in wafer level MEMS packaging. In *Key Engineering Materials* (2006), vol. 324, Trans. Tech. Publ., pp. 231–234.

[25] Clemens, B. M., Nix, W. D., and Gleixner, R. J. Void nucleation on a contaminated patch. *J. Mater. Res. 12* (1997), 2038–2042.

[26] Clement, J. J. Reliability analysis for encapsulated interconnect lines under DC and pulsed DC current using a continuum electromigration transport model. *J. Appl. Phys. 82*, 12 (1997), 5991–6000.

[27] Clement, J. J. Electromigration modeling for integrated circuit interconnect reliability analysis. *IEEE Trans. Dev. Mat. Rel. 1*, 1 (2001), 33–42.

[28] Clement, J. J., and Lloyd, J. R. Numerical investigations of the electromigration boundary value problem. *J. Appl. Phys. 71*, 4 (1992), 1729–1731.

[29] Clement, J. J., and Thompson, C. V. Modeling electromigration-induced stress evolution in confined metal lines. *J. Appl. Phys. 78*, 2 (1995), 900–904.

[30] COMSOL Inc. *COMSOL multiphysics 4.3a.* 2012. http://www.comsol.com/products/4.3a/.

[31] Craigie, C., Sheehan, T., Johnson, V., Burkett, S., Moll, A., and Knowlton, W. Polymer thickness effects on Bosch etch profiles. *J. Vac. Sci. Technol. B 20*, 6 (2002), 2229–2232.

[32] Crank, J. *The mathematics of diffusion.* Oxford university press, 1979.

[33] Datta, M., Osaka, T., and Schultze, J. W. *Microelectronic packaging.* CRC press, 2004.

[34] de Orio, R. L. *Electromigration modeling and simulation.* PhD thesis, Technische Universität Wien, 2010.

[35] de Orio, R. L., Ceric, H., and Selberherr, S. Physically based models of electromigration: From Black's equation to modern TCAD models. *Microelectron. Reliab. 50*, 6 (2010), 775–789.

[36] Debnath, L. *Nonlinear partial differential equations for scientists and engineers*, third ed. Birkhäuser Basel, 2012.

[37] Dekker, J. P., Lodder, A., and van Ek, J. Theory for the electromigration wind force in dilute alloys. *Phys. Rev. B 56* (1997), 12167–12177.

[38] Emmerich, H. *The diffuse interface approach in materials science: Thermodynamic concepts and applications of phase–field models*, vol. 73. Springer Science & Business Media, 2003.

[39] Emrick, R. M., and McArdle, P. B. Effect of pressure on quenched–In electrical resistance in gold and aluminum. *Phys. Rev. 188* (1969), 1156–1162.

[40] Ertl, O., and Selberherr, S. Three–dimensional level set based Bosch process simulations using ray tracing for flux calculation. *Microelectron. Eng. 87*, 1 (2010), 20–29.

[41] Finnis, M. W., and Sachdev, M. Vacancy formation volumes in simple metals. *J. Phys. F: Metal Physics 6*, 6 (1976), 965.

[42] Fisher, J. C. Calculation of diffusion penetration curves for surface and grain boundary diffusion. *J. Appl. Phys. 22*, 1 (1951), 74–77.

[43] Flinn, P. A. Mechanical stress in VLSI interconnections: Origins, effects, measurement, and modeling. *MRS Bulletin 20* (November 1995), 70–73.

[44] Frank, T., Chappaz, C., Leduc, P., Arnaud, L., Lorut, F., Moreau, S., Thuaire, A., El-Farhane, R., and Anghel, L. Resistance increase due to electromigration induced depletion under TSV. In *Proc. Intl. Reliability Physics Symp.* (2011), pp. 3F.4.1–3F.4.6.

[45] Freund, L. B., and Suresh, S. *Thin film materials: Stress, defect formation and surface evolution.* Cambridge University Press, 2004.

[46] Garrou, P., Bower, C., and Ramm, P. *Handbook of 3D integration: Volume 1–Technology and applications of 3D integrated circuits.* John Wiley & Sons, 2011.

[47] Garrou, P., Koyanagi, M., and Ramm, P. *Handbook of 3D integration: Volume 3–3D process technology.* John Wiley & Sons, 2014.

[48] Gaskell, D. R. *Introduction to the thermodynamics of materials.* CRC Press, 2008.

[49] Gleixner, R. J., Clemens, B. M., and Nix, W. D. Void nucleation in passivated interconnect lines: Effects of site geometries, interfaces, and interface flaws. *J. Mater. Res. 12* (1997), 2081–2090.

[50] Gleixner, R. J., and Nix, W. D. A physically based model of electromigration and stress–induced void formation in microelectronic interconnects. *J. Appl. Phys. 86*, 4 (1999), 1932–1944.

[51] Glicksman, M. *Diffusion in solids: Field theory, solid–state principles, and applications.* A Wiley–Interscience publication. Wiley, 1999.

[52] Grove, A. S., Leistiko, O., and Sah, C. T. Redistribution of acceptor and donor impurities during thermal oxidation of silicon. *J. Appl. Phys. 35*, 9 (1964), 2695–2701.

[53] Gurtin, M. E. Generalized Ginzburg–Landau and Cahn–Hilliard equations based on a microforce balance. *Phys. D 92*, 3–4 (1996), 178–192.

[54] Gurtin, M. E., and McFadden, G. B. *On the evolution of phase boundaries*, vol. 43. Springer Science & Business Media, 2012.

[55] Haasen, P. *Physikalische Metallkunde.* Springer Berlin Heidelberg, 1994.

[56] Hauschildt, M. *Statistical analysis of electromigration lifetimes and void evolution in Cu interconnects.* PhD thesis, The University of Texas at Austin, 2005.

[57] Herring, C. Diffusional viscosity of a polycrystalline solid. *J. Appl. Phys. 21*, 5 (1950), 437–445.

[58] Herring, C. Effect of change of scale on sintering phenomena. *J. Appl. Phys. 21*, 4 (1950), 301–303.

[59] Ho, P. S., and Kwok, T. Electromigration in metals. *Rep. Prog. Phys. 52*, 3 (1989), 301.

[60] Hollauer, C. *Modeling of thermal oxidation and stress effects.* PhD thesis, Technische Universität Wien, 2007.

[61] Holzer, S. *Optimization for enhanced thermal technology CAD purposes.* PhD thesis, Technische Universität Wien, 2007.

[62] Holzer, S., Hollauer, C., Ceric, H., Wagner, S., Langer, E., Grasser, K.-T., and Selberherr, S. Transient electro–thermal investigations of interconnect structures exposed to mechanical stress. In *Proc. Intl. Conf. on VLSI Circuits and Systems II* (2005), pp. 380–387.

[63] Hopwood, J. Ionized physical vapor deposition of integrated circuit interconnects. *Phys. Plasmas 5*, 5 (1998), 1624–1631.

[64] Huntington, H., and Grone, A. Current–induced marker motion in gold wires. *J. Phys. Chem. Solids 20*, 1–2 (1961), 76–87.

[65] Ikegawa, M., and Kobayashi, J. Deposition profile simulation using the direct simulation Monte Carlo method. *J. Electrochem. Soc. 136*, 10 (1989), 2982–2986.

[66] Jackson, J. D. *Classical electrodynamics*, third ed. Wiley, 1998.

[67] Johnson, C. *Numerical solution of partial differential equations by the finite element method.* Courier Corporation, 2012.

[68] Johnson, C., Nävert, U., and Pitkäranta, J. Finite element methods for linear hyperbolic problems. *Computer methods in applied mechanics and engineering 45*, 1 (1984), 285–312.

[69] Kaanta, C., Bombardier, S., Cote, W., Hill, W., Kerszykowski, G., Landis, H., Poindexter, D., Pollard, C., Ross, G., Ryan, J., Wolff, S., and Cronin, J. E. Dual damascene: A ULSI wiring technology. In *Proc. Intl. IEEE VLSI Multilevel Interconnection Conference* (1991), pp. 144–152.

[70] Kaltenbacher, M. *Numerical simulation of mechatronic sensors and actuators.* Springer-Verlag Berlin Heidelberg, 2007.

[71] Khan, N., and Hassoun, S. *Designing TSVs for 3D integrated circuits.* Springer Science & Business Media, 2012.

[72] Kim, D., and Lu, W. Creep flow, diffusion, and electromigration in small scale interconnects. *J. Mech. Phys. Solids 54*, 12 (2006), 2554–2568.

[73] Kim, J. Y. *Investigation on the mechanism of interface electromigration (EM) in copper (Cu) thin films.* PhD thesis, The University of Texas at Arlington, 2007.

[74] Kirchheim, R. Zur Lösung des 2. Fickschen Gesetzes unter nicht–isothermen Bedingungen in Gegenwart von äußeren Kräften. *Phys. Status Solidi B 91*, 1 (1979), 123–134.

[75] Kirchheim, R. Stress and electromigration in Al-lines of integrated circuits. *Acta. Metall. Mater. 40*, 2 (1992), 309–323.

[76] Kirchheim, R. Modelling electromigration and induced stresses in aluminum lines. In *Proc. M2 – Materials Reliability in Microelectronics III* (1993), vol. 309, pp. 101–110.

[77] Kirchheim, R., and Kaeber, U. Atomistic and computer modeling of metallization failure of integrated circuits by electromigration. *J. Appl. Phys. 70*, 1 (1991), 172–181.

[78] Kittel, C. *Introduction to solid state physics*, 6th ed. John Wiley & Sons, Inc., New York, 1986.

[79] Knechtel, R. Glass frit bonding: An universal technology for wafer level encapsulation and packaging. *Microsys. Technol. 12*, 1–2 (2005), 63–68.

[80] Knickerbocker, J., Andry, P., Dang, B., Horton, R., Patel, C., Polastre, R., Sakuma, K., Sprogis, E., Tsang, C., Webb, B., and Wright, S. 3D silicon integration. In *Proc. Electronic Components and Technology Conference* (2008), pp. 538–543.

[81] Kondo, K., Akolkar, R. N., Barkey, D. P., and Yokoi, M. *Copper Electrodeposition for Nanofabrication of Electronics Devices.* Springer New York, 2014.

[82] Korhonen, M. A., Børgesen, P., Tu, K. N., and Li, C. Stress evolution due to electromigration in confined metal lines. *J. Appl. Phys. 73*, 8 (1993), 3790–3799.

[83] Kraft, J., Schrank, F., Teva, J., Siegert, J., Koppitsch, G., Cassidy, C., Wachmann, E., Altmann, F., Brand, S., Schmidt, C., and Petzold, M. 3D sensor application with open through silicon via technology. *Proc. Elec. Comp. C* (2011), 560–566.

[84] Kubo, R. Statistical–mechanical theory of irreversible processes. I. General theory and simple applications to magnetic and conduction problems. *J. Phys. Soc. Jpn. 12*, 6 (1957), 570–586.

[85] Laermer, F., and Schilp, A. Verfahren zum anisotropen Ätzen von Silicium. A method for anisotropic etching of silicon, May 26 1994. DE Patent 4,241,045.

[86] Landauer, R. The Das–Peierls electromigration theorem. *J. Phys. C 8*, 19 (1975), L389.

[87] Landauer, R. Geometry and boundary conditions in the das–peierls electromigration theorem. *Phys. Rev. B 16* (1977), 4698–4702.

[88] Landauer, R. Spatial variation of currents and fields due to localized scatterers in metallic conduction (and comment). *J. Math. Phys. 37*, 10 (1996), 5259–5268.

[89] Landauer, R., and Woo, J. W. F. Driving force in electromigration. *Phys. Rev. B 10* (1974), 1266–1271.

[90] Lau, F., Mader, L., Mazure, C., Werner, C., and Orlowski, M. A model for phosphorus segregation at the silicon-silicon dioxide interface. *Appl. Phys. A 49*, 6 (1989), 671–675.

[91] Li, C.-Y., Børgesen, P., and Korhonen, M. A. Electromigration–induced failure in passivated aluminum-based metallizations – The dependence on temperature and current density. *Appl. Phys. Lett. 61*, 4 (1992), 411–413.

[92] Li, Y. *Microelectronic applications of chemical mechanical planarization.* John Wiley & Sons, 2007.

[93] Lloyd, J. R. Reliability modelling for electromigration failure. *Qual. Reliab. Eng. Int. 10*, 4 (1994), 303–308.

[94] Lloyd, J. R. Electromigration in thin film conductors. *Semicond. Sci. Tech. 12*, 10 (1997), 1177.

[95] Lloyd, J. R. Electromigration for designers: An introduction for the non–specialist. 1–16. http://eetimes.com/design/eda-design/4017969/Electromigration-for-Designers-An-Introdroction for the Non-Specialist.

[96] Lodder, A. The driving force in electromigration. *Physica A 158*, 3 (1989), 723–739.

[97] MacLaren, J. M., Crampin, S., Vvedensky, D. D., and Pendry, J. B. Layer Korringa–Kohn-Rostoker technique for surface and interface electronic properties. *Phys. Rev. B 40* (1989), 12164–12175.

[98] MacLaren, J. M., Zhang, X.-G., Butler, W. H., and Wang, X. Layer KKR approach to Bloch–wave transmission and reflection: Application to spin–dependent tunneling. *Phys. Rev. B 59* (1999), 5470–5478.

[99] Mahadevan, M., and Bradley, R. Phase field model of surface electromigration in single crystal metal thin films. *Physica D 126*, 3–4 (1999), 201–213.

[100] Mehrer, H. *Diffusion in Solids*, vol. 155 of *Springer Series in Solid–State Sciences*. Springer Berlin Heidelberg, 2007.

[101] Mizutani, U. *Introduction to the electron theory of metals*. Cambridge University Press, 2001.

[102] Nabarro, F. R. N. *Theory of crystal dislocations*. Clarendon Press, 1967.

[103] Naka, Y. *Introduction to VLSI process engineering*. Springer Science & Business Media, 1993.

[104] Nowick, A. S., and Burton, J. J. *Diffusion in solids: Recent developments*. Academic Press., New York, 1975.

[105] Ohno, K., Esfarjani, K., and Kawazoe, Y. *Computational materials science: from ab initio to Monte Carlo methods*, vol. 129. Springer Science & Business Media, 2012.

[106] Oono, Y., and Puri, S. Study of phase–separation dynamics by use of cell dynamical systems. I. Modeling. *Phys. Rev. A 38* (1988), 434–453.

[107] Pierce, D., and Brusius, P. Electromigration: A review. *Microelectron. Reliab. 37*, 7 (1997), 1053–1072. Reliability Physics of Advanced Electron Devices.

[108] Ramm, P., Lu, J. J.-Q., and Taklo, M. M. *Handbook of wafer bonding*. John Wiley & Sons, 2012.

[109] Reinhardt, K., and Kern, W. *Handbook of silicon wafer cleaning technology*. William Andrew, 2008.

[110] Rosenberg, R., and Ohring, M. Void formation and growth during electromigration in thin films. *J. Appl. Phys. 42*, 13 (1971), 5671–5679.

[111] Rous, P. Theory of surface electromigration on heterogeneous metal surfaces. *Appl. Surf. Sci. 175–176*, 0 (2001), 212–217.

[112] Rous, P. J. Electromigration wind force at stepped Al surfaces. *Phys. Rev. B 59* (1999), 7719–7723.

[113] Rous, P. J., and Bly, D. N. Wind force for adatom electromigration on heterogeneous surfaces. *Phys. Rev. B 62* (2000), 8478–8486.

[114] Ru, C. Thermomigration as a driving force for instability of electromigration induced mass transport in interconnect lines. *J. Mater. Sci. 35*, 22 (2000), 5575–5579.

[115] Sabelka, R. *Dreidimensionale Finite Elemente Simulation von Verdrahtungsstrukturen auf Integrierten Schaltungen*. PhD thesis, Technische Universität Wien, 2001.

[116] Sarychev, M. E., Zhitnikov, Y. V., Borucki, L., Liu, C.-L., and Makhviladze, T. M. General model for mechanical stress evolution during electromigration. *J. Appl. Phys. 86*, 6 (1999), 3068–3075.

[117] Schaich, W. L. Theory of the driving force for electromigration. *Phys. Rev. B 13* (1976), 3350–3359.

[118] Schoenmaker, W., and Petrescu, V. Modeling electromigration as a fluid–gas system. *Microelectron. Reliab. 39*, 11 (1999), 1667–1676.

[119] Schwartz, G. C., and Srikrishnan, K. V. *Handbook of semiconductor interconnection technology*. CRC Press, 2006.

[120] Seith, W., and Wever, H. Die Aktivität bei der Diffusion in metallischen Dreistoffsystemen. *Zeitschrift für Elektrochemie und angewandte physikalische Chemie 55*, 5 (1951), 380–384.

[121] Selberherr, S. *Analysis and simulation of semiconductor devices*. Springer Wien, 1984.

[122] Selvanayagam, C., Lau, J., Zhang, X., Seah, S., Vaidyanathan, K., and Chai, T. Nonlinear thermal stress/strain analyses of copper filled TSV (through silicon via) and their flip–chip microbumps. *IEEE Trans. Adv. Packaging 32*, 4 (2009), 720–728.

[123] Seshan, K. *Handbook of thin film deposition*. William Andrew, 2012.

[124] Sham, L. J. Microscopic theory of the driving force in electromigration. *Phys. Rev. B 12* (1975), 3142–3149.

[125] Shatzkes, M., and Huang, Y. Characteristic length and time in electromigration. *J. Appl. Phys. 74*, 11 (1993), 6609–6614.

[126] Shatzkes, M., and Lloyd, J. R. A model for conductor failure considering diffusion concurrently with electromigration resulting in a current exponent of 2. *J. Appl. Phys. 59*, 11 (1986), 3890–3893.

[127] Skriver, H. L. *The LMTO method: muffin-tin orbitals and electronic structure*, vol. 41. Springer Science & Business Media, 2012.

[128] Sorbello, R. Landauer fields in electron transport and electromigration. *Superlattices Microstruct. 23*, 3–4 (1998), 711–718.

[129] Sorbello, R. S. Residual–resistivity dipole in electron transport and electromigration. *Phys. Rev. B 23* (1981), 5119–5127.

[130] Sorbello, R. S. Theory of the direct force in electromigration. *Phys. Rev. B 31* (1985), 798–804.

[131] Sorbello, R. S. Microscopic driving forces for electromigration. *Proc. Mater. Research Soc. Symp. 427* (1996), 73–81.

[132] Sorbello, R. S., Lodder, A., and Hoving, S. J. Finite–cluster description of electromigration. *Phys. Rev. B 25* (1982), 6178–6187.

[133] Sørensen, M. R., Mishin, Y., and Voter, A. F. Diffusion mechanisms in Cu grain boundaries. *Phys. Rev. B 62* (2000), 3658–3673.

[134] Strong, A. W., Wu, E. Y., Vollertsen, R.-P., Sune, J., La Rosa, G., Sullivan, T. D., and Rauch III, S. E. *Reliability wearout mechanisms in advanced CMOS technologies*, vol. 12. John Wiley & Sons, 2009.

[135] Suhir, E. Accelerated life testing (ALT) in microelectronics and photonics: Its role, attributes, challenges, pitfalls, and interaction with qualification tests. *J. Electron. Packaging 124* (2002), 281–291.

[136] Sukharev, V., Choudhury, R., and Park, C. Physically–based simulation of the early and long-term failures in the copper dual damascene interconnect. In *IRWS* (2003), pp. 80–85.

[137] Sukharev, V., Kteyan, A., and Zschech, E. Physics–based models for EM and SM simulation in three-dimensional IC structures. *IEEE Trans. Device Mater. Rel. 12*, 2 (2012), 272–284.

[138] Sukharev, V., and Zschech, E. A model for electromigration-induced degradation mechanisms in dual-inlaid copper interconnects: Effect of interface bonding strength. *J. Appl. Phys. 96* (2004), 6337–6343.

[139] Tan, C. M., and Roy, A. Electromigration in ULSI interconnects. *Mater. Sci. Eng. R–Rep. 58*, 1–2 (2007), 1–75.

[140] Tan, C. S., Chen, K.-N., and Koester, S. J. *3D integration for VLSI systems*. CRC Press, 2011.

[141] Teschl, G. *Mathematical methods in quantum mechanics*, vol. 157. American Mathematical Soc., 2014.

[142] Thrasher, S., Capasso, C., Zhao, L., Hernandez, R., Mulski, P., Rose, S., Nguyen, T., and Kawasaki, H. Blech effect in single-inlaid Cu interconnects. In *Proc. IEEE Intl. Interconnect Technology Conference* (2001), pp. 177–179.

[143] Tu, K. N. Recent advances on electromigration in very–large–scale–integration of interconnects. *J. Appl. Phys. 94*, 9 (2003), 5451–5473.

[144] van Ek, J., Dekker, J. P., and Lodder, A. Electromigration of substitutional impurities in metals: Theory and application in Al and Cu. *Phys. Rev. B 52* (1995), 8794–8800.

[145] van Ek, J., and Lodder, A. Electromigration in transition metals. II. Light interstitials in Cu, Ag, Ni, Pd, Al, V, Nb and Ta. *J. Phys. Condens. Matter 3*, 38 (1991), 7331.

[146] Wetzig, K., and Schneider, C. M. *Metal based thin films for electronics.* Wiley Online Library, 2003.

[147] Wieting, T. J., and Schlüter, M. *Electrons and phonons in layered crystal structures*, vol. 3. Springer Science & Business Media, 2012.

[148] Wittmer, M. Barrier layers: Principles and applications in microelectronics. *J. Vac. Sci. Technol. A 2*, 2 (1984), 273–280.

[149] Wolf, S. Silicon processing for the VLSI era, volume 4 – deep-submicron process technology, chapter 15. Sunset Beach, 2002.

[150] Zeidler, E. *Springer-Taschenbuch der Mathematik.* Springer Spektrum, 2013.

Own Publications

[1] Ceric, H., Lacerda de Orio, R., Zisser, W. H., and Selberherr, S. Microstructural Impact on Electromigration: A TCAD Study. *Facta universitatis - series: Electronics and Energetics 27*, 1 (2014), 1–11.

[2] Ceric, H., Lacerda de Orio, R., Schanovsky, F., Zisser, W. H., and Selberherr, S. Multilevel Simulation for the Investigation of Fast Diffusivity Paths. In *Proceedings of the 16th International Conference on Simulation of Semiconductor Processes and Devices (SISPAD)* (2011), pp. 135–138.

[3] Ceric, H., Lacerda de Orio, R., Zisser, W. H., Schnitzer, V., and Selberherr, S. Modeling of Microstructural Effects on Electromigration Failure. In *Abstracts of the 12th International Workshop on Stress-Induced Phenomena in Microelectronics* (2012), pp. 50–51.

[4] Ceric, H., Lacerda de Orio, R., Zisser, W. H., and Selberherr, S. Ab Initio Method for Electromigration Analysis. In *Proceedings of the 19th IEEE International Symposium on the Physical & Failure Analysis of Integrated Circuits* (2012), pp. 1–4.

[5] Ceric, H., Zisser, W. H., Rovitto, M., and Selberherr, S. Electromigration in Solder Bumps: A Mean-Time-to-Failure TCAD Study. In *Proceedings of the 19th International Conference on Simulation of Semiconductor Processes and Devices (SISPAD)* (2014), pp. 221–224.

[6] Ceric, H., Zisser, W. H., and Selberherr, S. Quantum Mechanical Calculations of Electromigration Characteristics. In *Abstracts of the 13th International Workshop on Stress-Induced Phenomena in Microelectronics* (2014), p. 16.

[7] Marti, G., Zisser, W. H., Arnaud, L., and Wouters, Y. Electromigration: Multiphysics Model and Experimental Calibration. In *Proceedings of the 2016 IEEE International Reliability Physics Symposium (IRPS)* (2016), in print.

[8] Papaleo, S., Zisser, W. H., and Ceric, H. Factors that Influence Delamination at the Bottom of Open TSVs. In *Proceedings of the 20th International Con-*

ference on Simulation of Semiconductor Processes and Devices (SISPAD) (2015), pp. 421–424.

[9] Papaleo, S., Zisser, W. H., and Ceric, H. Effects of the Initial Stress at the Bottom of Open TSVs. In *Proceedings of the IEEE 22nd International Symposium on the Physical and Failure Analysis of Integrated Circuits (IPFA)* (2015), p. P7–4.

[10] Papaleo, S., Zisser, W. H., Singulani, A. P., Ceric, H., and Selberherr, S. Stress Analysis in Open TSVs after Nanoindentation. In *Abstracts of the GDRI CNRS Mecano General Meeting on the Mechanics of Nano-objects* (2014), pp. 39–40.

[11] Papaleo, S., Zisser, W. H., Singulani, A. P., Ceric, H., and Selberherr, S. Stress Evolution During the Nanoindentation in Open TSVs. In *Abstracts of the 13th International Workshop on Stress-Induced Phenomena in Microelectronics* (2014), p. 44.

[12] Rovitto, M., Zisser, W. H., and Ceric, H. Analysis of Electromigration Void Nucleation Failure Time in Open Copper TSVs. In *Proceedings of the IEEE 22nd International Symposium on the Physical and Failure Analysis of Integrated Circuits (IPFA)* (2015), p. P7–1.

[13] Rovitto, M., Zisser, W. H., Ceric, H., and Grasser, K.-T. Electromigration Modelling of Void Nucleation in Open Cu-TSVs. In *Proceedings of the IEEE 16th International Conference on Thermal, Mechanical & Multi-Physics Simulation and Experiments in Microelectronics and Microsystems (EuroSimE)* (2015), pp. 1–5.

[14] Zisser, W. H., Ceric, H., Lacerda de Orio, R., and Selberherr, S. Electromigration Analyses of Open TSVs. In *Proceedings of the 18th International Conference on Simulation of Semiconductor Processes and Devices (SISPAD)* (2013), pp. 244–247.

[15] Zisser, W. H., Ceric, H., Lacerda de Orio, R., and Selberherr, S. Electromigration Induced Stress in Open TSVs. In *2013 IEEE International Integrated Reliability Workshop Final Report* (2013), pp. 142–145.

[16] Zisser, W. H., Ceric, H., and Selberherr, S. Stress Development and Void Evolution in Open TSVs. In *Abstracts of the GDRI CNRS Mecano General Meeting on the Mechanics of Nano-objects* (2014), pp. 38–39.

[17] Zisser, W. H., Ceric, H., and Selberherr, S. Void Evolution in Open TSVs. In *Abstracts of the 13th International Workshop on Stress-Induced Phenomena in Microelectronics* (2014), p. 58.

[18] Zisser, W. H., Ceric, H., Weinbub, J., and Selberherr, S. Electromigration Induced Resistance Increase in Open TSVs. In *Proceedings of the 19th*

International Conference on Simulation of Semiconductor Processes and Devices (SISPAD) (2014), pp. 249–252.

[19] Zisser, W. H., Ceric, H., Weinbub, J., and Selberherr, S. Electromigration Reliability of Open TSV Structures. *Microelectronics Reliability 54*, 9-10 (2014), 2133–2137.

[20] Zisser, W. H., Ceric, H., Weinbub, J., and Selberherr, S. Electromigration Reliability of Open TSV Structures. In *Abstracts of the 25th European Symposium on Reliability of Electron Devices, Failure Physics and Analysis (ESREF)* (2014), p. 48.

[21] Zisser, W. H., Ceric, H., Weinbub, J., and Selberherr, S. Electromigration Reliability of Open TSV Structures. In *Proceedings of the 21st International Symposium on the Physical and Failure Analysis of Integrated Circuits* (2014), pp. 317–320.

	Author	Co-Author	Total
Journals	1	1	2
Conferences	7	12	19
Total	8	13	21

Publication Statistics.

Curriculum Vitae

1995-1996

International School of Islamabad, Pakistan.

June 2001

High school graduation (*Matura*) at the TGM Wien, specializing in Electrical Engineering (with honors).

October 2011

Received degree of *Diplom-Ingenieur* (equiv. M.Sc.) in Industrial Engineering, specializing in Finanzwirtschaft & Risikomanagement from the Fakultät für Maschinenwesen und Betriebswissenschaften, Technische Universität Wien (with honors).

November 2011

Entered doctoral program at the Institute for Microelectronics, Technische Universität Wien, under the supervision of Prof. Siegfried SELBERHERR.